

Doctorate Dissertation (Censored)

博士論文 (要約)

Development of the resonant magneto-optical Kerr effect and
the study of transient magnetization dynamics in thin films
(共鳴磁気光学効果の手法開発と薄膜の磁気ダイナミクス研究)

A Dissertation Submitted for Degree of Doctor of Philosophy

August 2017

平成 29 年 8 月博士(理学)申請

Department of Physics, Graduate School of Science,

The University of Tokyo

東京大学大学院理学系研究科物理学専攻

Shingo Yamamoto

山本 真吾

Supervisor: Professor Iwao Matsuda

Abstract

Magnetization dynamics on a femtosecond timescale, so-called femtomagnetism, has been attracting attention for more than two decades because of its potential for use in the development of novel spintronic devices as well as its fundamental physics. Although the mechanism of magnetization dynamics process on the femtosecond timescale, such as demagnetization and magnetization reversal, remains controversial from the microscopic perspective, the application demands in the field of spintronics expand the realm of the target magnetic systems from pure ferromagnetic materials into multi-component magnetic systems. Furthermore, the high density integration of the data devices with ever-faster processing speed needs the deeper understanding of dynamical properties of ultrathin magnetic films with out-of-plane magnetization. At the same time, in order to reduce the energy consumption and to avoid the notorious heat issues, electric-field driven magnetization control is preferred, which requires to trace spins under the real operating environment with the electric field as well as the magnetic field.

In this thesis, we developed a novel measurement technique, the time-resolved magneto-optical Kerr effect (MOKE) in the extreme ultraviolet / soft X-ray range using a free electron laser (FEL) in order to incorporate the current demands from fundamentals and application in the field of magnetism. We extended the conventional MOKE measurements involved with the optical transition between delocalized states into the resonant MOKE (RMOKE) using the photon energy tuned to the specific absorption edge of core levels. The advantages of the time-resolved RMOKE using FEL revealed in this thesis are the following: (1) element selectivity, (2) time-resolution of sub-picosecond timescale, (3) detection of out-of-plane magnetization, (4) sensitivity to subnanometer-scale system, (5) measurement under the external field (the operando condition), (6) giant magneto-optical response compared with the conventional MOKE. On top of the features described above, the RMOKE scheme has a potential to extend into the nonlinear regime. Because nonlinear effects itself in the EUV / soft X-ray range has not been observed in the preceding studies due to the lack of the intense laser in the energy range, in this thesis we aimed at observation of the nonlinear optical effect, second harmonic generation (SHG). We measured the SHG in the EUV range for the first time using FEL from the non-centrosymmetric gallium ferrite by facilitating the resonant enhancement under a reflection geometry, which opens the way to extend the RMOKE into the nonlinear regime.

Acknowledgements

It would not have been possible for me to survive through without help from so many people for conducting PhD research during past five years. I would like to take this opportunity to acknowledge all the people who have encouraged, helped, and supported me over five years.

First of all, I would like to thank my supervisor, Prof. Iwao Matsuda. I have been fortunate enough to receive tremendous guidance and knowledge from him during these past years. I met with him when I was undergraduate student at a seminar in a small group that had been held during half a year. Thanks to him, I knew the fascinating world of soft X-ray sciences ranging from third generation synchrotron radiation (SR) to state-of-the-art free electron laser (FEL). He gave me the opportunity to be in charge of developing new magneto-optical measurement systems combining with a variety of cutting-edge soft X-ray light sources such as SR, FEL, and high harmonic generation (HHG) laser. He always puts an emphasis on the importance of discussion in conducting research and enjoy its process. I have learned a great deal from his commitment and gratitude toward science and its activity about how one comes up with a research topic from the context of big picture including applications as well as fundamentals and grasps the essence of the problem by focusing on its physical intuition. His intuitional suggestions not only have helped me solve so many problems in my experiments, but also have been good examples to tackle a problem. I am also grateful for his patience and help in improving my writing and presentation skills.

I would like to thank Dr. Susumu Yamamoto, for giving me objective advise in writing papers and designing experiments at SACLA. He showed me the way to conduct research with carefully and critical thinking.

I express my gratitude to all the students of Matsuda Laboratory. I would like to thank Dr. Manami Ogawa for teaching me the system of time-of-flight ARPES system at SPring-8 when I entered this group, Dr. Ryu Yukawa for teaching me at any time, no matter how busy he is and discussing many topics ranging from science to music and things in daily life, Dr. Yuya Kubota for conducting experiments and overcome many difficulties together and having drinking sometimes with friends who studied together when we were undergraduate student, Ms. Ro-ya Liu for showing me many delicious food through facebook and teaching me many nice Chinese foods, Mr. Takashi Someya for conducting development of measurement system using a HHG laser together, Mr.

Kazuma Akikubo for helping me measure X-ray photoelectron spectroscopy at SPring-8, Mr. Suguru Ito for planning many group party and discussing various research topics, Ms. Kaori Takeuchi for teaching me the system of AK2B chamber and Mr. Kazushi Fujikawa for teaching me the fun of shogi.

I also would like to thank the group of Prof. Satoshi Iwata in Nagoya University. Prof. Iwata allowed me to conduct collaborating research during my PhD research. He gave me the opportunity to synthesize thin magnetic films and evaluate various magnetic properties using experimental setups owned by his group. Dr. Takeshi Kato gave me valuable advice when I was facing with scientific issues and also takes care of me when I was staying Nagoya University for experiments. Dr. Daiki Oshima gave me instruction for operating experiments. Two students of Prof. Iwata group, Mr. Tomohiro Higashide and Mr. Kengo Fukuta, helped me when I faced with technical problem in conducting experiments at Nagoya University.

I would like to thank the group of Prof. Hiroki Wadati in ISSP. We conducted experiments at SACLA together and also they allowed me to join experiments at BESSY-II and FLASH in Germany. I would like to thank Prof. Wadati for joining my experiment at FERMI in Italy. I also would like to thank Dr. Yasuyuki Hirata, Dr. Ko Takubo Mr. Tomoyuki Tsuyama and Mr. Kohei Yamamoto.

I would like to thank Mr. Rei Hobara for teaching me LabView programming and data acquisition techniques.

I would like to express my gratitude to Mr. Masami Fujisawa. He taught me technical stuffs necessary for developing experimental chambers that were used for a HHG beamline. I would like to thank Dr. Koichiro Yaji, Ms. Ayumi Harasawa and Ms. Akiko Fukushima for their kind support for resonant magneto-optical Kerr effect experiments at photon factory and for fabrication of magnetic films at E-building.

I would like to thank Prof. Jiro Itatani, Dr. Nobuhisa Ishii and Mr. Teruto Kanai for collaboration research using a HHG laser and giving me technological advices. I also would like to thank Prof. Shik Shin, Dr. Yukiaki Ishida, Prof. Kozo Okazaki, Dr. Rikiya Yoshida, and Dr. Takashi Yamamoto because in the experiments using HHG laser, we borrowed a femtosecond Ti:sapphire laser from Prof. Shin's group and they have given us many useful techniques for generation of high harmonics and for adjustment of optical alignment.

I would like to thank Prof. Eiji Shigemasa for giving me an opportunity to use BL5B in UVSOR, Dr. Masami Hasumoto for supporting experiments at BL5B in UVSOR,

and Dr. Yasumasa Takagi for supporting X-ray magnetic circular dichroism (XMCD) experiments at BL4B in UVSOR.

I would like to thank Dr. Tetsuya Nakamura for supporting when I conducted XMCD experiments at BL25SU@SPring-8 and giving me much useful advice in terms of magnetism. I also would like to thank Dr. Hiroaki Kimura and Dr. Toko Hirono. I have conducted polarization measurement at BL07LSU@SPring-8 using a sophisticated ellipsometry named Elli together. I could know much technological information that could be used in my experimental setups using HHG laser when we aligned optical components and chambers in an efficient way. I also would like to thank Dr. Munetaka Taguchi for simulating resonant MOKE spectra using resonant scattering theory. I would also like to thank Dr. Mitsuru Nagasono, Dr. Makina Yabashi, Dr. Tadashi Togashi, Dr. Shigeki Owada, Dr. Kensuke Tono for their experimental support and technical advice given when we conducted experiments using SACLA.

I would also like to thank Prof. Kenta Amemiya. He had explained his apparatus for XMCD measurements. He also gave me useful information in analyzing XMCD spectrum. I also would like to thank Prof. Hiroshi Kumigashira and Prof. Koji Horiba. They gives us to measure XPS measurements of GaFeO₃ with the help of Dr. Ryu Yukawa.

I would like to thank scientists in DiProI beamline in FERMI@ELETTRA in Italy, Dr. Flavio Capotondi, Dr Emanuele Pedersoli, and Dr. Maya Kiskinova. I also would like to thank Dr. Jun Fujii and scientists in APE beamline and Dr. Paolo Moras for joint research. I also would like to thank scientists in TIMEX beamline, Dr. Claudio Masciovecchio, Dr. Filippo Bencivenga and Dr. Emiliano Principi, for allowing me to join cutting-edge experiments when I have been staying ELETTRA and FERMI for three months.

I am also grateful to the members, Prof. Yoshihisa Harada, Dr. Jun Miyawaki, Dr. Hideharu Niwa, Dr. Hisao Kiuchi, Dr. Yitao Cui, Mr. Junki Nakajima, Mr. Kosuke Yamazoe, Mr Takanobu Inoue, Mr. Hao Wang, Mr. Naoki Itamoto, Prof. Koji Horiba, Dr. Naoka Nagamura, Ms. Mihoko Araki, and Ms. Yuka Kosegawa. They made my stay in SPring-8 comfortable and friendly atmosphere.

I would like to thank Prof. Fumio Komori, Dr. Toshio Miyamachi, Dr. Masamichi Yamada, Mr. Takushi Iimori, Dr. Sunghun Kim, Mr. Yukio Takahashi, Mr. Shuhei Nakajima and Mr. Takuma Hattori for kind help and valuable advices at our joint group seminar.

I am grateful to Prof. Masakiyo Tsunoda in Tohoku University for joint research and giving me samples of Ni thin films for resonant MOKE measurements.

I am grateful to the secretary of SOR office, Ms. Yumiko Aihara, Ms. Misa Harada, Ms. Yoshie Kaneko, Ms. Akiko Someya, Ms. Yukimi Yamamoto, Ms. Motoko Yoshizawa, Ms. Yumiko Tsutsumi, Ms. Akiko Hayashi and Ms. Kuniko Ikeda. Their great assistance helped me perform daily research activity smoothly.

And finally I would like to thank my family for their kind support until today.

This work was partially supported by the Ministry of Education, Culture, Sports, Science and Technology of Japan (X-ray Free Electron Laser Priority Strategy Program). I was supported by the Grant-in-Aid for JSPS Fellows and the Program for Leading Graduate Schools (MERIT).

Contents

Abstract	v
Acknowledgements	vi
Abbreviations	xv
1 Introduction	1
1.1 Background	1
1.2 Purpose of the present study	4
1.3 Structure of this thesis	5
2 Historical overview of magneto-optical spectroscopy	7
2.1 Laser-induced magnetization dynamics	7
2.2 Conventional methods	9
2.3 Necessity of resonant magneto-optical techniques	14
2.4 Magneto-optical Kerr effect	18
2.4.1 Phenomenological description	21
2.4.2 Physical picture	22
2.4.3 Preceding studies of visible MOKE	26
2.4.4 Visible and soft X-ray regime	30
2.4.5 Extension into a nonlinear regime	32
2.5 X-ray magnetic circular dichroism	33
2.5.1 Magneto-optical sum rules	33
3 Femtosecond EUV/soft X-ray light source	35
3.1 Free electron laser	35
3.2 High harmonic generation laser	40
3.3 Synchrotron radiation with a laser-slicing technique	43
3.4 Comparison of femtosecond EUV / soft X-ray pulses	43
4 Static <i>M</i>-edge polar resonant MOKE	45
4.1 Introduction	45
4.1.1 Preceding studies of resonant MOKE	46

4.2	Development of a resonant MOKE measurement system	49
4.2.1	Measurement regime in soft X-ray region	49
4.3	Experiment	57
4.3.1	Sample Structure	57
4.4	Results and Discussions	58
4.4.1	Spin and Orbital moment	58
4.4.2	Ni <i>M</i> -edge polar resonant MOKE	58
4.5	Conclusion	61
5	Extension of resonant MOKE technique to sub-picosecond time resolution	63
5.1	Introduction	63
5.1.1	Pump-Probe Scheme	63
5.1.2	Magnetic and optical response in TR-MOKE measurements . . .	65
5.1.3	Shot-by-shot measurement system	66
5.2	First time-resolved resonant MOKE measurement with a FEL	67
5.2.1	Introduction	67
5.2.2	Experiment	71
5.2.3	Results and discussion	71
5.2.4	Conclusion	79
5.3	Sensitivity for magnetization dynamics of subnanometer ultrathin magnetic film	81
5.4	Development for resonant MOKE measurement system with a HHG laser	82
5.4.1	Introduction	82
5.4.2	Developments	83
5.4.3	Experiment	90
5.4.4	Conclusion and future prospects	93
5.5	Conclusion	95
6	Resonant enhancement of second harmonic generation in the EUV region	97
6.1	Introduction	97
6.2	Experiment	100
6.3	Results	101
6.3.1	Second harmonic generation measurement using FEL	101
6.3.2	X-ray photoelectron spectroscopy	103
6.4	Discussion	104
6.5	Conclusion	105
7	Conclusions	109
7.1	Summary	109
7.2	Future prospect	111
A	Magnetic moment of 3<i>d</i> transition metals	113

B	Experimental methods	115
B.1	RHEED	115
B.2	Alternating gradient magnetometer	118
B.3	Torque Magnetometer	119
C	Configuration-interaction cluster-model calculation	121
D	Time-resolved resonant MOKE measurement system using a HHG laser	125
	Bibliography	131

Abbreviations

AFMR	AntiFerroMagnetic Resonance
AGM	Alternating Gradient Magnetometer
APD	Avalanche PhotoDiode
bcc	body-centered cubic
BLS	Brillouin Light Scattering
CPA	Chirped Pulse Amplification
EUV	Extreme Ultraviolet
fcc	face-centered cubic
FEL	Free Electron Laser
FERMI	Free Election laser Radiation for Multidisciplinary Investigations
FMR	FerroMagnetic Resonance
FTH	Fourier Transform Holography
GGA	Generalized Gradient Approximation
hcp	hexagonal closed-packed
HHG	High Harmonic Generation
IFE	Inverse Faraday Effect
IR	InfraRed
IS	Inversion Symmetry
LASER	Light Amplification by Stimulated Emission of Radiation
LCLS	Linac Coherent Light Source
LSDA	Local Spin Density Approximation
L-MOKE	Longitudinal Magneto-Optical Kerr Effect
L-RMOKE	Longitudinal ResonantMagneto-Optical Kerr Effect
MAE	Magneto-crystalline Anisotropy Energy

MBE	M olecular B eam E pitaxy
MLM	M ulti L ayer M irror
MO	M agneto- O ptics
MOKE	M agneto- O ptical K err E ffect
MSHG	M agnetization-induced S econd H armonic G eneration
OPA	O ptical P arametric A mplifier
P-MOKE	P olar M agneto- O ptical K err E ffect
P-RMOKE	P olar R esonant M agneto- O ptical K err E ffect
RAE	R otating- A nalyzer E llipsometry
RE	R are E arth
RHEED	R eflection H igh- E nergy E lectron D iffraction
RMOKE	R esonant M agneto- O ptical K err E ffect
RIXS	R esonant I nelastic X -ray S cattering
RSXD	R esonant S oft X -ray D iffraction
SASE	S elf- A mplified S pontaneous E mission
SAXS	S mall A ngle X -ray S cattering
SCSS	S Pring-8 C ompact S elf- A mplified S pontaneous E mission S ource
SHG	S econd H armonic G eneration
SP-PES	S pin P olarized P hoto E lectron S pectroscopy
SR	S ynchrotron R adiation
TFY	T otal F luorescence Y ield
THz-TDS	T era H ertz- T ime D omain S pectroscopy
TM	T ransition M etal
TMP	T urbo M olecular P ump
TR	T ime R esolved
T-MOKE	T ransverse M agneto- O ptical K err E ffect
T-RMOKE	T ransverse R esonant M agneto- O ptical K err E ffect
UV	U ltra V iolet
XAS	X -ray A bsorption S pectroscopy
XMCD	X -ray M agnetic C ircular D ichroism
XMLD	X -ray M agnetic L inear D ichroism
XRD	X - R ay D iffraction

Chapter 1

Introduction

1.1 Background

While magnetism has been one of the central topics in the condensed matter physics for about two hundred years, it has been also deeply ingrained in our real life since the age of navigation more than a millennium before, when the nature of magnetism was employed in a compass needle. The variation of magnetization probing techniques has expanded since the discovery of Faraday effect by Michael Faraday in 1845 and of Kerr effect by John Kerr in 1876. This discovery reminded the relation between magnetism and incident particles, photons. Currently, the main probes for the magnetization are photons, electrons and neutrons. The interaction between the magnetism and incoming particles defines the information that a specific probing technique can extract from measurements. Various magnetization probing techniques have revealed the magnetism of a wide variety of target systems on a different length and time scale. Furthermore, magnetic excitations as well as ground states of magnetic materials have also investigated through the interaction of magnetization and particles.

Here we briefly review the current magnetism research. Examining the challenges facing this field, we will discuss the features desired in measurement methods.

Challenge in magnetism research

In this section, we start by reviewing the current topics and challenges in magnetism. We will also discuss the features needed for measurement techniques in the frontier of magnetism research. Currently, magnetism research encompasses three major topics:

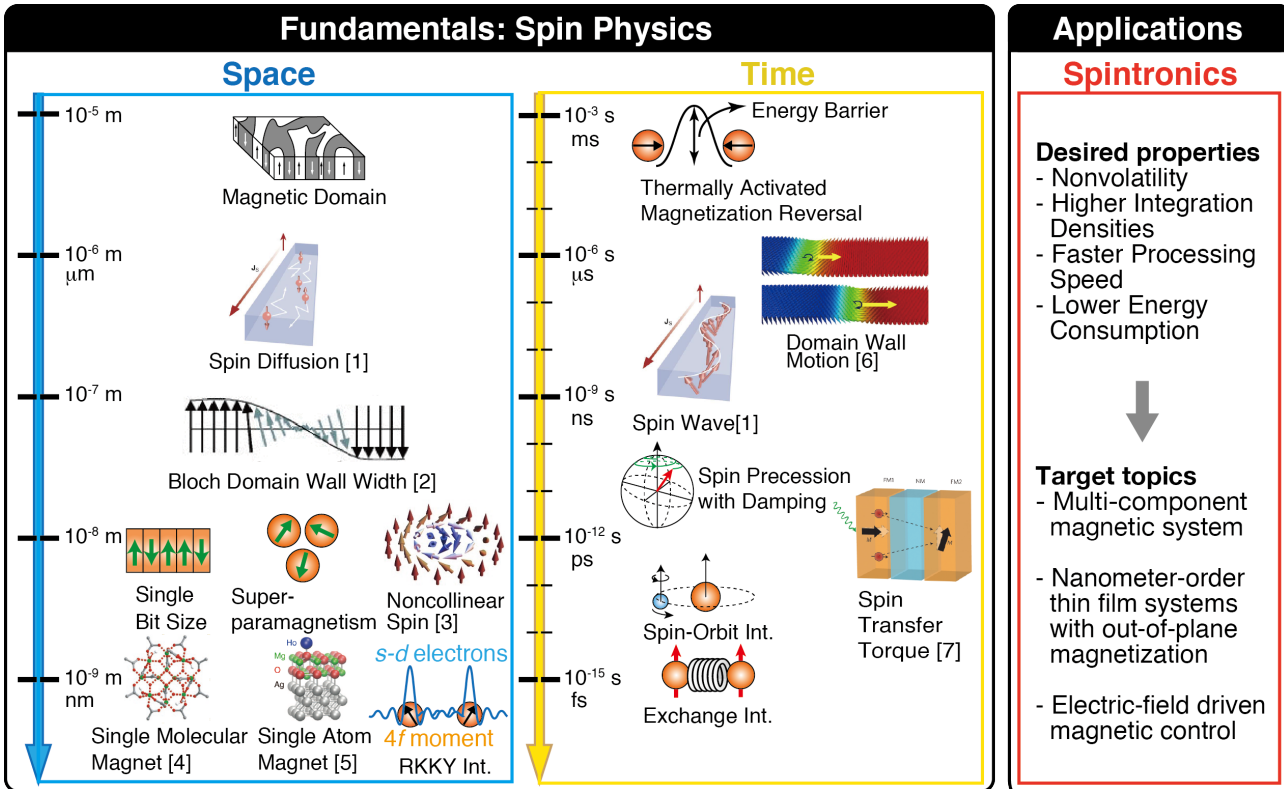


FIGURE 1.1: There are three main research directions in magnetism: first, the dimensions or length of magnetism phenomena ranging from tens of micrometers down to the sub-nanometer scale; second, the dynamical features ranging from milliseconds down to femtosecond (10^{-15} s); third, applications of fundamental spin physics, called spintronics. Some of these drawings are taken from [1–7].

1) Exploring the length scales of the interactions of magnetic phenomena, 2) revealing the temporal features of magnetization, and 3) using fundamental spin physics in applications, a field called spintronics. These topics are shown in Fig. 1.1.

Regarding length scale, magnetism is related to various kinds interaction at very different length scales. For example, magnetic domains form on the scale of 10 – 100 μm , spin retains direction with a length of a few μm and the width of Bloch domain wall is on the order of 10 nm. The minimum size of a magnetic particle that shows superparamagnetism and a noncollinear spin structure such as a vortex core is on the order of a few nanometers, though recently single-molecular and single-atom magnets, whose size is on the order of nanometers, have been observed. Ruderman–Kittel–Kasuya–Yoshida interactions also operate on the nanometer scale. Scientists are also interested in how dimensionality, symmetry and boundary conditions affect the

spin structure and its transport nature. The target systems have become smaller and have now reached the subnanometer scale, making it desirable to develop measurement methods with **sensitivity to subnanometer-scale system**.

Regarding time scale, various phenomena occur on the millisecond scale down to the femtosecond scale. On the millisecond scale, thermally activated magnetization reversal occurs by overcoming the energy barrier; domain wall motion occurs on the microsecond scale; and collective magnetic excitation, which produces spin waves, propagates on the nanosecond scale. Spin precession and magnetization reversal caused by spin transfer torque are on the order of a hundred picoseconds. Recently, the sub-picosecond timescale has been intensively investigated because such a fast timescale involves exchange interactions and spin-orbit interactions, which are the fundamental interactions in forming long-range magnetic order. The desire to investigate faster timescales make it important to develop measurement techniques with **sub-picosecond resolution**.

Regarding applications, the following features are desired in novel magnetic devices: 1) nonvolatility, 2) faster processing speed, 3) lower energy consumption (such as by reversing magnetization without current), and 4) higher integration density, which favors materials with perpendicular magnetization. Scientists and engineers have tried to develop these devices by facilitating the spin degree of freedom while using conventional electronic technologies. Developing such quantum information processing devices requires systems ranging from simple ferromagnetic metals to multi-component magnetic compounds. In spintronics, **element-specific** techniques that can detect **out-of-plane magnetization under an external field** are indispensable for disentangling the complicated interplay of magnetic elements in multicomponent systems.

To summarize, the frontier of magnetism research requires measurement techniques with the following features:

- Measurement under an external field
- Element selectivity
- The ability to trace out-of-plane magnetization dynamics
- The ability to trace with sub-picoseconds resolution
- Sensitivity to subnanometer-scale system

1.2 Purpose of the present study

This thesis aims to newly develop a magneto-optical technique with the characteristics listed at the end of the previous section. This objective can be broken down into the following targets.

- (i) We extend the conventional magneto-optical Kerr effect (MOKE) measurement from the visible region into the extreme ultraviolet (EUV) / soft X-ray region, using a technique called resonant MOKE (RMOKE). We establish a static RMOKE technique that can measure out-of-plane magnetization. The definition of RMOKE is given in the next chapter. Although there are some earlier works on RMOKE, all of them used an in-plane detection technique. We first conduct RMOKE in a polar geometry to detect out-of-plane magnetization. This system is important for its element selectivity and its ability to detect out-of-plane components of magnetization.
- (ii) We extend static RMOKE to a time-resolved technique by combining it with a free electron laser (FEL). We demonstrate this measurement system by tracking ultrafast magnetization reversal in a ferrimagnetic alloy.
- (iii) We explore whether time-resolved RMOKE can investigate sub-nanometer ultra-thin magnetic films on the sub-picosecond timescale. Thus far, this timescale has been investigated with time-resolved X-ray magnetic circular dichroism (TR-XMCD) using synchrotron radiation with a laser slicing technique. We compare the results measured with TR-XMCD using the slicing technique with time-resolved RMOKE using a FEL, assessing their signal-to-noise ratio and the measurement time.
- (iv) We develop an RMOKE measurement system using laboratory-based high-harmonic generation (HHG) laser, which generates ultrashort laser pulses in the EUV region. Experiments using an FEL cannot be run often, so we intend to develop a system using the HHG laser so as to complement FEL experiments. We demonstrate the first observation of RMOKE in an iron film involving polarization analysis with the HHG laser.
- (v) We explore whether RMOKE can be extended into the nonlinear regime. One feature of nonlinear RMOKE is the magnetization-induced second harmonic generation (SHG) in the resonant condition. We expect that this technique will add element specificity. Before exploring the nonlinear RMOKE technique, we must

deal with the SHG in the EUV / soft X-ray region under the resonant condition, which has not yet been reported. Therefore, our first challenge is observing SHG in the EUV / soft X-ray range.

1.3 Structure of this thesis

The detailed structure of the thesis is described in the following:

- Chapter 2 describes the background for this thesis, reviewing conventional techniques for probing static magnetization and magnetization dynamics at a sub-picosecond timescale. Here we show why we focus on measurement techniques in the EUV / soft X-ray region that can track magnetization dynamics on the sub-picosecond timescale.
- Chapter 3 describes light sources with a sub-picosecond pulse duration in the EUV / soft X-ray region. Currently, there are three sub-picosecond light sources in the EUV / soft X-ray region that are suitable for solid-state physics research. We compare the characteristics of these light sources to determine which sources are suitable for our measurements.
- Chapter 4 shows the development of the polar RMOKE measurement system and the first static M -edge polar RMOKE measurements of Ni thin films by using synchrotron radiation. The giant magneto-optical response is presented here.
- Chapter 5 describes our extension of the static RMOKE measurement developed in the previous chapter into the time-resolved measurement. In Sec. 5.2, we present the first time-resolved RMOKE (TR-RMOKE) measurements made using a FEL. In Sec. 5.3, we discuss the sensitivity of TR-RMOKE for measuring the magnetization dynamics of sub-nanometer ultrathin magnetic films. In Sec. 5.4, we present our RMOKE measurement system that uses a HHG laser.
- Chapter 6 describes our observation of the resonant enhancement of SHG in the EUV region. The research in this chapter is motivated by the desire to extend the RMOKE measurements into the nonlinear regime. Before performing nonlinear RMOKE measurements, we first tried to observe SHG in the EUV region, which has not yet been reported.
- Chapter 7 summarizes the major findings in this thesis and discuss future prospects.

Chapter 2

Historical overview of magneto-optical spectroscopy

The review of this chapter has been published as [8] (Publication list No. 6).

We have already seen the importance of magnetization dynamics in the sub-picoseconds timescale in Sec. 1.1. In this chapter, firstly the laser-induced transient states of magnetic systems are briefly introduced and the challenges in this research field are overviewed. The following section is a review of conventional techniques for studying the static and dynamical magnetization properties. Next, the necessity for developing the new soft x-ray measurement techniques in the linear (resonant MOKE) and non-linear (second harmonic generation) regime are explained. In Secs. 2.4 and 2.5, the details of magneto-optical effects are presented.

2.1 Laser-induced magnetization dynamics

Since the seminal work by Beaurepaire *et. al.* [10], which showed laser-induced demagnetization in the subpicoseconds timescale, a number of investigations on ferro-/ferrimagnetic systems have been performed in order to elucidate the mechanism responsible for the observed ultrafast magnetization behavior. The femtosecond laser pulses irradiated onto magnetic materials induce partial demagnetization in hundreds of femtoseconds. After the partial quenching, remagnetization to the initial state occurs in the picoseconds timescale. In some ferrimagnetic alloys, laser-induced magnetization reversal has been reported so far, which is the fastest manipulation of magnetization at

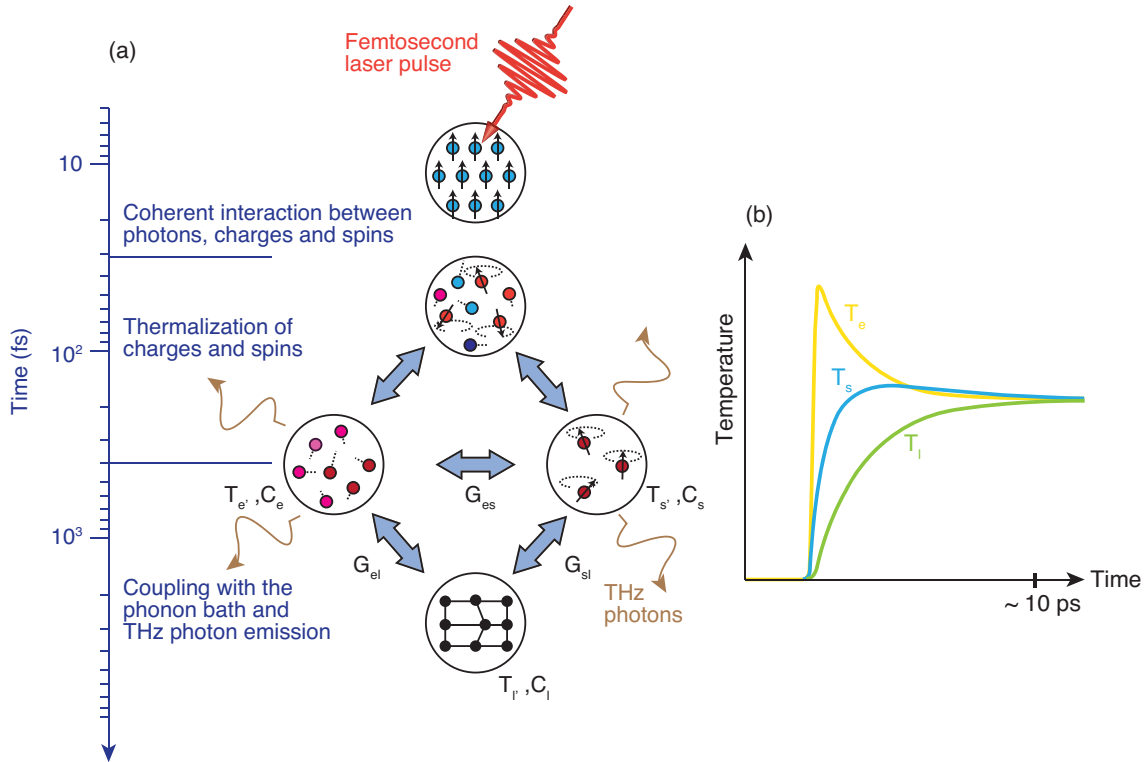


FIGURE 2.1: (a) Laser-induced processes that occur in ferromagnetic materials [9]. (b) Temperature variation with respect to time, where at time zero, a pulse laser irradiates the surface of a ferromagnetic material.

present. Some insights behind this transient magnetization behavior can be extracted from a phenomenological model, which treats the electron, spin and lattice (phonon) system separately. Fig. 2.1 (a) presents a series of proposed processes based on the phenomenological model combining with three-temperature model that each bath has its own temperature, T_e , T_s , and T_l with heat capacity, C_e , C_s , and C_l , where e , s and l express electrons, spins, and lattice, respectively. In this regime, the demagnetization is driven first by the coherent interaction between the photon field and charges/spins, which is followed by incoherent process during the thermalization of the electrons and charges. In the incoherent process, which means that the electronic wave functions have lost the phase information with respect to the excitation by the photons, the spin-flip processes occur, which results in demagnetization. The electron and spin baths interact with lattice (phonon) bath through the phenomenological coupling constant, G_{es} , G_{el} , and G_{sl} . In Fig. 2.1 (b), the typical time evolution of each temperature is shown. Electron heat capacity is much smaller than that of the lattice, so that the abrupt increase of T_e is induced by femtosecond pulses. The electron baths decay through

phonon cascades, which rises T_l with a time constant given by a electron-phonon coupling. At the same time, the part of the energy goes into the spin subsystem that causes spin-flip processes, which causes the decrease of magnetization. In a highly non-equilibrium state driven by intense femtosecond pulses, even with this phenomenological model, the details of the interactions underlying the laser-induced phenomena cannot be completely explained [11, 12]. Especially, the interpretation for the spin-flip processes and the path of the angular momentum is still lacking, while a number of attempts have been performed beyond the phenomenological model in the 1) theory of Stoner excitations, 2) (quasi)particle-mediated spin-flip mechanism including spin-orbit scattering and magnon excitations [13], 3) the direct interaction between photons and spins [9, 14], 4) the atomistic calculations, 5) microscopic three-temperature model based on Elliott-Yafet spin-flip scattering, and 6) the nonlocal framework of superdiffusive transport [15]. As we have seen in Sec. 1.1, the spin-orbit interaction and exchange interactions dominate in the laser-induced magnetization dynamics. These interactions are significantly altered at the interfaces of magnetic systems. Therefore, in the field of this research, it is important to reveal the role of interface in the magnetization dynamics, which calls new measurement schemes that can detect spin dynamics from a surface or interface with higher sensitivity than conventional methods.

2.2 Conventional methods

Figure 2.2 shows a variety of experimental techniques which have been facilitated to track transient magnetization behavior in earlier studies. Each technique is presented with regards to the timescale and the energy. The dynamical magnetization phenomena and pertinent optical transitions are also shown together. There are two regimes for the optical transitions: one from the viewpoint of the valence bands for energies in a few eV and the other from the viewpoint of the core states in the energies higher than those of the extreme ultraviolet (EUV) range. Sub-picosecond pulses for the core-level excitation, the free electron laser (FEL), the high harmonic generation (HHG) laser, and the laser slicing source, are presented with respect to the energy regions in which each source falls.

In the microwave \sim millimeter-wave region, magnetic resonance, for example, ferromagnetic resonance (FMR) [16], and antiferromagnetic resonance (AFMR) [17], have

been utilized to study the frequency of spin precession and the spin collective excitation modes, magnon. Brillouin light scattering (BLS) and Raman scattering techniques, which are classified as inelastic light scattering, are utilized for investigating the magnon as well. The spin precession and spin waves take place in a temporal domain of hundreds of picoseconds. Terahertz time-domain spectroscopy (THz-TDS) is directly able to measure the waveforms of ultrashort terahertz pulses [18]. Furthermore, in time-resolved regime, The target system can be pumped by THz pulses without being accompanied by heat dissipation. This means that heating effects can be excluded in analysis of transient magnetization phenomena [19]. In the infrared \sim the ultraviolet range, the magneto-optical technique have been used in either reflection (Kerr) or transmission (Faraday) scheme. Visible MOKE measurements with element selectivity were reported on specific magnetic compounds that consisted of transition-metals and rare-earths by using different wavelength for each target element [20]. Moreover, magnetic systems without inversion symmetry, such as systems involving surface and interface magnetism have been investigated by means of nonlinear magneto-optical techniques, magnetization-induced second harmonic generation (MSHG) [21, 22]. Although laboratory-based lasers can be employed for these techniques, they do not have element specificity because they are related with the optical transitions that take place between conduction and valence bands which do not localized to the particular element.

In the energy higher than the EUV range, element specific measurements are generally conducted by setting the photon energy to a particular inner-shell absorption edge. Static property of magneto-optical effects in the EUV \sim soft X-ray range were intensively studied over the last 20 years (see in Sec. 4.1.1). Measurement techniques, which can detect the component of $\langle M^2 \rangle$ are also utilized such as the X-ray magnetic linear dichroism (XMLD) [23] and Voigt effect [24]. Both the ferromagnetic and antiferromagnetic orders can be probed with these techniques. However, these methods, which are related to $\langle M^2 \rangle$ produce much smaller signals than those related to $\langle M \rangle$ [24, 25]. Furthermore, it is not clear to differentiate the magnetic-originated contributions from the nonmagnetic ones in XMLD measurements [26]. Especially in the soft X-ray range, X-ray magnetic circular dichroism (XMCD) is the most commonly utilized method for element-selectively probing ferro-/ferrimagnets. This technique employs circularly polarized light in this energy region. By combining with magneto-optical sum-rules, the spin and the orbital magnetic moment can be extracted separately from the XMCD measurements. Although the XMCD signals in the EUV region are much smaller than those in the soft X-ray region, a HHG laser with a circular polarization has been utilized for the demonstration of the M -edge XMCD in the EUV range for $3d$ transition

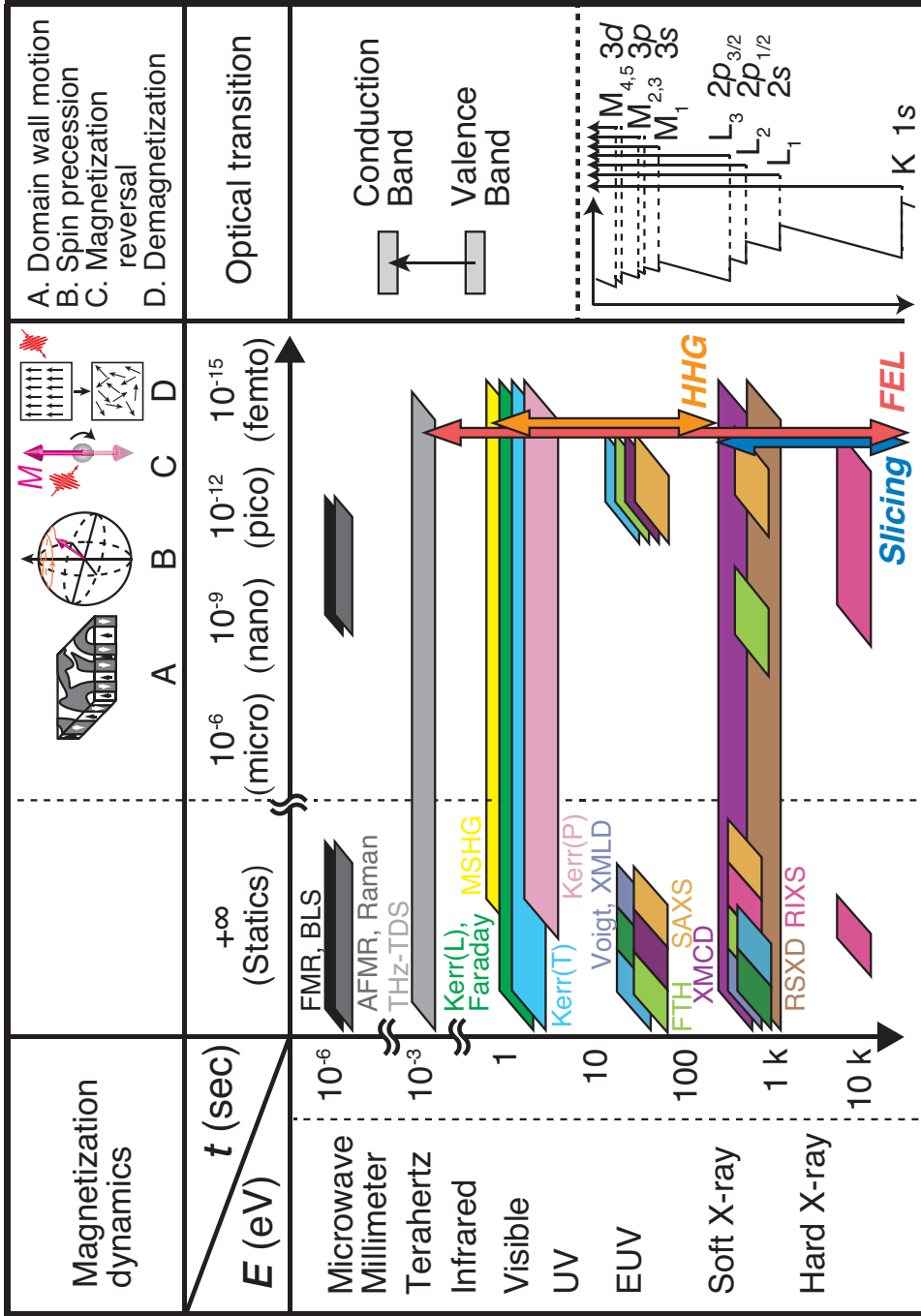


FIGURE 2.2: Experimental techniques that have been used to track transient magnetization behavior in the timescale from $+\infty$ (corresponding to static measurements) to 10^{-15} s (femtosecond scale) are shown with regards to the energies required with which each method has been utilized. The techniques are restricted to photon-in & photon-out regimes. With respect to Kerr techniques, P, L, and T represent the polar, longitudinal and transverse configurations, respectively. These geometries in the Kerr measurements are explained in the text. Dynamical magnetization behavior that takes place in each timescale are presented above the temporal axis. On the right side, the pertinent optical transitions are schematically illustrated. The core states are positioned for the 3d transition metals. Femtosecond pulses in the EUV \sim X-ray ranges, FEL, HHG and laser slicing sources, are shown with respect to their energy ranges and pulse durations. This figure has been taken from [8] (Publication list No. 6)

metals [27–29]. The resonant inelastic X-ray scattering (RIXS) technique is newer than the other magnetic probing techniques and is complementarily used with the inelastic neutron scattering [30–33]. This method has been more intensively utilized as a result of the increase of brilliance of third-generation synchrotron radiation (SR) and the advent of the FEL. Moreover, in parallel with the enhancement of the energy resolution, RIXS technique has a merit that it can be utilized to investigate magnetic collective excitations. Different from similar methods, RIXS can also be employed to study momentum-resolved information. Small-angle X-ray scattering (SAXS) has similarity to resonant X-ray scattering technique. SAXS can be employed to observe magnetic structures on the nanometer scale [34, 35]. The topological spin textures of the skyrmion has recently been investigated by using this method. Recent coherent light sources, for example HHG lasers and FELs, made it possible to conduct Fourier transform holography (FTH) in the EUV \sim soft X-ray ranges [36, 37]. In the conventional magnetic imaging scheme, magnetic transmission X-ray microscopy using zone plates has been utilized. This FTH technique, which is one of the holography measurements, does not need lens such as zone plate. While SAXS technique gives the average correlation length, the FTH technique can unveil the real-space magnetic distribution in the element-selective way. The resonant soft X-ray diffraction (RSXD) technique has been employed to study the spin, orbital, charge order and structural information of target elements, especially in strongly correlated systems like transition metal oxides. The magnetic structures of helimagnets and antiferromagnets can be determined by this technique. Resonant X-ray diffraction is also employed in the hard X-ray region for capturing the orbital and charges orders. It is of note that the cross section of magnetic scattering is much smaller in the hard X-ray region than that in the soft X-ray region [31, 38]. In addition, because the $3d$ states are in the soft X-ray region, resonant magnetic scattering is primarily employed in the soft X-ray region. One must keep in mind for RSXD measurements: (1) the attenuation length in the soft X-ray range is smaller ($\sim 100 - 200$ nm) than that in the hard X-ray range and that for neutron scattering; (2) because the soft X-ray wavelength is longer than that for the hard X-ray, the target ordering system is limited, with a typically periodic length of > 10 Å.

When it comes to transient phenomena of magnetization on a sub-picosecond timescale, the experimental methods presented above have been combined with the light sources above the EUV range such as HHG laser, laser slicing light sources and FELs. Recently, Transverse RMOKE (T-RMOKE) has been employed to investigate in-plane magnetization dynamics using an HHG laser in the sub-picoseconds timescale [15, 39, 40]. Regarding the combination with the FEL, only recently, time-resolved T-RMOKE

measurement has been demonstrated at FERMI@ELETTRA [41]. When a grating is utilized after the reflection from a sample, the transient RMOKE spectrum in the transverse geometry can be measured with an HHG laser that can emit the energy near the M -edge, which is the transition from $3p$ to $3d$, of the $3d$ transition metals. In the soft X-ray range, time-resolved XMCD (TR-XMCD) measurements have been combined with a laser slicing light source which covers the L -edge range, which is the transition from $2p$ to $3d$, for $3d$ transition metals [42, 43]. Recently, by using an HHG laser [44] and an FEL [45], M -edge TR-XMCD measurements have been demonstrated on $3d$ transition metals. These time-resolved reflectivity measurements with the use of linear (T-RMOKE) and circular polarization (XMCD) have had a crucial role in tracking transient in-plane magnetization in the earlier studies. A time-resolved RIXS (TR-RIXS) method using an FEL has also been performed in sub-picoseconds timescale [46]. This makes it possible to track the transient magnetic correlation with momentum resolution in the nanometer scale, which gives information on magnetic meltings in a variety of length scales. By using HHG lasers or FELs, a time-resolved SAXS (TR-SAXS) technique has been utilized to investigate the transient magnetization in the nanometer scale when demagnetization or magnetization reversal phenomena take place [47–49]. By using SR sources [50, 51] and an FEL [52], time-resolved FTH (TR-FTH) has been demonstrated. Because FELs have much higher brilliance and shorter pulse durations than those of SR sources, holographic measurements can be acquired in much shorter times when the FEL is utilized. By using a laser slicing source [53] and FELs [54, 55], time-resolved RSXD (TR-RSXD) for tracking transient magnetic orders with $q \neq 0$ (where q is the wave number) has been employed .

In Fig. 2.2, we focused only on measurement schemes with photon-in and photon-out setups. In these scheme, the existence of an external field does not affect the measurement system, which is the first requirement, **measurement under an external field**. This regime is important for measuring magnetic systems under *operando* conditions, for example application of magnetic or electric fields for both metals and insulators. It is of note that although time-resolved scanning tunneling microscopy and spin-polarized photoemission are not photon-out methods, these methods are considered to be important experimental options because they directly detect spin information.

2.3 Necessity of resonant magneto-optical techniques

In this section, we reveal why the development of the resonant magneto-optical techniques are required for satisfying the conditions as stated in the Sec. 1.1.

As we have already seen in the previous section, for the first requirement, **measurement under an external field**, photon-in & photon-out technique should be considered. In the energy range below \sim UV, averaged information of target samples are detected. However element specificity is added in methods that are related with a core-level excitation of a target sample. Therefore, for the second requirement, **element selectivity**, we focus on the techniques in the energy from EUV to soft X-ray range within the photon-in & photon-out regimes. According to the preceding element-selective methods described in the previous section, the following notable techniques are considered to be the candidates for meeting the requirements: time-resolved (TR) RIXS, TR-FTH, TR-SAXS, TR-RSXD, TR-RMOKE in a transverse configuration, and TR-XMCD.

Only recently, TR-RIXS has been utilized and combined with TR-RSXD. This method focuses on tracking the low-energy magnetic excitation mode. Therefore, this technique gives insight into the relation between magnetization reversal or demagnetization, and the magnetic correlated modes. However, along with TR-RIXS, the light-induced transient magnetization behavior in a macroscopic scale should be measured utilizing other techniques, such as TR-XMCD, TR-RMOKE for ferro-/ferrimagnetic orders and TR-RSXD for antiferromagnetic orders, which are classified as elastic scattering. TR-SAXS and TR-FTH are effective tools for determining the transient magnetic structures in the nanometer scale. However, these techniques, TR-FTH and TR-SAXS, are primarily utilized in the transmission configuration. When it comes to the measurements in the transmission geometry, a target sample should be thin enough to acquire a sizable transmission, especially in the soft X-ray range. TR-RSXD is employed for tracking the transient magnetic order with a certain periodic length, which is as large as the wavelength in the soft X-ray range, of materials with $q \neq 0$, for example antiferromagnets. If one is interested in the magnetization dynamics of ferro-/ferrimagnets, TR-RMOKE in the transverse geometry and TR-XMCD are preferred. In the TR-RMOKE in the transverse configuration, in-plane magnetization which is perpendicular to the incident plane can be detected (see the details of the explanation in Fig. 2.4). TR-XMCD is commonly employed with the energy near the L -edge region. Mostly, the L -edge TR-XMCD measurements in the sub-picoseconds timescale for the typical $3d$ transition metals are performed by using a laser slicing source in the

circular polarization mode. However, these measurements need to be done with much smaller photon flux, typically 10^3 /pulse for 0.1 % bandwidth [56], than those of SR and FEL sources [57]. Transient MCD signals are typically detected using a reflection geometry [58]. In the energy range of $100 \sim$ a few keV, where there are the L -edges of $3d$ transition metal, the light is strongly absorbed by the materials, so that the degree of freedom for the experimental setup is limited in the reflection geometry. To measure the out-of-plane magnetization, it is important to make the angle of incidence as close to the direction perpendicular to the sample surface as possible. However, the reflectivity (R) dramatically drops off with decreasing incidence angle, θ (with regard to the sample normal), and $R \sim 10^{-10} - 10^{-11}$ at $\theta = 45^\circ$ [59]. Therefore, for the reflection measurement in the energy region near L -edge for $3d$ transition metal, grazing incidence is necessary for raising the reflectivity, which results in the decrease of the magnetic contrast in the out-of-plane component of magnetization. Transient out-of-plane magnetization component can also be measured by utilizing the L -edge TR-XMCD in the transmission [42] and total fluorescence yield (TFY) modes [60]. However, the sample thickness should be thin enough to acquire high transmission in the former geometry. In the latter scheme, the detection scheme should be carefully constructed to collect a lower photon flux than that in the reflection/transmission scheme and to keep the pump light from entering the detectors.

In order to meet the third and fourth requirements, **the ability to trace out-of-plane magnetization dynamics with sub-picoseconds resolution**, we pay attention to the M -edge region for $3d$ transition metals, which is in the EUV range. In the energy range of $50 \sim 70$ eV, where there are the M edges of $3d$ -transition metal, materials absorb the light less than that in the L -edge region. Thus, at all incident angles, relatively sizable reflectivity can be acquired when compared with reflectivity measurement in the L -edge region. Out-of-plane magnetization can be detected by a MOKE measurement in the polar configuration, which the MOKE signals becomes maximum at normal incidence. However, even under this normal incidence condition, there is a larger signal-to-noise ratio in the M -edge than in the L -edge region. These facts mean that for detecting out-of-plane component of magnetization dynamics in the sub-picoseconds timescale, the freedom of the experimental configuration in the M -edge region is larger than in the L -edge region.

Although most of the preceding TR-XMCD was conducted in the L -edge range as described above, we here consider the applicability of the TR-XMCD in the M -edge range. The magnitude of the M -edge XMCD is much smaller than that in the L -edge region. Additionally, while the L -edge XMCD can extract the orbital and spin

magnetic moment by using the magneto-optical sum rule (see Sec. 2.5.1), this cannot be applied for the M -edge XMCD. Because the spin-orbit splitting is smaller in the M -edge region than that in the L -edge region, which makes it ambiguous to define the range of multiplet peaks. Furthermore, because it is difficult to incorporate the Coulomb interaction, the sum rule cannot be fully applied for the XMCD in the M -edge range. That is why the spin/orbital magnetic moments differ between those obtained from the M -edge and L -edge XMCD measurements [61].

Because of the deficiency regarding the detection of out-of-plane magnetization dynamics in the conventional element-selective techniques within photon-in & photon-out regimes, (TR)-RMOKE technique with polarization analysis in the M -edge range is needed for detecting the out-of-plane magnetization, which is the third and fourth requirements (**the ability to trace out-of-plane magnetization dynamics with sub-picoseconds resolution**). In addition, combining with FEL, the fifth requirement, **sensitivity to subnanometer-scale system**, is also met due to the high brilliance of the FEL. In the previous techniques, MOKE measurements with polarization analysis have been conducted in the optical regions. In this thesis, we extend the MOKE with polarization analysis into the EUV & soft X-ray range, we call RMOKE, and apply it to the time-resolved measurements in a sub-picosecond timescale with a free electron laser. This new technique developed in this thesis has the following properties in addition to the five features described in Sec. 1.1: (1) M -edge measurement feasibility, (2) use of linearly polarized pulses, (3) measurements of both rotation and ellipticity, and (4) extension to the nonlinear regime.

(1) M -edge measurement feasibility

In the preceding theoretical study regarding RMOKE with polarization analysis, it is expected that the RMOKE in the M -edge range gives the same order as that in the L -edge range [62, 63]. Furthermore, taking advantages of large degree of freedom for the experimental setup in the M -edge range, depth resolved RMOKE measurements is expected to be possible by varying the incident angle.

(2) Use of linearly polarized pulses

In TR-RMOKE measurements, linear polarization is utilized. Ellipsometry reveals the polarization state for the RMOKE measurements in the polar (P-RMOKE) and the longitudinal (L-RMOKE) configurations. On the other hand, TR-XMCD measurements utilize circular polarization. Circularly polarization can be employed at the Linac Coherent Light Source (LCLS) and FERMI@Elettra facilities [64–66] among the currently

operating FEL facilities in the EUV \sim soft X-ray region. However, to reveal the transient magnetization behavior, it is required to determine the accurate degree of circular polarization in advance, which is the energy dependent. In this sense, a measurement technique with linear polarization are suitable for analyzing the magnetic response extracted from the magneto-optical dynamics. Recently, circular polarization of HHG lasers in the EUV range has been generated by the use of a variety of techniques, such as use of two circularly or linearly polarized light at slightly different wavelengths and of a phase-shifter [29, 67]. However, HHG lasers give smaller intensities than that of FELs, so that an FEL source is favored in some cases when one is interested in investigating the dynamics of weak magnetic signals such as an ultrathin magnetic layer and a diluted magnetic systems.

(3) Measurement of both rotation and ellipticity

While XMCD only detects the ellipticity, in principle, MOKE measurements can measure both ellipticity and rotation. The rotation and the ellipticity are related to the nondiagonal component of the permittivity tensor [68]. In previous studies, the permittivity in the energy ranging from EUV to soft X-ray was determined indirectly with a certain magnitude of errors. However, RMOKE measurements in the energy range makes it possible to directly determine the nondiagonal component of permittivity tensor that gives magnetic information.

Measuring both the rotation and the ellipticity gives another merit. In the time-resolved measurement, through the combination of the rotation and the ellipticity signals, intrinsic magnetic signals can be extracted from the time-dependent magneto-optical signals. This is described in details in Sec. 5.1.2.

(4) Extension to the nonlinear regime

RMOKE measurements using an FEL gives another possibility for the detection of nonlinear signals, which is quite important in investigating the system without inversion symmetry element selectively. This gives the opportunity to conduct surface/interface-selective measurements, which is important for studying of spintronic materials such as spin-valve, magnetoresistive and magnetic topological insulator systems. In the visible region, MSHG is conventionally utilized, as shown in Fig. 2.2. It was reported that the rotation angle of polarization axis of second harmonics shows much larger than that of fundamental wave [69]. This possibility is explored in Chapter 6.

In the following section, firstly, in Sec. 2.4 we give an explanation for MOKE in terms of its phenomenological model, physical pictures, preceding studies in the visible

range, and the comparison between visible and soft x-ray regime. The extension into the nonlinear regime is also addressed. Furthermore preceding studies on MOKE for 3d transition metals, Fe, Co, and Ni are overviewed. In Sec. 2.5, we introduce XMCD technique and how magnetic moments can be extracted using the magneto-optical sum rules.

2.4 Magneto-optical Kerr effect

Before introducing the MOKE in details, we define the word "visible" here. Strictly speaking, the visible region is approximately 380–780 nm of the wavelength, the range which can be detected by the human eye. However, in this thesis, we will use "visible" to refer to all energies below 10 eV (124 nm) for distinguishing this energy range related to nonresonant experiment with EUV \sim soft X-ray range, which is involved with resonant measurements.

First, we focus on the magneto-optical (MO) effect, which refers to the interaction between light and magnetized materials. This effect has been used to study static bulk [68] and surface [70] magnetism, spin dynamics [11] and spin transport using MO microscopy with lateral resolution. Most MOKE experiments have been conducted utilizing linearly polarized laser light typically in the visible region.

Figure 2.3 shows a schematic of the magneto-optical (MO) effect, which is called the Kerr effect when considering reflection measurements or the Faraday effect when considering transmission measurements. The Kerr and Faraday effects show basically the same phenomena. The MO effect can be characterized by rotation and ellipticity, as explained in Fig. 2.3. Linearly polarization can be decomposed into two orthogonal (left and right) circular polarization components (Fig. Fig. 2.3 top), which have the same amplitude and phase velocity. When linearly polarized light interacts with a magnetized material, the polarization state changes in two ways. The first is a change in rotation of the polarization axis (Fig. 2.3 middle left), and the second is a change from linear to elliptical polarized light (Fig. 2.3 middle right). The phase variation between the right- and left-circularly polarized light causes the rotation, and the variation between amplitudes causes the ellipticity. These two effects appear in the reflected (transmitted) light for the Kerr (Faraday) effect shown at the bottom of the figure. In this thesis we focus on the Kerr effect, represented by the Kerr rotation angle, θ_K . Ellipticity is defined by $\eta_K = \arctan(b/a)$, where a and b are the minor and major axes of the ellipse, respectively. We do not consider η_K in this thesis.

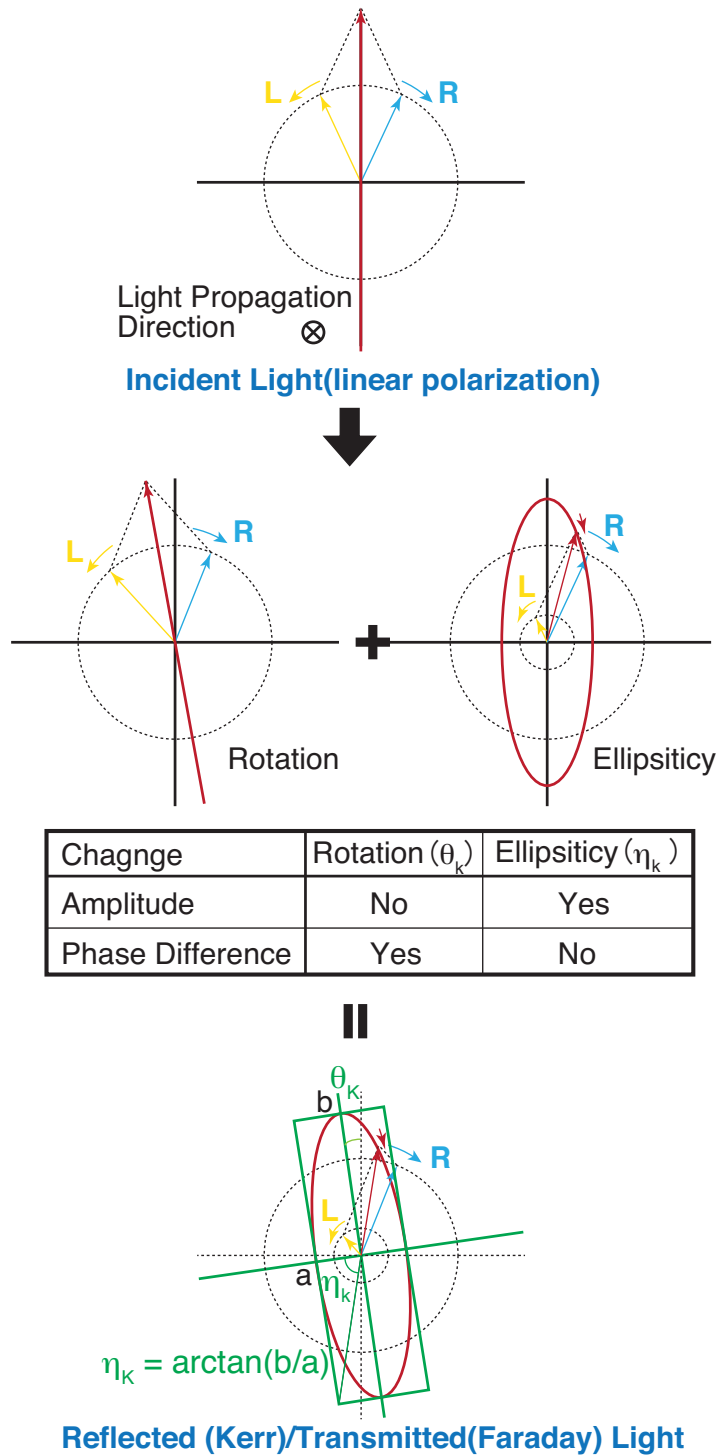


FIGURE 2.3: Schematic of the magneto-optical effect. The magneto-optical effect is characterized by rotation and ellipticity. L and R denote the left and right components of circular polarization.

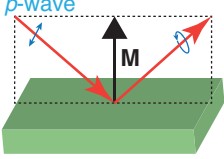
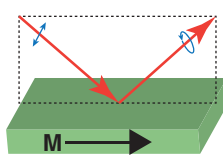
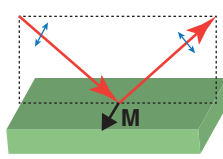


Name	(a) Polar	(b) Longitudinal	(c) Transverse
Geometry			
Detection	Out-of-plane	in-plane	in-plane
Polarization Variation	Rotation Ellipticity		None 
Measurement	Polarization Analysis		Intensity measurement

FIGURE 2.4: Schematic diagram of MOKE measurement configuration assuming that incident light has p -polarization. The dashed line in the "Geometry" row represents the incident plane. In the "Polarization Variation" row, the polarization-state changes that are projected in the plane that lies normal to the light direction are given for both incident (left) and reflected light (right). This figure has been taken from [8] (Publication list No. 6)

Figure 2.4 shows the measurement geometry. There are two main techniques used to measure MOKE. One analyzes polarization: the polarization of reflected light rotates and changes its ellipticity, as shown in Fig. 2.4(a), (b). The other measures intensity and the reflected-light polarization states do not vary from that of the incident light, as shown in Fig.2.4(c) (transverse MOKE, T-MOKE). The former group is further divided into two geometries. When magnetization, \vec{M} , is perpendicular to the sample surface, it is called polar MOKE, P-MOKE as shown in Fig. 2.4(a). If \vec{M} lies both in the sample surface and the incident plane that is made by incident and reflected light axis, it is called longitudinal MOKE, L-MOKE, as shown in Fig. 2.4(b)). Historically, (a) and (b) were recognized as separate geometries, but the MOKE signal involving polarization analysis for (a) and (b) originates from $\vec{k} \cdot \vec{M}$, where \vec{k} represents the wave vector of the incoming light. Therefore, between the two configurations there is no intrinsic difference. External magnetic field is applied to make magnetization direct to the specific direction described above in each MOKE geometry as shown in Fig. 2.4. If the external field is applied in the arbitrary direction, magneto-optical effects comes from the combination of the three configurations. The earlier studies formulated the analytical and phenomenological expressions in such cases [71, 72]. Fresnel coefficients define θ_K and η_K , which are dependent on an incident light frequency (ω) as shown in Sec. 2.4.3. The RMOKE is defined when measurements are performed under $\omega \approx \omega_{\text{res}}$, where ω_{res} represents an inner-shell absorption edge of target magnetic element.

2.4.1 Phenomenological description

Here, we show the expression for polar MOKE that is used in this thesis. The derivation of the expression follows from [68]. We assume that the incident light impinges on a magnetic medium with the incident angle ϕ_i ($0^\circ < \phi_i < 90^\circ$). The Kerr rotation (θ_K) and ellipticity (η_K) for s -polarized (p -polarized) incident light can be expressed as θ_{Ks} and η_{Ks} (θ_{Kp} and η_{Kp}). These are given by using Fresnel coefficients: r_{ss} , r_{pp} , r_{sp} and r_{ps} . r_{ij} is defined as follows:

$$\tilde{r}_{ij} = \frac{E_1^i}{E_0^j} \quad (2.1)$$

where E_1 and E_0 are the electric field of reflected and incident light, respectively, and the superscript expresses the s or p component. The tilde means that the quantity is complex. These Fresnel coefficients are expressed by:

$$\tilde{r}_{ss} = \frac{n_0 \cos \phi_i - \bar{n} \cos \phi_t}{n_0 \cos \phi_i + \bar{n} \cos \phi_t} \quad (2.2)$$

$$\tilde{r}_{pp} = \frac{\bar{n} \cos \phi_i - n_0 \cos \phi_t}{\bar{n} \cos \phi_i + n_0 \cos \phi_t} \quad (2.3)$$

$$\tilde{r}_{ps} = \frac{in_0(n_+ - n_-)\cos\phi_i}{(\bar{n}\cos\phi_t + n_0\cos\phi_i)(\bar{n}\cos\phi_i + n_0\cos\phi_t)\cos\phi_t} \quad (2.4)$$

$$\tilde{r}_{sp} = \tilde{r}_{ps} \quad (2.5)$$

where \bar{n} (n_0) is the refractive index of the (non-)magnetic medium ($\bar{n} \sim \frac{1}{2}(n_+ + n_-)$). ϕ_t (ϕ_i) is the refraction (incident) angle. The subscript + (-) indicates the the helicity of the circular polarization. The Kerr rotation and the ellipticity are expressed using the Fresnel coefficients:

$$\theta_{Ks} + i\eta_{Ks} = -\frac{\tilde{r}_{ps}}{\tilde{r}_{ss}} \sim \frac{-in_0\bar{n}Q}{\bar{n}^2 - n_0^2} \left(\frac{\cos\phi_i}{\cos(\phi_i - \phi_t)} \right) \quad (2.6)$$

$$\theta_{Kp} + i\eta_{Kp} = \frac{\tilde{r}_{sp}}{\tilde{r}_{pp}} \sim \frac{-in_0\bar{n}Q}{\bar{n}^2 - n_0^2} \left(\frac{\cos\phi_i}{\cos(\phi_i + \phi_t)} \right) \quad (2.7)$$

where θ_{Kp} (η_{Kp}) and θ_{Ks} (η_{Ks}) are Kerr rotation angle (Kerr ellipticity) for p - and s -polarized incident light, respectively. Q is the Voigt parameter defined by $Q = \frac{i\eta_{xy}}{\eta_{xx}} \sim \frac{n_+ - n_-}{\bar{n}\cos\phi_t}$. The refractive index can be converted into dielectric tensors, (ϵ), through the relation extracted from Fresnel equation [68]. The rigorous expression of the ϵ is given in Sec. 2.4.2.

2.4.2 Physical picture

Classical picture of MOKE

From the classical point of view, the magneto-optical phenomena can be understood by regarding the electrons in the material as the damped oscillator. In this regime, a periodic field (\vec{E}) of the electromagnetic light makes electrons in the material oscillation, which is simultaneously affected by a magnetic field (\vec{B}) in the form of the Lorenz term. This is described by

$$\ddot{\vec{r}} + \gamma\dot{\vec{r}} + \omega_0^2\vec{r} = \frac{q}{m}(\vec{E} + \dot{\vec{r}} \times \vec{B}) \quad (2.8)$$

where \vec{r} is the displacement of the electrons, m (q) is the electron mass (charge), and γ is the collision probability given by $1/\tau$ (τ is the relaxation time of the scattering). ω_0 is the resonance frequency of the undamped oscillator.

In this regime, the polarization of electrons is induced in the direction of the electric field of incident light under a magnetic field in a certain direction. In the polar or longitudinal geometry, the magnetic field induces the perpendicular component in the electron motion with respect to the polarization direction of the incident light. This gives the dipole radiation in the reflected light, which results in the deviation of the light polarization from the initial linear polarization. In the transverse geometry, the field only changes the amplitude of the electron oscillation, which gives the reduction of the reflected intensity and does not contain the rotation of the principal axis of the polarization, and the change from a linear to an elliptical polarization.

If we assume that the magnetic field has only z component $\vec{B}=(0,0,B)$ (polar geometry), then non-zero dielectric tensors are given as follows:

$$\begin{aligned} \epsilon_{xx}(\omega) &= 1 - \frac{nq^2}{m\epsilon_0} \cdot \frac{\omega^2 + i\omega\gamma - \omega_0^2}{(\omega^2 + i\omega\gamma - \omega_0^2)^2 - \omega^2\omega_c^2} \\ \epsilon_{xy}(\omega) &= \frac{nq^2}{m\epsilon_0} \cdot \frac{i\omega\omega_c}{(\omega^2 + i\omega\gamma - \omega_0^2)^2 - \omega^2\omega_c^2} \\ \epsilon_{zz}(\omega) &= 1 - \frac{nq^2}{m\epsilon_0} \cdot \frac{1}{\omega^2 + i\omega\gamma - \omega_0^2} \end{aligned} \quad (2.9)$$

where ω is the frequency of the incident light, n is the electron density, and ω_c is the cyclotron frequency given by $|qB/m|$. This tells that the linear dependence of the dielectric tensor on magnetization is in the off-diagonal component. It is of note that if the ω is close to the ω_0 , the magneto-optical response is enhanced, which is expected in the resonant MOKE scheme.

This classical picture can explain the magneto-optical response in the system where free electrons dominate the interaction with the light such as nonmagnetic semiconductors. However the magneto-optical response of ferromagnets which show spontaneous magnetization cannot be well described with this regime. This required the formalization based on a quantum theory.

Quantum picture of MOKE

The dielectric tensor based on the quantum mechanics can be derived from the Kubo formula in the framework of the linear-response theory. This gives dynamical response of dielectricity. We focus on the microscopic nature of MOKE in a quantum mechanical regime, so only results of the dielectric tensor derived from this theory are given here (the details of the derivation can be found in Ref. [73, 74].)

$$\begin{aligned}\epsilon_{xx}(\omega) &= 1 - \frac{Nq^2}{2m\epsilon_0} \sum_n (\rho_n - \rho_m) \frac{(f_x)_{mn}}{\omega_{mn}^2 - (\omega + i\gamma)^2} \\ \epsilon_{xy}(\omega) &= i \frac{Nq^2}{2m\epsilon_0} \sum_n (\rho_n - \rho_m) \frac{\omega_{mn} \Delta f_{mn}}{\omega_{mn}^2 - (\omega + i\gamma)^2}\end{aligned}\tag{2.10}$$

where N is the electron-dipole density, $\omega_{mn} = \omega_m - \omega_n$, $(f_x)_{mn} = \frac{2m\omega_{mn}}{\hbar} \cdot | \langle m|x|n \rangle |$, $\rho_n = \frac{\exp(-\hbar\omega_n/kT)}{\sum_n \exp(-\hbar\omega_n/kT)}$, and $\Delta f_{mn} = f_{mn}^+ - f_{mn}^-$. $f_{mn}^\pm (= \frac{m\omega_{mn} |\langle m|x^\pm|n \rangle|^2}{\hbar})$ is the oscillator strength for right and left-circularly polarized light. qx^\pm correspond to electric-dipole operators for right- and left-circularly polarized light. The direction of the electric field is assumed to be in the y direction. These formula show that the dielectric tensor is expressed by a superposition of the dispersion formula based on optical transitions.

The dielectric tensor defines the degree of material polarization due to a perturbation by electric fields of electromagnetic light. Electronic wave function for the perturbed system can be expanded by the Fourier series of eigen functions of the unperturbed system. Therefore, the Eq.2.10 tells that through the perturbation of the electric fields

of incoming light, the excited state of the unperturbed system is partly incorporated into the ground state for the perturbed system, which causes the polarization through the modification of spatial distribution of electrons. The excited states are mixed into the ground state depending on the oscillator strength, f , and the energy denominator, $1/(\omega - \omega_{mn})$.

The off-diagonal component of the dielectric tensor is non-zero, which gives the magneto-optical response, when the followings are met: i) In a transition from ψ_n to ψ_m state, the oscillator strength for right- (f_{mn}^+) and left-circularly (f_{mn}^-) polarized light are different. The difference of the central frequencies of the transitions induced by right- and left-circularly polarized light is one of the contributions for causing the finite value of Δf_{mn} . ii) Distribution function ρ is different depend on each state n .

The effect of magnetic fields does not clearly appear in Eq. 2.10 like ω_c in Eq. 2.9. We see the influence of the magnetic field by using Fig. 2.5 [75]. Matrix elements of electric dipole transitions become nonzero when an initial and a final state have the same wave vector, which means the only direct transitions are related to magneto-optical effects. Furthermore, for the electric dipole transition, the selection rules are imposed for the orbital and magnetic quantum number as follows:

$$\begin{aligned}\Delta l &= \pm 1 \\ \Delta m &= 0, \pm 1\end{aligned}\tag{2.11}$$

The transition of $\Delta m_l = +1$ (-1) is caused by right(left)-circularly polarized light. Fig. 2.5 shows the transitions from d_{xz} and d_{yz} states to a p_z state by right- and left-circularly polarized light. The d_{xz} , d_{yz} and p_z states correspond to $|l, m_l \rangle = |2, +1 \rangle$, $|2, -1 \rangle$ and $|1, 0 \rangle$, respectively. If there is a spontaneous magnetization or external magnetic fields, spin-up and spin-down states, shown by \uparrow and \downarrow respectively in Fig. 2.5, are lifted with the difference of exchange splittings (Δ_{EX}). Furthermore, orbital degeneracy is lifted by spin-orbit splitting (Δ_{SO}). For d_{xz} and d_{yz} , they become $d_{(x+iy)z}$ ($|l, m_l \rangle = |2, 1 \rangle$) and $d_{(x-iy)z}$ ($|l, m_l \rangle = |2, -1 \rangle$). The transition induced by right- and left-circularly polarized light is shown with red and blue line, respectively. Fig. 2.5(a) shows the magneto-optical response with the finite Δ_{EX} and Δ_{SO} , and (b) ((c)) corresponds to the response with Δ_{SO} (Δ_{EX}) and without Δ_{EX} (Δ_{SO}). The absorption spectrum is shown in the right panel for the transition caused by opposite photon helicities. Only in the case with a finite Δ_{EX} and Δ_{SO} , the left- and right-

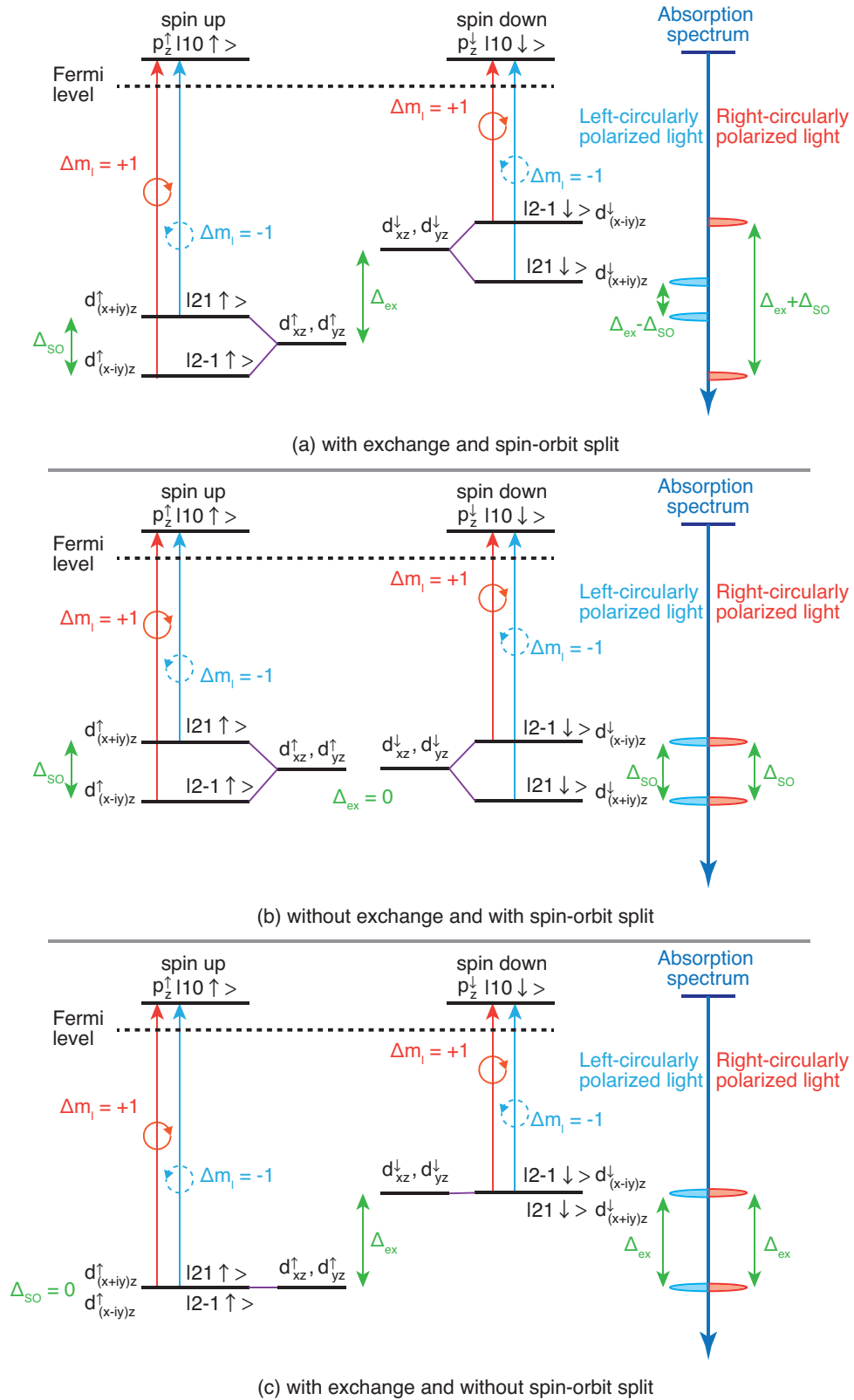


FIGURE 2.5: The role of selection rule of dipole transition, exchange interaction and spin-orbit interaction in magneto-optical effects. The transition from d_{xz} and d_{yz} to p_z state is shown. In the right part, absorption spectrum is shown for the transition caused by left- (blue) and right-circularly (red) polarized light.

circularly polarized light is absorbed differently, which causes nonzero value of non-diagonal component of dielectric tensor. This gives the magneto-optical response, the rotation of the principal axis of the polarization and the change of polarization state from the linear to the elliptical polarization. Furthermore, this schematic diagram also tells that depending on the difference of absorption between right- and left-circularly polarized light at each energy position, the magneto-optical signals can be positive or negative. This behavior is observed in magnetic metals as shown in the next section.

2.4.3 Preceding studies of visible MOKE

In this section, we review the studies of $3d$ transition metals that use MOKE in the visible region. In $3d$ transition metals, the MO effect in metals mainly originates from the difference in interband transitions between right- and left-handed polarized light. The MO measurements of these elements contributed to theoretical development by providing information on the bandwidth and the influence of the spin-orbit effect. MO spectroscopy played a crucial role in testing whether local spin-density approximation (LSDA) band theory could be applied to Fe, Co and Ni.

The magnetism of the $3d$ transition metals Fe, Co, and Ni, has been widely investigated for more than half a century. $3d$ electrons have an itinerant character whereas $3d$ orbitals are relatively localized. Along with the development of a theoretical approach to describe the bands for these elements, it was found that a band theory, based on itinerant character and using either the LSDA or the generalized gradient approximation (GGA), agreed very well with experimental data such including the spin magnetic moment, exchange splittings, Fermi surface cross-sections, Curie temperatures, spin-wave-stiffness constant, and spin-wave dispersion.

First, we review the visible MOKE spectra of Fe. Bulk crystalline Fe is known to have either bcc (α -Fe) or fcc (γ -Fe) structure. Because γ -Fe is not stable at low temperature, the optical and MO spectra were only investigated in *alpha*-Fe. Therefore, here we only focus on α -Fe. For bcc Fe, the hard magnetization axis lies in the $\langle 111 \rangle$ direction and the easy axis in the $\langle 100 \rangle$ direction. The Kerr angle (θ_K) and ellipticity (η_K) spectra measured at room temperature, reported independently, are shown together with calculated results [78] in Figure 2.6. The minimum value near 1 eV in θ_K and near 2 eV in η_K can be well reproduced by incorporating the contributions from intraband Drude conductivity. When only interband transition

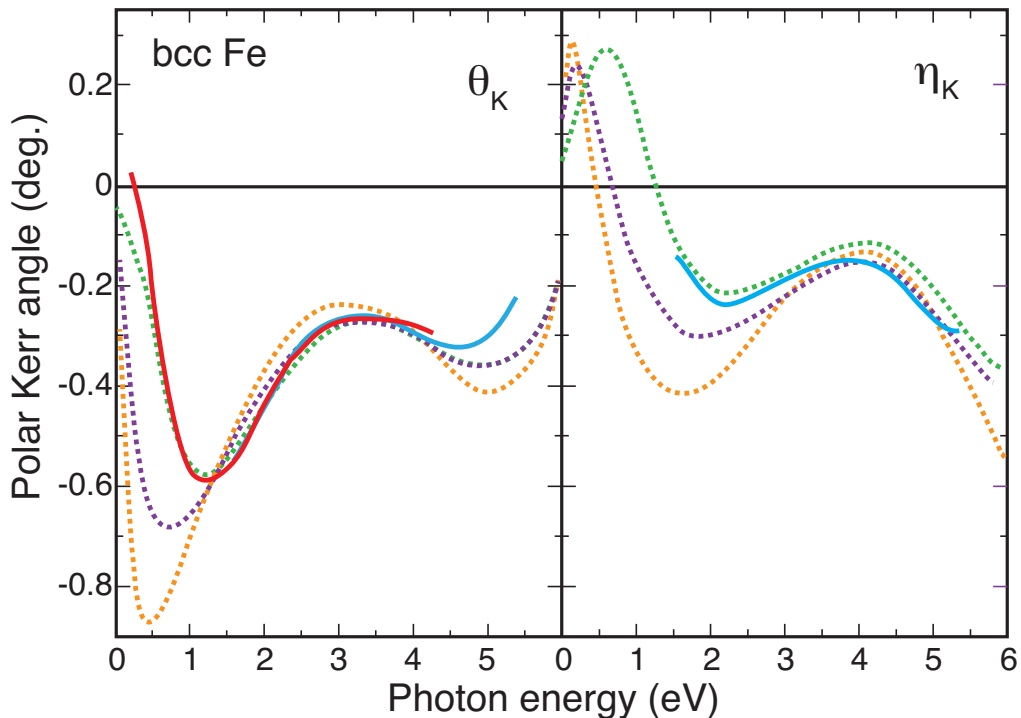


FIGURE 2.6: Experimental (solid lines: red from Ref. [76], blue from Ref. [77]) and calculated (in part from [78]) spectra for visible P-MOKE in Fe. All curves are traced from Ref. [68]. These calculations assumed only interband transition with two lifetime parameters, $\hbar\delta = 0.03$ Ry (orange dashed line) and 0.05 Ry (purple dashed line). Green dashed line is calculated by accounting for the intraband Drude term, which is crucial in the MO response below 1 eV.

is considered, the calculation gives larger θ_K than that taken into account the influence of the intraband transition. The intraband conductivity is approximated by the phenomenological Drude expression [78]. The agreements between experiments and calculations, both in the overall features and magnitude, show that LSDA band theory correctly describes the occupied and unoccupied energy bands and exchange splittings. The maximum magnitude of the Kerr rotation angle, **0.6 degree**, was observed around 1 eV for polar MOKE (P-MOKE) in Fe. To reproduce the zero-crossing below 0.5 eV observed in experiments, a large Drude relaxation time should be incorporated. Extending the energy region up to 10 eV and testing theoretical schemes, it was found that the full-potential linearized augmented plane wave method agrees more with experimental data than does the augmented plane wave spherical-potential calculation.

Second we assess the visible MOKE of Co. Co crystalizes in an hcp or fcc structure depending on temperature. For hcp (fcc) Co, the hard magnetization axis lies in

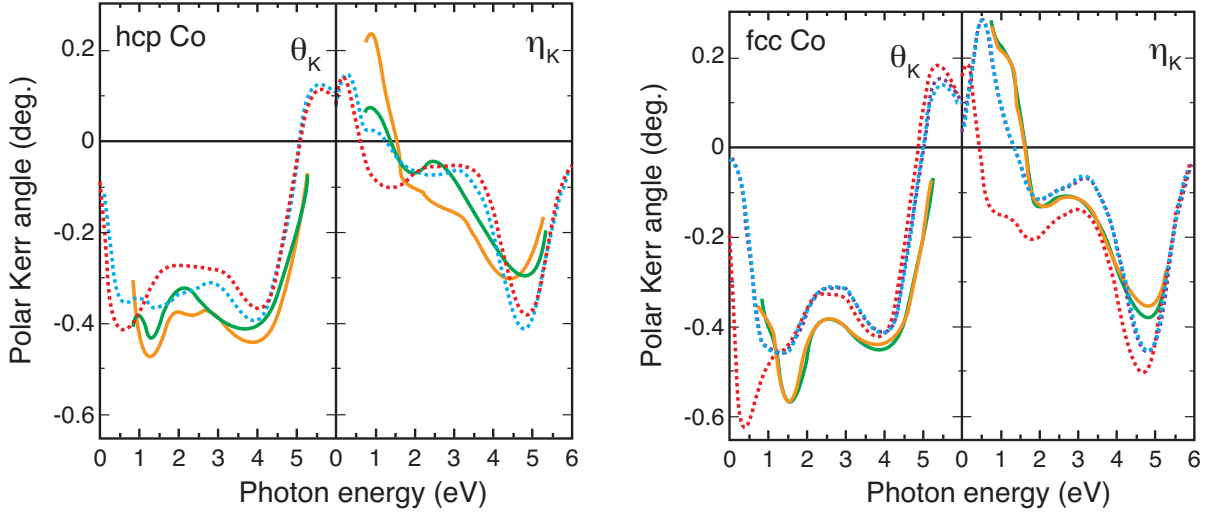


FIGURE 2.7: Experimental (solid lines, Ref. [79]) and calculated (dashed lines, [80]) spectra for visible P-MOKE for (left) hcp Co and (right) fcc Co at room temperature. All curves are traced from Ref. [68]. MO spectra are shown for two crystals with different crystal axes: (left) Co(0001) (green) and Co(11 $\bar{2}$ 0) (orange), (right) Co(001) (green) and Co(110) (orange). (left) Calculations assumed only interband transition with a lifetime parameter, $\hbar\delta = 0.03$ Ry for Co(0001) (red) and Co(11 $\bar{2}$ 0) (blue). (Right) Two calculated curves for Co(001) and one curve for Co(110) are shown for both θ_K and η_K spectra. One of the former curves is calculated for 3.9 % larger lattice constant system assuming interband-only Kerr effect (red) and the other of the former curves is calculated including the effect of the intraband Drude term (blue). The latter curve (purple) is calculated with the same conditions as above but for the Co(110) system.

the $\langle 1000 \rangle$ ($\langle 100 \rangle$) direction and the easy axis in the $\langle 0001 \rangle$ ($\langle 111 \rangle$) direction. Because of technological advances in fabricating magnetic thin films, fcc Co has been fabricated at low temperature [81, 82]. Figure 2.7 shows the Kerr angle (θ_K) and ellipticity (η_K) spectra obtained from experiments at room temperature for hcp Co(0001), Co(11 $\bar{2}$ 0), fcc Co(001) and Co(110) are displayed together with calculations in Fig. 2.7 [68, 79]. The calculated lines reproduce the overall shapes from experimental data, but the calculated peak positions and magnitudes do not agree well with experimental data. These discrepancies appear to originate from the LSDA band theory, which predicts a larger d -bandwidth than the experimental results. The hcp Co has an uniaxial structure, so the Kerr spectrum depends on the magnetization orientation (Kerr anisotropy), which is also expected in the orbital moment and anisotropy energy. The MO spectrum depends on growth orientation in hcp Co, as shown in Fig. 2.7, but not in fcc Co. For

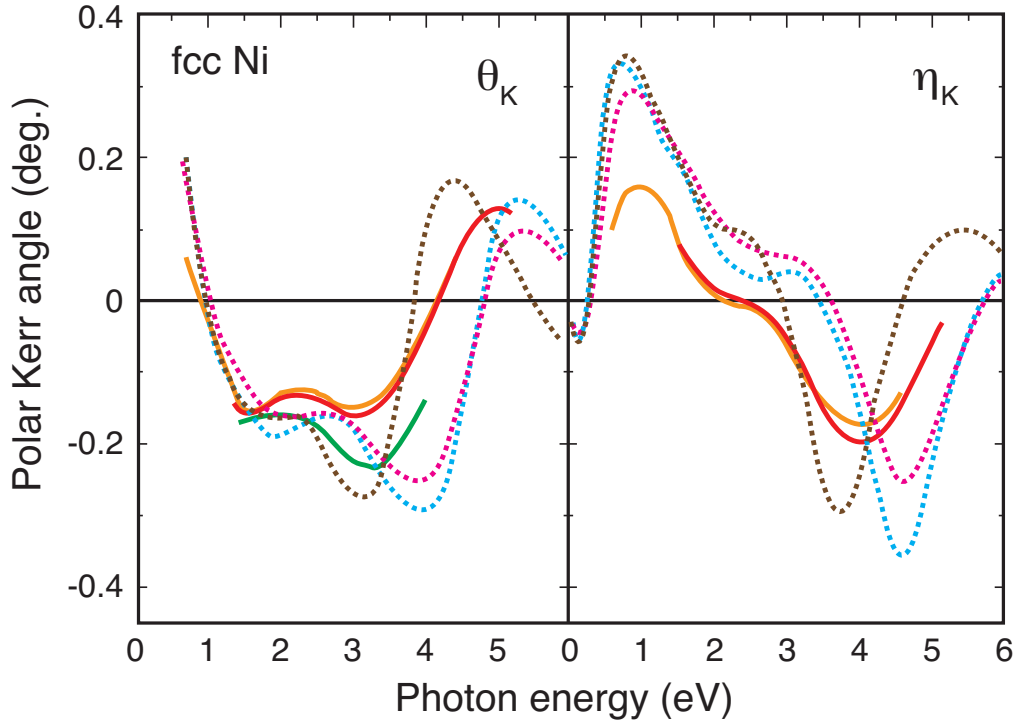


FIGURE 2.8: Experimental (solid lines: orange from Ref. [83], red from Ref. [84], and green from Ref. [85]) and calculated spectra for visible P-MOKE in Ni. All curves are traced from Ref. [68]. The calculations (dashed curves) assumed only an interband transition with two lifetime parameters: 0.03 Ry (blue) and 0.04 Ry (pink). The brown dashed line is calculated for a 5.9 % larger lattice constant, which shows smaller bandwidth.

fcc Co, the curve for Co(001) and Co(110) cannot be distinguished because they overlap. The Kerr anisotropy of hcp Co shows a maximum near 2–3 eV and this feature is reproduced in the calculated results, especially for θ_K . At energies below ~ 1.5 eV, the η_K spectra show a difference between Co(0001) and Co(11 $\bar{2}$ 0), but this deviation came from the difference in the Drude contribution to the MO spectra because different crystals were measured. Therefore true Kerr anisotropy should appear at the energies above ~ 1.5 eV, where the Drude contribution does not affect the MO spectra. The Kerr anisotropy has been shown to originate from the anisotropy of both the diagonal and off-diagonal components of the conductivity tensor [80]. The maximum magnitude of the Kerr rotation angle, **0.5 degree** (hcp Co) and **0.55 degree** (fcc Co), appeared near 1.5 eV, observed using P-MOKE at room temperature. The larger Kerr rotation in fcc Co than in hcp Co originates from the difference in the diagonal conductivity tensor. This difference does not originate from the magnetization difference due to its

structural difference. Calculations have shown that fcc and hcp Co have fairly similar total moments.

Finally, we assess the visible MOKE of Ni. For fcc Ni, the hard magnetization axis lies in $\langle 100 \rangle$ direction and the easy axis in the $\langle 111 \rangle$ direction. The Kerr angle (θ_K) and ellipticity (η_K) spectra measured at room temperature [83, 84] and 84 K [85], reported independently, are shown together with the calculation in Figure 2.8. The maximum magnitude of the Kerr rotation angle, **0.15 degree**, appears near 1.5 and 3 eV using P-MOKE for Ni at room temperature. Notably, the Ni band structure depends on temperature, so the exchange splitting decreases with increasing temperature. This behavior means the MO spectra depends on temperature. Figure 2.8 suggests that the minimum peak near 3 eV changes with temperature. The LSDA band theory predicts a broader d band width and larger exchange splittings than the experimental values. Because of the lack of strong correlations in the LSDA method, the band theory predicts bands that are too broad and gives a discrepancy between experiments and calculations, which predict a broader Kerr rotation spectrum. If we consider a 5.9 % larger lattice constant system, it gives a narrower bandwidth and reproduces the MO spectra well. There are no physical grounds for using the system with a larger lattice constant, but the calculated result suggests that the bandwidth also introduces a significant difference in the calculated results. We believe that the LSDA describes the Ni MO spectra moderately well because it expects an overly broad d -band and it reproduces the lower-temperature results better than the room-temperature results.

We reviewed the MO spectra of $3d$ transition metals obtained from both experiments and calculations. The maximum of Kerr rotation angle in the "visible" region appears to be less than 1 degree for Fe, Co and Ni.

2.4.4 Visible and soft X-ray regime

In Sec. 2.3, we overview the characteristics of magneto-optical effect in the soft X-ray regime. In this section, we make it clear what is different between visible and soft X-ray regime.

Firstly, element selective measurements can be performed only in the soft X-ray range. This is already explained in Sec. 2.2 and 2.3. Here we further clarify the importance of the element selectivity in investigating magnetic materials. The M - ($3p$) and L -edges ($2p$) of $3d$ transition metals and M -edges ($3d$) of rare earths fall in the

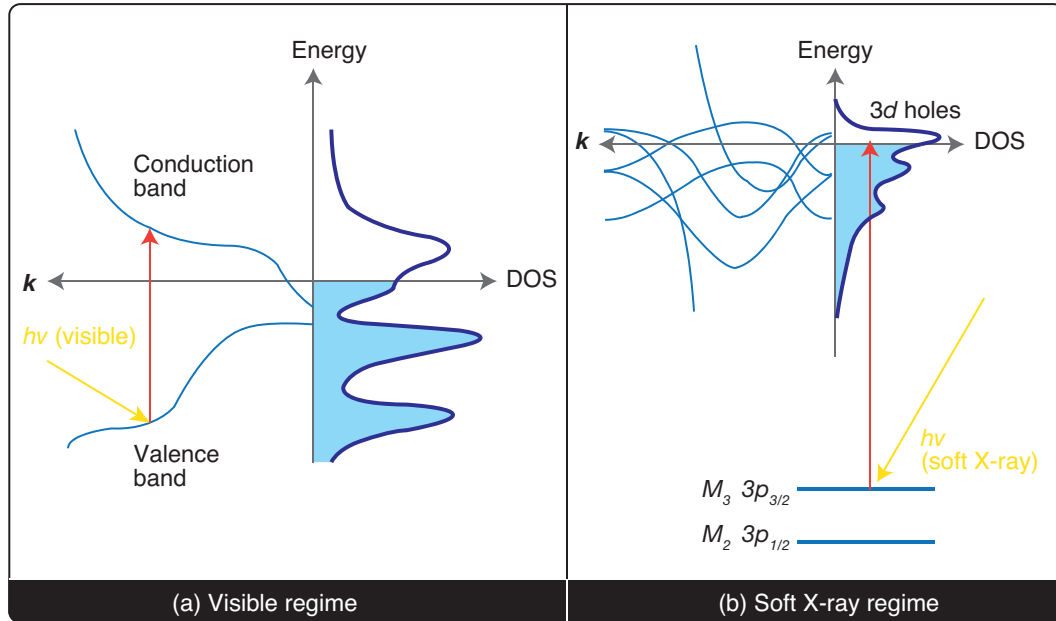


FIGURE 2.9: Transitions induced by light in the (a) visible and (b) soft X-ray range. In the visible regime, transitions occur between valence and conduction bands. On the other hand, in the soft X-ray regime, transitions is from core states to unoccupied conduction band states. In (b), the core and the conduction band is $3p$ edge and $3d$ band [86].

soft X-ray range. Through these edges, direct access to $3d$ and $4f$ states is possible for transition metals and rare earths, respectively.

Secondly, in the visible regime, reflection spectrum originate from direct interband transitions for electrons with a limited wave number. In contrast, soft X-ray magneto-optical spectrum provides k -integrated properties over valence shells. This makes it possible to relate X-ray absorption spectrum to the number of holes in unoccupied bands, spin and orbital magnetic moment as shown in Sec. 2.5.1.

Thirdly, in both visible and soft X-ray regime, the magneto-optical response is enhanced in the resonant condition, where photon energy is tuned to the target transition. However, in the soft X-ray regime, a transition occurs from a core state which has much sharper width when compared with the valence band as shown in Fig. 2.9. In the visible regime, the bandwidth of density of states related to the transition is much larger than spin-orbit splitting, which cause a certain amount of cancellation of the absorption between right- and left-circularly polarized light. In addition, the initial state in the case of soft X-ray (core states) has larger spin-orbit splitting than that in the visible regime (valence bands). These facts result in much larger magneto-optical response

due to the larger difference of helicity-dependent absorption in the soft X-ray than in the visible regime [87, 88].

2.4.5 Extension into a nonlinear regime

So far, MOKE has been explained in the linear regime, where the energy of the reflected light is same as that of the incident light. In this section, the advantage of the nonlinear regime is explained with an emphasis on magneto-optical effects in the soft x-ray region.

The light-matter interaction is mediated by dielectric polarization. It is usually proportional to the electric field of light. However, the nonlinearity of the polarization appears with increasing the power of light. This can be observed by using coherent light sources, which is lasers. Among a variety of nonlinear optical effects, SHG has been mostly used because it can detect information of spatial and time inversion symmetry. In the multiple expansion of the nonlinear polarization, the second-order polarization term, $P^{(2)}$, can be expanded by taking into account the magnetic-dipole (MD) and electric-quadrupole (EQ) response in the first order as follows [89]:

$$\frac{\partial P^{(2)}}{\partial t} = \frac{\partial \vec{P}_D^{(2)}}{\partial t} + c\nabla \times \vec{M}^{(2)} - \frac{\partial \nabla \cdot \overleftrightarrow{Q}^{(2)}}{\partial t} + \dots \quad (2.12)$$

where $\vec{P}_D^{(2)}$, $\vec{M}^{(2)}$, and $\overleftrightarrow{Q}^{(2)}$ are the induced electric-dipole (ED) polarization, magnetization and EQ polarization. It is of note that the ED polarization itself also includes MD and EQ terms [90]. The ED contribution is larger by a factor of λ/a than the MD and EQ terms [91], where λ (a) is the wavelength of light (lattice parameter). In the ED approximation, where high-order contributions such as MD and EQ components are neglected, SHG is generated only from a noncentrosymmetric system. The SHG in the ED approximation can be expressed by

$$P_i^{(2)}(2\omega) = \epsilon_0 \sum_{jkl} \chi_{jkl}^{(2)} E_k(\omega) E_l(\omega) \quad (2.13)$$

$E_i(t)$ is the electric-field component of incident light, and $\chi^{(2)}$ is a third-order susceptibility tensor. The second-order susceptibility can be expressed depending on the response to the parity operation of time inversion as follows [92]:

$$\chi^{(2)} = \chi^{(i)} + \chi^{(c)} \quad (2.14)$$

where $\chi^{(i)}$ ($\chi^{(c)}$) is a time-invariant (noninvariant) tensor and gives crystallographic (magnetic) contribution to SHG signals. For materials with ferroelectricity or (and) long-range magnetic order, the $\chi^{(i)}$ and $\chi^{(c)}$ are expressed by

$$\chi^{(i)} = \chi(0) + \alpha : \mathbf{P}_S + \mathcal{O}(\mathbf{P}_S^2) \quad (2.15)$$

$$\chi^{(c)} = \beta : \mathbf{F}_M + \gamma : \mathbf{P}_S \mathbf{F}_M + \mathcal{O}(\mathbf{P}_S^2, \mathbf{F}_M^2) \quad (2.16)$$

where \mathbf{P}_S expresses the pyroelectric polarization and this is a polar vector [91]. \mathbf{F}_M describes magnetic ordering (an axial vector in case of ferro/ferrimagnetic orders and a polar vector for an antiferromagnetic order). Those contributions have different selection rules depending on a crystal structure and a response to parity operations, so that SHG measurements allow to extract information of electric/magnetic ordering separately and their bilinear effects, magnetoelectric interaction [93], using a single-experimental configuration. Macroscopic magnetization such as ferro/ferrimagnetic order is needed for the detection with the linear magneto-optical technique. However, in the nonlinear regime, SHG is also sensitive to antiferromagnetic as well as ferro/ferrimagnetic orders. In the previous studies, the SHG probe has been applied for detecting signals from surface or interface with centrosymmetric medium and noncentrosymmetric crystals in the visible range. Nonlinear optical effects in the energy range from EUV to soft x-ray has not explored so far because there has not been intense lasers in the energy range. However, the SHG technique in the EUV \sim soft x-ray range which can excite the inner-core states is expected to detect electric and magnetic ordering from noncentrosymmetric media element selectively. In Chapter 6, the nonlinear optical effects in the soft x-ray regime is explored using the newly developed soft x-ray laser.

2.5 X-ray magnetic circular dichroism

2.5.1 Magneto-optical sum rules

X-ray magnetic circular dichroism (XMCD) has been used in the soft X-ray range, especially around the L -edge region for the $3d$ transition metals. This technique is

combined with sum rules, which formalize the relationship between the spin/orbital magnetic moments and the absorption spectrums for right- and left-circularly polarized light. XMCD occurs by the same principle as Kerr ellipticity. Both comes from magneto-dichroic effects, which are the difference of the absorption between right- and left-circularly polarized light.

XMCD can be detected by measuring helicity-dependent absorption. The signal is proportional to $\langle M \rangle$, so it probes the net magnetic moment in ferro/ferrimagnets and paramagnetic systems with element and orbital selectivity. Furthermore, it can be used for lateral magnetic imaging. The incident angle dependence of XMCD can be used to measure the anisotropy of an orbital magnetic moment.

Combining the sum rules derived by [94] for spin moment, and those by [95] for orbital moment, the spin and orbital contributions to magnetic moments can be investigated. These sum rules are summarized by Chen *et al.* in [96].

$$m_{\text{orb}} = -\frac{2q}{3r}(10 - n_{3d}) \quad (2.17)$$

$$m_{\text{spin}} = -\frac{3p - 2q}{r}(10 - n_{3d}) \left(1 + \frac{7 \langle T_z \rangle}{2 \langle S_z \rangle} \right)^{-1} \quad (2.18)$$

where p, q and r are the integral value given by

$$p = \int_{L_3} (\mu_+ - \mu_-) d\omega \quad (2.19)$$

$$q = \int_{L_3+L_2} (\mu_+ - \mu_-) d\omega \quad (2.20)$$

$$r = \int_{L_3+L_2} \frac{(\mu_+ + \mu_-)}{2} d\omega \quad (2.21)$$

m_{orb} and m_{spin} are orbital and spin magnetic moments, respectively, n_{3d} is the number of $3d$ electrons, and $\langle T_z \rangle$ is the expectation value of the magnetic dipole term. $\langle S_z \rangle$ is equal to $m_{\text{spin}}/2$. The L_2 and L_3 express the integration range, which corresponds to the L_2 and L_3 region of the spectrum, respectively. μ_+ and μ_- are absorption cross-section for right- and left-circularly polarized light.

Chapter 3

Femtosecond EUV/soft X-ray light source

In this chapter, currently operating femtosecond light sources in extreme ultraviolet (EUV) to hard X-ray region are reviewed. We especially focus on three light sources: 1) free electron laser (FEL), 2) a high harmonic generation (HHG) laser, and 3) synchrotron radiation with a laser-slicing technique. Finally we compare these light sources including conventional EUV \sim X-ray light sources.

3.1 Free electron laser

Characteristics of FEL

Free electron laser (FEL) has recently appeared in the energy range from the EUV to hard X-ray range. The FEL is regarded as a fourth generation light source in the X-ray range with respect to the third generation source, a synchrotron radiation (SR). The conventional synchrotron radiation is generated by periodic magnetic arrays called, undulator as shown in Fig. 3.1. Electron bunches which proceed between the array of magnets emit dipole radiation [97].

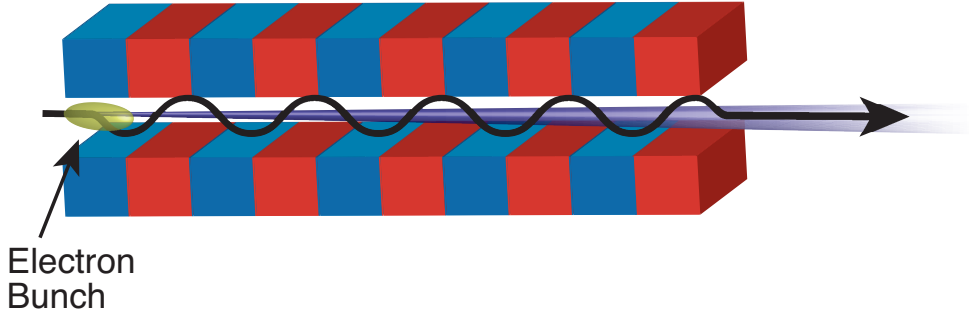


FIGURE 3.1: Undulator is an insertion device for generating synchrotron radiation. This is composed of a series of periodic magnets.

Firstly, we give the difference between X-ray laser (FEL) and the conventional visible laser. There are mainly three differences between them: 1) amplification medium, 2) Variability of energy and 3) amplification scheme.

1. Amplification medium: the reason why this light source in X-ray range is called the laser of *free* electrons is that the FEL uses free electrons for an amplification medium. These free electrons are generated from atoms in an electron gun and accelerated to the relativistic speed. On the other hand, the amplification results from the stimulated emission caused by bound electrons in the visible range.
2. Variability of energy: In the visible range, the energy emitted from the bound electrons is defined by the transition from an inverted population of the amplification medium. On the other hand, the energy of FEL is defined by the following resonant wavelength.

$$\lambda = \frac{\lambda_U}{2\gamma^2} \left(1 + \frac{K^2}{2}\right) \quad (3.1)$$

where λ , λ_U and K are the FEL wavelength, undulator period and undulator parameter. $\gamma = \sqrt{\frac{1}{1 - \frac{v^2}{c^2}}}$ and $K = \frac{eB_0\lambda_U}{2\pi m_e c}$ where v and B_0 are the electron velocity and undulator magnetic field. From this formula, it is found that the energy can be changed by controlling the electron beam energy (γ) or the gap of the undulator (this results in the change of K through the change of B_0).

3. Amplification scheme: in the visible range, coherent amplification occurs in optical cavities composed of two reflective mirrors. The cavity is filled with amplification medium. The light is amplified as a result of the interaction with the

medium by passing through the same path repeatedly. On the other hand, there are no optical mirrors, which are used for normal-reflection, for the X-ray range. Therefore, in this higher energy range, the amplification of light is achieved by a long undulator, which the light passes through once. This is why the laser in the X-ray range (FEL) is only available at a large-facility with a long accelerator and undulator.

Next, we give the difference between the third (SR) and fourth (FEL) generation light source in the X-ray range. Both light sources emit light with the wavelength defined by Eq. 3.1. However, compared with SR, FEL is literally "LASER" in the X-ray range and has characteristics of 1) full spatial coherence, 2) a extremely higher power and 3) shorter pulse duration on the subpicosecond timescale. These features result from the energy interaction between light and free electrons, which makes electron bunches align at intervals equal to light wavelength (microbunching). This makes it possible to amplify radiation from electron bunches coherently. The total intensity of emitted light become proportional to N^2 (N : the number of electrons in a bunch). On the other hand, in the incoherent amplification process for the case of SR, electrons do not have correlation each other and the total intensity is proportional to N . The pulse duration of undulator radiation is determined by the convolution between $\sigma_t = N_u \lambda / c$ and σ_{bunch} , where σ_t is the pulse length emitted by one electron, N_u is the number of undulator period, and σ_{bunch} is the length of an electron bunch. FEL is emitted from an electron bunch with much shorter duration than that in SR, which makes the FEL pulse width shorter than SR.

The FEL intensity saturates with a certain amount of undulator length. This length is called saturation length. The undulator in the FEL facility is designed to have larger length than the saturation length of FEL [98].

The coherent amplification and its saturation or gain depend on the quality of electron bunches which are injected into a series of undulator. The high quality of electron bunches mean low emittance, and high peak current. The emittance is defined by the product of electron beam size and its angle divergence.

SASE and seeded FEL

FEL is classified into two types depending on a seed light for the coherent amplification: one uses the spontaneous emission which is generated at the entrance of

the undulator and the other uses an external laser. The former regime is called self-amplified spontaneous emission (SASE) FEL [99] and the latter regime is called seeded FEL.

In the SASE regime, the spontaneous emission is regarded as noise, which means that the initial emitted radiation has its own time structure and makes the final output FEL multimode in the temporal distribution. This deteriorates the temporal coherence of SASE FEL.

Compared with SASE regime, the seeded-type FEL has several advantages in spectrum (reduced spectral linewidth, reduced fluctuation of central wavelength), time structure and arrival time by using a single-mode external laser as a seed. In the seeded regime, the output FEL is expected to be a single mode and have full temporal coherence as well as spatial coherence. There are three techniques which have been already achieved in the EUV \sim X-ray FEL facility.

- **Self seeding** In this scheme, a monochromatized FEL with the wavelength same as that of the final output FEL is used as a seed. This can be done by inserting a grating in the course of long undulator for SASE source. The difficulty for this technique is to achieve temporal overlap between the monochromatized FEL and an electron bunch. Furthermore, in this scheme there is larger intensity fluctuation than that in the following schemes. This regime is employed in LCLS in US [100].
- **High gain harmonic generation (HG HG)** In this regime, the external laser with much longer wavelength (typically 800 nm) than a target FEL wavelength in the EUV range is used. This principle was proposed in Ref. [101]. This regime is employed at FERMI in Italy [102, 103]. HG HG scheme uses two arrays of undulator called modulator and radiator. Between the modulator and radiator, there is a dispersive section formed by four dipole magnets. At the modulator section, energy modulation is formed in electron bunches with the period equal to the wavelength of the input external laser. At the dispersive section, the energy modulation is converted into density modulation of electron bunch. Finally, at the radiator section, the one of the high harmonics of the input external laser from the density-modulated electron bunch is emitted as an output (FEL). In order to convert the input laser wavelength into higher order than that achieved by the single set of modulator-radiator, another set of modulator-radiator can be used, where the output of first radiator is used again as an input for the second

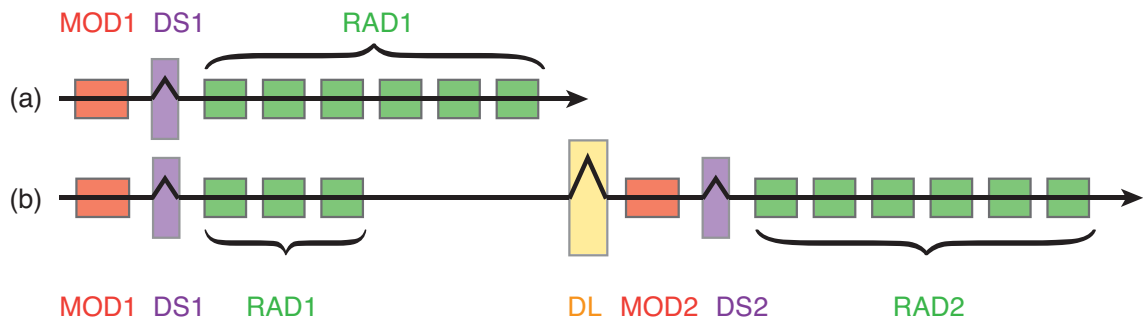


FIGURE 3.2: High gain harmonic generation scheme for generating a free electron laser. (a) In the modulator section (MOD1), energy modulation of electron bunches is formed by four dipole magnets, followed by the dispersive section (DS1), where the energy modulation is converted to density modulation of electron bunches. In the radiator section (RAD1) the density-modulated electron bunch emit one of the high harmonics of the input external laser. (b) The output of RAD1 is again injected into another set of RAD+DS+RAD for generating FEL pulses with shorter wavelength. The delay line (DL) adjusts the temporal overlap between the radiation emitted by the first stage of the radiator and an electron bunch.

modulator as shown in Fig. 3.2 [104]. This is called the "cascaded" HGHG regime.

- **High harmonic generation (HHG)** This scheme uses the light with the same wavelength as that of the target FEL as a seed laser. Coherent pulse with the duration on the femtosecond order and the energy in the EUV and soft X-ray range can be generated through the interaction between strong laser field and noble gas. This gives odd-order high harmonics of the driving fundamental laser. This high harmonics can be used as a seed for FEL. This regime was employed at SCSS in Japan [105] and FLASH in Germany [106]. Details of HHG laser is given in Sec. 3.2.

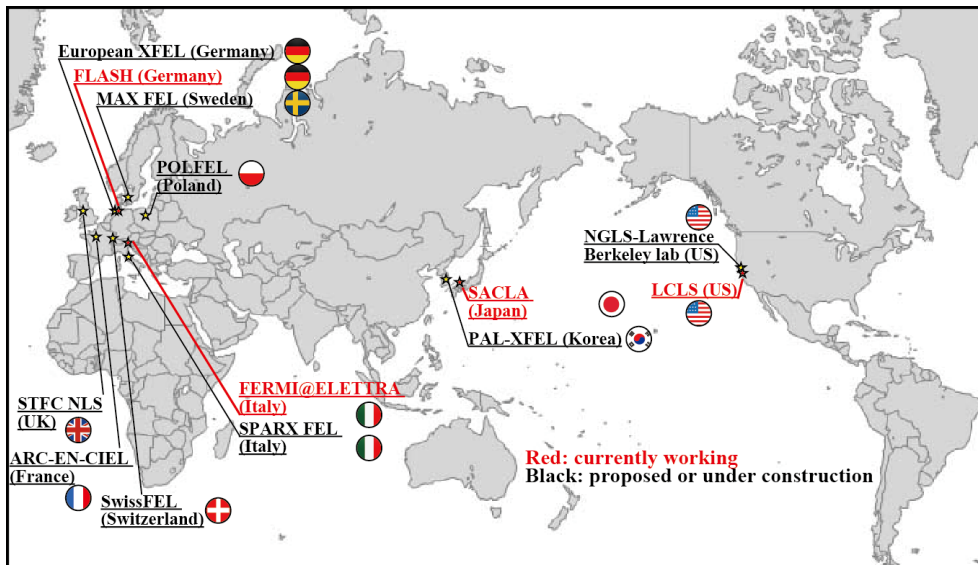
HGHG and HHG regime has an advantage in a time-resolved measurement using pump-probe technique (which is explained in Sec. 5.1.1). By using pump and probe pulse from the same light source, pump-probe measurements can be conducted in a jitter-free way.

EUV-X-ray FEL facility in the world

In Fig. 3.3, Locations of FEL facilities which are currently operating or under construction are shown in the map. We have shown FEL in the EUV \sim X-ray region. Currently four facilities are available: LCLS in USA, SACLA in Japan, FERMI in Italy, and FLASH in Germany. In 2017, European XFEL facility will start to be used by external users. In this thesis, we have used FERMI for experiments shown in Sec. 5.2 and SACLA in Sec. 5.3, and Ch. 6.

3.2 High harmonic generation laser

High harmonic generation (HHG) is coherent ultrashort laser pulse on the femtosecond order in EUV / soft X-ray range. This technique has been implemented in the laboratory-scale system. This contrasts with a FEL which is large-facility based light source. A nonlinear interaction between strong laser field and a noble gas gives rise to odd-order high harmonics of a fundamental laser [107, 108]. Currently, the HHG laser has been extensively used in the field of physics, chemistry, and biology.



XFEL Facility in the world (2017/03)

FIGURE 3.3: Locations of FEL facilities which are currently operating or under construction in the world.

The investigation of harmonic generation dates back to the work by P. A. Franken *et al* in 1961 [109]. They observed the first second harmonic generation from a non-isotropic crystalline quartz. In 1967, first third harmonic generation (THG) from gas has been reported by New *et al* [110]. After the first THG observation, higher order harmonics had been targeted and in 1987, McPherson *et al* observed 17th harmonics of excimer laser with the wavelength of 248 nm, the pulse energy of 20 mJ, and pulse duration of 350 fs by using Ne gas [111].

Three step model

Here we give the quasi-classical description for the HHG laser [112, 113]. For the accurate description, we need to consider the time-dependent Schrödinger equation, but we can extract the feature of HHG from this simple three step model.

HHG process can be broken into the following three steps.

- (i) Tunnel and ionization: strong laser field modifies the Coulomb potential of atoms in a gas, which makes electrons tunnel the Coulomb barrier to go out.
- (ii) Acceleration electrons: After the ionization, the electrons accelerate and gain a momentum in the laser electric field.
- (iii) Recombination: when the sign of laser electric field reverses, the accelerated electrons are pulled back to the parent ion. This causes recombination and emit a photon of higher energy.

Next we give several equations for describing the three step models. The total ionization rate is given as follows [114]:

$$\eta(t) = \exp \left[- \int_{-\infty}^t \omega(t') dt' \right] \quad (3.2)$$

where $\omega(t)$ is the ionization rate at time t and given by

$$\omega(t) = \omega_P |C_{n^*}|^2 \left(\frac{4\omega_P}{\omega_t} \right)^{2n^*-1} \exp\left(-\frac{4\omega_P}{3\omega_t}\right) \quad (3.3)$$

$$\omega_P = \frac{I_P}{\hbar} \quad (3.4)$$

$$\omega_t = \left(\frac{eE(t)}{2m_e I_P} \right)^{1/2} \quad (3.5)$$

$$|C_{n^*}|^2 = 2^{2n^*} [n^* \Gamma(n^* + 1) \Gamma(n^*)]^{-1} \quad (3.6)$$

$$n^* = Z \left(\frac{I_H}{I_P} \right)^{1/2} \quad (3.7)$$

I_P , I_H , $E(t)$, m_e , and Z are the ionization potential of atom in a target gas, the ionization potential for atomic hydrogen, the laser electric field, the electron mass, and the order of ionization respectively. Γ is the Gamma function.

In the second step, the ponderomotive energy (U_P), which is kinetic energy the electrons gain, is given by

$$U_P(\text{eV}) = \frac{e^2 E^2}{4m_e \omega_0^2} \quad (3.8)$$

$$= \frac{e^2 I}{2m_e \omega_0^2 \epsilon_0 c} \quad (3.9)$$

$$= 9.3 \times 10^{-20} \times I(\text{W/cm}^2) \times (\lambda(\text{nm}))^2 \quad (3.10)$$

where e , E , and ω_0 are the electron charge, the laser electric field, and angular frequency of the fundamental laser, respectively.

In the third step, energy generated by the recombination is given by

$$E_{\text{cutoff}} = \hbar\omega_{\text{max}} = I_P + 3.17U_P \quad (3.11)$$

where I_P and ω_{max} are the ionization energy and the maximum angular frequency, respectively. From this equation, the cutoff order can be extracted as:

$$q_{\text{max}} = \frac{I_P + 3.17U_P}{\hbar\omega_0} \quad (3.12)$$

where q_{max} is the cutoff harmonic order and given by $q_{\text{max}} = \omega_{\text{max}}/\omega_0$.

By increasing the U_P through the use of a longer wavelength of the driving laser, a higher laser power, or a atom with larger I_P , one can get the higher cutoff energy.

3.3 Synchrotron radiation with a laser-slicing technique

This technique, called femtoslicing, is based on the use of conventional third generation synchrotron radiation generated by bending magnet or undulator devices. The conventional SR pulse duration is on the order of 50–100 ps. The concept of femtoslicing was proposed in 1996 [115]. This technique has been achieved using bending magnet source at ALS in Berkeley, USA [116], undulator source in soft X-ray at BESSY-II in Germany [56] and in hard X-ray region at SLS in Switzerland [117]. A new slicing facility is currently under preparation at SOLEIL, in France [118].

Similar to HGHG regime in FEL presented in Sec. 3.1, femtosecond pulses from conventional SR are result of laser-induced energy modulation of electron bunches. Femtosecond laser pulse co-propagate with SR and modifies the energy distribution of electron bunch through coherent interaction at the first undulator, called modulator. In order to achieve the coherent interaction, the modulator is designed so that the λ in Eq. 3.1 matches to the wavelength of co-propagating femtosecond laser. Most of electrons do not be influenced by the femtosecond laser field. Only a small part of electrons increase or decrease its kinetic energy.

Then, the energy modulation is converted to a spatial modulation by using dipole magnets. After being spatially separated, the energy-modulated electrons at the modulator emit femtosecond pulse from the second undulator, called radiator. At BESSY II, the photon flux (per second per 0.1 % bandwidth) is on the order of 10^6 – 10^7 photons/s.

3.4 Comparison of femtosecond EUV / soft X-ray pulses

Here, we compare femtosecond EUV/ soft X-ray pulses that has been utilized in the condensed matter physics. Table 3.4 compare various light source in the energy range from EUV to hard X-ray region. We compare in terms of pulse intensity, pulse duration, energy range, repetition rate, and spatial / temporal coherence. These light sources have their unique characteristics and are complementary each other. It is not possible to cover all of the scientific research with one light source. In the design of a new experiment, it is of great importance to choose the suitable light source.

In the photon energy ranging from EUV to hard X-ray range, FEL has by far the most brilliant sources.

Table 3.1 Status of current and future ultrashort X-ray pulses

Light source	$\frac{\text{photons}}{\text{pulse} \cdot 0.1\% \text{b.w.}}$	Pulse duration	Energy range	Repetition rate	Spatial coherence	Temporal coherence
Laser-generated plasma	$10^1 - 10^5$ (a)	100 - 300 fs	< 30 keV	10 Hz - 2 kHz		
3rd generation synchrotron radiation	$10^4 - 10^6$	20 - 100 fs	0 - 100 keV	< 500 MHz	$\sim 0.1\%$	$\sim 0.1\%$
Short pulse photon source	10^8	~ 100 fs	Fixed energy 8 keV	10 Hz	$\sim 0.1\%$	$\sim 0.1\%$
Energy recovery linac	$10^4 - 10^7$	~ 100 fs	0 - 100 keV	< GHz		
High harmonic generation	$10^4 - 10^6$	0.1 - 100 fs	< 500 eV	kHz - MHz	$\sim 100\%$	$\sim 100\%$
Laser slicing	$10^1 - 10^3$	100 fs	0 - 100 keV	1 - 10 kHz	$\sim 0.1\%$	$\sim 0.1\%$
Free electron laser	$10^{11} - 10^{12}$	10 - 150 fs	$10^{-3} - 100$ keV	10 - 60 Hz	$\sim 100\%$	$< 1\%$ (SASE) $\sim 100\%$ (Seeded)

(a) it depends on X-ray optics

Chapter 4

Static M -edge polar resonant MOKE

This chapter has been published as [119].

4.1 Introduction

In the visible region, magneto-optical Kerr effect (MOKE) has been extensively utilized for probing average magnetization of target systems. The visible MOKE spectra for $3d$ transition metals were compared with calculations as a test-bed for applying itinerant theory as already seen in Sec. 2.4.3. On the other hand, in shorter wavelength range around the soft X-ray region, light interacts with core-levels of matter, such as $2p$ or $3p$ edge for the $3d$ transition metals. These core-level states are relatively localized to each elements compared to states near the Fermi level for magnetic metals. Therefore, RMOKE can detect magnetization element-selectively.

In this chapter, M -edge RMOKE on Ni thin films are investigated using synchrotron radiation. The polar geometry shown in Fig. 4.1 has been employed and the out-of-plane magnetization component has been detected. Following this, preceding studies on RMOKE will be overviewed. After this section, firstly measurement techniques for polar RMOKE in the soft X-ray region which were developed in this research are explained while comparing with that used for MOKE in the visible region. Secondly, the target system employed for the polar RMOKE measurements will be introduced together with X-ray magnetic circular dichroism (XMCD) measurements. At last, results of a polar

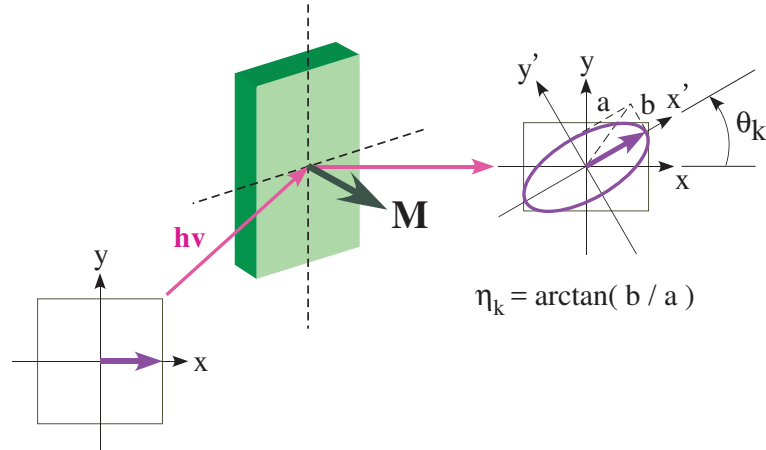


FIGURE 4.1: Illustration of the polar magneto-optical Kerr effect. Linearly polarized light is, after reflection from a magnetized material, elliptically polarized and the main polarization plane is tilted over a small angle θ_k with respect to that of the incident light. The ellipticity of the reflected light is quantified by $\eta_k = \arctan \frac{b}{a}$.

RMOKE measurement that was conducted at Japanese synchrotron facility, BL-18A in Photon Factory will be presented and are compared with calculations for evaluating the validity of the magnitude of Kerr rotation angle.

4.1.1 Preceding studies of resonant MOKE

In this section, we overview earlier experimental studies on transverse RMOKE (T-RMOKE), Faraday effect, longitudinal RMOKE (L-RMOKE). Furthermore we make comment as to theoretical considerations for polar RMOKE (P-RMOKE). In the soft X-ray region, T-RMOKE that detects only the *intensity* proceeds to RMOKE measurements that need the polarization analysis. This is because polarizers in the soft X-ray region had not been available at first and it had become available since the middle of 1990s.

We start with the preceding T-RMOKE measurements. First measurement of RMOKE was conducted on Ni *K*-edge in transverse geometry and 0.2 % as a peak-to-peak value of asymmetry has been observed [120]. This first T-RMOKE measurement was motivated from the study of an interference effect between X-ray magnetic Bragg scattering and the electric scattering in X-ray diffraction measurement [121]. This measurement was focused on *K*-edge, for which $1s \rightarrow 4p$ dipole transition takes place and magnetic signal mainly originates from *p-d* hybridization [122]. The magnitude of the asymmetry

signal which carries magnetic information is as large as that in visible region [123]. In 1990, the first L -edge T-RMOKE of Fe has been reported [124]. As expected theoretically [125], the asymmetry ratio, defined by $\frac{I^+ - I^-}{I^+ + I^-}$ where I^+ (I^-) is the intensity measured under applying external field (anti)parallel to the cross product of the wave vector of incident and reflected light, reaches $\sim 20\%$ as a peak-to-peak value due to the effect, so-called resonant exchange scattering, in which strong electric multipole transitions from the core levels to unoccupied states cause large resonant enhancement. Combining with calculations using resonant scattering amplitude [125], it was shown that the total width of an excited state and the magnitude of exchange splittings could be extracted. After this measurement several T-RMOKE measurements were reported in [126–129] for Co M -edge, in [128–130] for Co L -edge, in [128, 131–133] for Fe M -edge, in [128, 134–137] Fe L -edge, in [128, 133, 138] for Ni M -edge, in [128, 133] for Ni L -edge, in [139] for Pt L -edge and in [140] for Mn L -edge. It was also noted that for RMOKE in soft X-ray region, the reflected light has contribution from substrate if the target system is a nm-order magnetic thin film and its thickness is smaller than the penetration depth. Furthermore, in [130] magneto-crystalline anisotropy energy (MAE) was measured for ultrathin Co film using L -edge T-RMOKE and revealed its capability that this technique can be applied to ultrathin magnetic systems and investigation for MAE. T-MOKE signal basically originates from pure-charge and pure-magnetic signal. This is because the resonant atomic scattering factor, which gives the X-ray scattering amplitudes, expands with the charge and magnetic scattering term. However, when incident angle is tuned to Brewster angle, components of charge-scattering is suppressed and one can get pure-magnetic signal in the geometry [132, 135, 141]. T-RMOKE is also measured using High Harmonic Generation (HHG) laser as well as synchrotron radiation [15, 39].

Next, we move onto the Faraday measurements. In 1990, the first K -edge Faraday measurements on Co, in which polarization state of a transmitted light is analyzed, has been reported [142] and compared well with calculation [143]. The first RMOKE measurement in the soft X-ray region, in which polarization analysis was indispensable, was reported in [144]. In the Fe L -edge resonant MO measurements in Faraday configuration 6.0×10^4 deg/mm of rotation were observed and it was larger than that in visible region, 3.5×10^4 deg/mm [145], and much greater than that observed for K -edge [142], although this measurement was conducted under applying magnetic field less than saturation field. After this work, Fe, Co and Ni L -edge [146–150] and Pt L -edge [151] Faraday measurements have been reported. After a series of L -edge measurements for $3d$ transition metals, M -edge Faraday measurements were conducted on Fe,

Co, and Ni [152–155], *N*-edge on Pt and *M*-edge on Cu [154]. It was suggested that the magnitude of rotation angle observed for *M*-edge was as large as that for *L*-edge region. This implies that exchange splitting of $3p$ bands as well as spin-orbit splitting of $3p$ also plays an important role for defining MO effect [155].

Next we overview the preceding L-RMOKE studies. In 1996, the first L-RMOKE that needs polarization analysis have been reported in [156]. The Kerr rotation angle was measured at a fixed energy on Fe and Cr in Fe/Cr multilayer separately. The earlier study showed the element selectivity of L-RMOKE by measuring hysteresis loops for each element [157]. In the study, the Kerr rotation angle was $\sim 9.8^\circ$, which is two orders of magnitude larger than that in visible region, and it is also suggested that RMOKE in soft X-ray region can be conducted under a fixed incident angle with varying penetration depth by tuning the photon energy *below* the edge due to its large anomalous dispersion effects. *L*-edge L-RMOKE measuring both rotation angles and ellipticities covering whole energy range of $L_{2,3}$ edges on Fe, Co and Ni has firstly been observed by Mertins *et al.* [158, 159]. Mertins suggested that in L-RMOKE spectra there are nonmagnetic contributions; (1) interference effect between reflection from top layer and from the interface with substrate and (2) the optical constants of capping layer. Furthermore he demonstrated relationships between (1) T-RMOKE signals and Kerr rotations in the longitudinal geometry, and (2) ellipticities in the longitudinal geometry and XMCD in reflection mode. These relations are theoretically expected only under grazing incident angle condition. In [137, 160–162], the efficiency of depth profile measurements using Fe, Co and Ni *L*-edge L-RMOKE has been demonstrated by selecting appropriate incident angle and energy. *M*-edge L-RMOKE measurements on Co and Ni were demonstrated in [129, 152].

At last part of this section, we focus on preceding theoretical studies on RMOKE. The macroscopic formalism using a dielectric tensor for MOKE in visible region [145] can also be applied to that in soft X-ray region. Furthermore in [150], it was shown that this formalism using dielectric tensor provides equivalent descriptions with theory using resonant scattering factor, which gives microscopic viewpoint, within the framework of dipole approximation. For describing electronic structure, spin-polarized relativistic band theory has moderately succeeded in describing MO spectra in the visible region. In early studies, this first-principle theoretical scheme was incorporated to resonant magnetic X-ray scattering calculation [163] for calculation of *K*, *L*-edge Faraday spectra of Fe, Co and Ni [148, 164–167] and *L*-edge T-RMOKE spectra on Ni [164]. These preceding theoretical studies on RMOKE predicted giant MO response under resonant condition compared to that in visible region. Different from *K*-edge,

calculation for L -edge spectra is more complicate because the degree of localization of final states, d -states, varies and spin-orbit coupling and exchange interaction of the initial $2p$ states have to be taken into account. Therefore K -edge MO spectra are better reproduced than in the case of L -edge MO spectra. It was shown that the Kohn-Sham single-particle spectrum was used as an approximation for many-body quasiparticle excitation spectrum in LSDA scheme and that in experiments with energy resolution $E/\Delta E \sim 2500$ for L -edge region, Coulomb correlation effects and multiplet transitions were not required for calculation of Faraday / MOKE in the soft X-ray region and XMCD spectra [148].

RMOKE in polar geometry has not been investigated so far in spite of its importance in application. An earlier study predicts a much larger Kerr rotation angle in Ni $M_{2,3}$ -edge under polar geometry than that in the visible region [88]. In this theoretical study, the expected value for polar RMOKE was of the order of a degree, which was 10 times larger than that observed in the visible range. Basically there is no physical difference of RMOKE signal between a polar and a longitudinal geometry. However, in the case of polar geometry, it is expected that the larger Kerr angle can be obtained if the incident light hits on the sample normally. Furthermore, MOKE in polar geometry prefers a small incident angle (measured from the sample normal) which needs a complicated setup in a synchrotron facility and this scheme has been avoided in practical measurements. This static polar RMOKE measurements are indispensable step for extending into the time-resolved regime.

4.2 Development of a resonant MOKE measurement system

4.2.1 Measurement regime in soft X-ray region

The visible MOKE has typically been measured utilizing the polarization-plane modulation method as shown in Fig. 4.2. The rotation of the polarization plane caused by the sample-originated Kerr effect is compensated by a Faraday cell, which is positioned between a polarizer and an analyzer. In the field of magneto-optical experiments, the polarizer that is located after the sample is usually called the "analyzer". To measure the Kerr rotation angle with a better angle resolution, an AC current for modulation is combined with the DC current and the detector signal is entered into a lock-in amplifier; the lock-in amplifier output is then used as feedback to the current for the Faraday

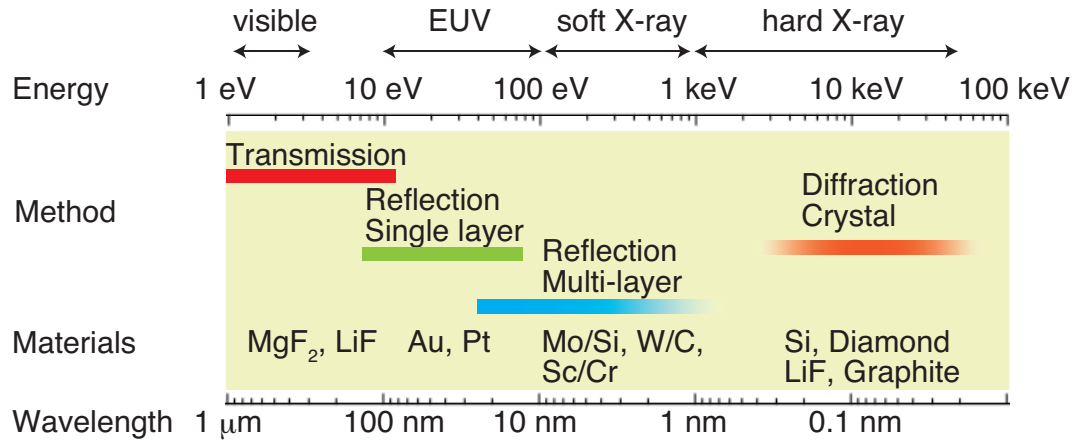


FIGURE 4.3: Methods for polarization analysis with respect to the photon energy from visible light to hard X-rays. Typical materials that are used as polarizers are shown for each energy region. This figure has been taken from [8] (Publication list No. 6)

regard to the surface) roughly defines a specific energy region with which multilayer mirrors can reflect. The components of the multilayer mirrors are materials with large differences in n and low k values. In the soft X-ray region, material pair is chosen as follows: one material that has a higher absorption edge than a target energy is selected, and the other material with low n and k in the energy range is then chosen. Brewster angle, which is defined by the incident angle at which p -reflected light is suppressed, can be employed in order to use the multilayer mirror as a polarizer. In the L -edge range, the refractive index n is close to 1, which makes the Brewster angle almost 45° . In comparison with the L -edge range, in the M -edge range, n deviates from 1, so that the Brewster angle is not close to 45° . In this M -edge range, a typical multilayer mirrors, Mo/Si, has the polarizance of the order of 10–100 under 45° incident angle, whereas in the L -edge region, multilayer mirrors such as W/B₄C and W/C show the polarizance around 1000–100000 with the same geometry. Here, the polarizance is defined by the ratio between the s - and p -reflectivity R_s/R_p . Figure 4.3 presents a collection of polarizers with respect to the photon energy from visible light to hard X-rays [170]. It is able to determine a polarization axis of reflected light in order to measure Kerr angles even with the order of the polarizance in the EUV range.

Calculated reflectivity spectrum of multilayer mirror both for p - and s -polarized light are compared for 45 degrees incidence angle in Fig. 4.4. This was calculated for Mo/Si with the periodic length of a material pair 15.6 nm (Mo:Si = 0.4:0.6), the number of repetition 10, and the roughness of the surface 0.5 nm on Si substrate. Furthermore,

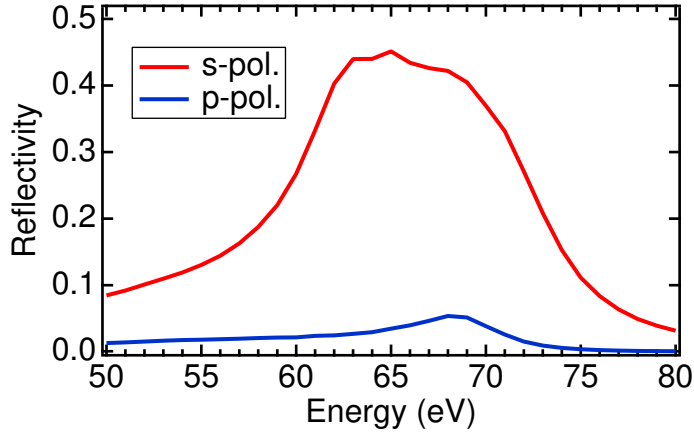


FIGURE 4.4: Reflectivity spectrum of multilayer mirror of Mo/Si for *s*-polarization (red) and *p*-polarization (blue). Mo(0.4)/Si(0.6), period length = 15.6 nm, number of layer is 10. Optical parameters are taken from Ref. [59, 171].

reflectivity of *s*-polarized light for three incident angle with respect to the multilayer surface normal are compared for the same multilayer parameters in Fig. 4.5.

In this chapter, we targeted on Ni *M* absorption edge for polar RMOKE measurements. We selected the multilayer parameters so that the reflectivity shows its peaks around Ni *M*-edge, ~ 66 eV, under 45 degrees incident angle for *s*-polarized light while having the largest polarizance. The multilayer mirror with these parameters employed in Fig. 4.4 was used for the experiment presented in the next section. These reflectivity calculations in Fig. 4.4 and 4.5 were conducted by using optical parameters taken from Ref. [59, 171]. The polarizance around Ni *M* edge with 45° incident angle was ~ 10 .

Figure 4.6 shows the measurement system using rotating analyzer ellipsometry (RAE) that is developed in this study. This technique is originally used in the visible MOKE regime using transmission-type polarizer. This method uses the multilayer mirror described above and is experimentally able to determine both the Kerr rotation angle θ_k and the Kerr ellipticity η_k .

In RMOKE measurements using this technique, the intensity of reflected light from the analyzer is measured at the detector with respect to χ , as defined in Fig. 4.6. The incident light incident on the specimen and the reflected beam then goes to the ellipsometry unit, which is utilized to extract the Kerr angles. After the reflection from the sample, the light passes through two pinholes. These pinholes are used to ensure accurate optical alignment. The light then impinges on a multilayer mirror with an incident angle roughly close to the Brewster angle. The intensity of reflected light

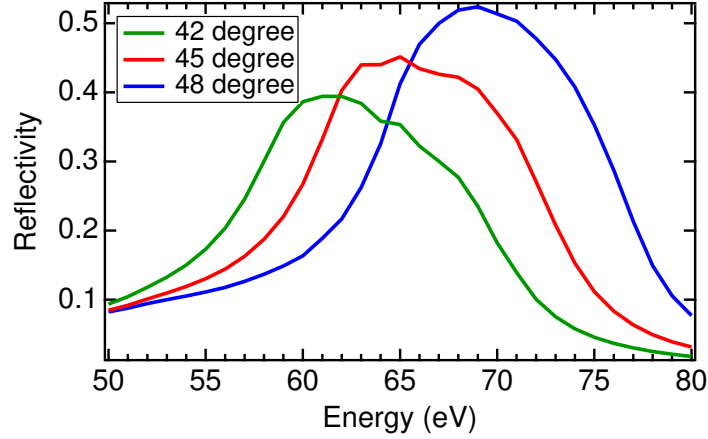


FIGURE 4.5: Reflectivity spectrum of multilayer of Mo/Si for s -polarization under incident angle 42 degrees (green), 45 degrees (red) and 48 degrees (blue). The parameter for multilayer mirror is same as that in Fig. 4.4. Optical parameters are taken from Ref. [59, 171].

from the multilayer mirror is finally measured by using a detector, microchannel plate (MCP). Current detection mode is used in the MCP detector. In order to extract the Kerr rotation angle, the unit that is shown by dashed rectangular lines in Fig. 4.6 is rotated with regard to the light axis by utilizing a rotary flange. The curve obtained by rotating the RAE unit depends on both the azimuthal angle for the polarization principal axis θ_K and the ellipticity angle η_K . It is of note that the lock-in amplification that is employed in the MOKE measurement in the visible range shown in Fig. 4.2 is not always necessary in the RMOKE measurement scheme.

Here, the intensity that is measured by using the RAE technique is given in the framework of a Mueller formalism [172, 173]. The Stokes vector is used for expressing the polarization states. The Stokes vector has four elements: S_0 (the sum of the vertical and horizontal components of the polarization (= total intensity)), S_1 (the difference between the vertical and horizontal components), S_2 (the difference between the $\pi/4$ and $-\pi/4$ components), and S_3 (the difference between the right-handed and left-handed components). It is expressed as follows:

$$S = \begin{bmatrix} S_0 \\ S_1 \\ S_2 \\ S_3 \end{bmatrix} \quad (4.1)$$

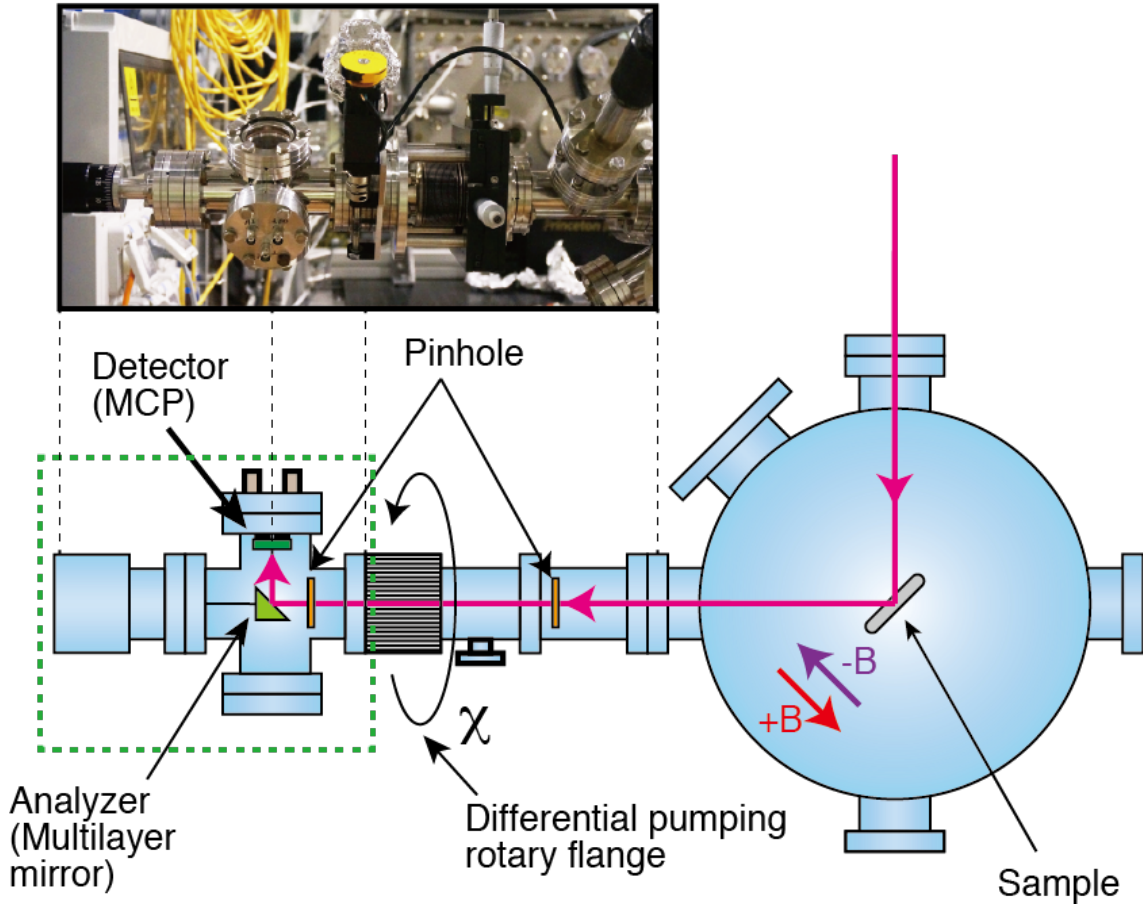


FIGURE 4.6: Measurement scheme that uses a rotating analyzer ellipsometry (RAE) for the resonant MOKE in the polar geometry is shown. The RAE unit is shown in the inset photograph. The parts enclosed by the dashed rectangular line is rotated together. This figure has been taken from [8] (Publication list No. 6)

The degree of polarization, V , is given by

$$V = \frac{\sqrt{S_1^2 + S_2^2 + S_3^2}}{S_0} \quad (4.2)$$

It is useful to define the normalized Stokes parameter that is divided by S_0 because in most real cases the absolute intensity is not more important than the polarization state. Then, the normalized Stokes parameters can be represented as follows.

$$S_0 = 1 \quad (4.3)$$

$$S_1 = V \cos 2\eta_K \cos 2\theta_K \quad (4.4)$$

$$S_2 = V \cos 2\eta_K \sin 2\theta_K \quad (4.5)$$

$$S_3 = V \sin 2\eta_K \quad (4.6)$$

In the Mueller scheme, Mueller matrix is employed for expressing the optical components. The Stokes vector $S'(\chi)$ of the reflected light from analyzer and reaching the detector can be expressed as a function of χ by using A_R (analyzer), and $R(\chi)$ (coordinate rotation). It is given by using Mueller matrices as:

$$S'(\chi) = R(\chi) \cdot A_R \cdot R(\chi) \cdot S \quad (4.7)$$

where S is the Stokes vector for the reflected light from a target sample.

The detected light intensity $I(\chi)$ at the detector can be derived from Eq. (4.7):

$$I(\chi) = S'_0(\chi) \frac{r_p^2}{2} \{S_0(\alpha^2 + 1) + S_1(\alpha^2 - 1)\cos 2\chi + S_2(\alpha^2 - 1)\sin 2\chi\} \quad (4.8)$$

where α is the amplitude ratio of reflectance for s - and p -polarized components, r_s/r_p .

The intensity can be rewritten by using the Eq. 4.6 as follows.

$$I(\chi) = \frac{r_p^2}{2} [2V(\alpha^2 - 1) \cos 2\eta_K \cdot \cos^2(\theta_K - \chi) + \alpha^2 + 1 - V(\alpha^2 - 1) \cos 2\eta_K] \quad (4.9)$$

θ_K appears in the phase-shift in $I(\chi)$. When the light is perfectly polarized, the degree of polarization, V , is equal to 1. The cosine square function depends on χ with Malus law [174, 175]. The $I(\chi)$ can simply be given by a cosine function with θ_K and η_K , if we assume that $V=1$.

$$I(\chi) = C_1(\eta_K) \cos 2(\chi - \theta_K) + C_2(\eta_K) \quad (4.10)$$

where η_K is determined by both the values of C_1 and C_2 . Thus, this RAE technique can determine the Kerr rotation angle.

In Fig. 4.7, one of the experimental results using SR are given as an example for the RMOKE measurement. These results were obtained from Ni thin film at the photon energy of 69 eV in a polar geometry. The vertical axis represents the intensity measured by MCP as shown in Fig. 4.6. This RAE technique can determine the Kerr rotation angle θ_k . For instance, the Kerr rotation angle can be extracted from the phase difference in curves that are measured under applying +B and -B fields, which corresponds to $2\theta_k$. It is noteworthy that the ellipticity depends on V in the RAE technique. When the light is not fully polarized and there is an unpolarized components, $C_1(\eta_K)$ in Eq. (4.10) then decreases. There is no intensity variations during the rotation of the RAE unit when the light is completely circular polarization or unpolarization. V depends on the the optical components that are used in the SR beamline and photon energy. In order to extract the ellipticity from the RAE measurement, the polarizance of the multilayer mirror should also be taken into account. In the remainder of this thesis, we concentrate solely on θ_K . θ_K does not depend on V . Therefore we assume $V = 1$.

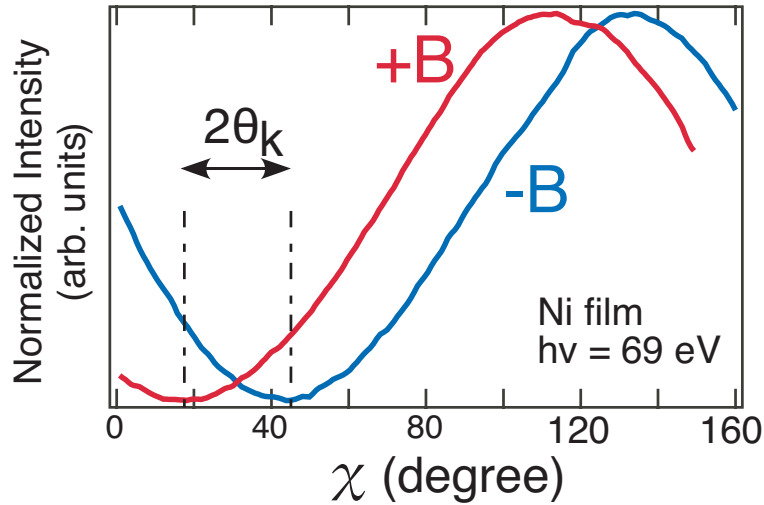


FIGURE 4.7: Typical results of the intensity variation with rotation angle, χ , taken at $h\nu = 69\text{eV}$ for Ni thin film. The Kerr rotation angle, θ_k , can be determined from $2\theta_k = |\theta(+B) - \theta(-B)|$. This figure has been taken from [119] (Publication list No. 8)

From next section, the results of the first polar RMOKE measurements on Ni thin films are presented.

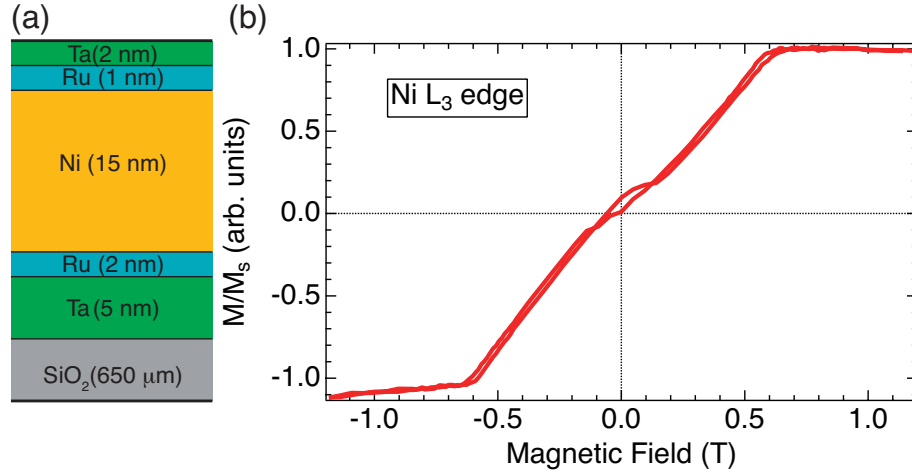


FIGURE 4.8: (a) 15-nm-thick Ni film structure. (b) Out-of-plane magnetization hysteresis loop normalized to saturation magnetization measured by XMCD at Ni L_3 edge. This has been measured by the TEY mode at room temperature.

4.3 Experiment

4.3.1 Sample Structure

Figure 4.8(a) presents the structure of a target thin film. In order to demonstrate the RMOKE, the Ni film, which is a typical ferromagnetic material, is selected. DC magnetron sputtering with 1 Å/s was utilized for fabricating a (111)-oriented Ni film. The film structure is Ta (2 nm)/Ru (1 nm)/Ni (15 nm)/Ru (2 nm)/Ta (5 nm) on thermally oxidized silicon wafers. The Ar sputtering pressure was 1 mTorr and the substrate temperature was maintained at room temperature. The Ta (2 nm) capping layer are deposited in order to protect the Ni layer from oxidation and the Ta (5 nm) underlayer help the films adhere to substrates. Reactions between the Ta and Ni layers are prevented by inserting the Ru layers. A magnetization state is canted with respect to the surface normal by applying an external field perpendicular to the film surface, which a finite M_z is induced. Out-of-plane magnetization loop measured by XMCD, which is described in the next section, at $h\nu = 853$ eV is shown in Fig. 4.8(b). The saturation field is ~ 0.6 T for the Ni thin film used in this measurements.

4.4 Results and Discussions

4.4.1 Spin and Orbital moment

Magnetic properties of the target Ni thin film were characterized by X-ray absorption spectroscopy (XAS) and XMCD. These measurements were conducted at the beamline with twin helical undulator, BL25SU, in SPring-8 [176, 177]. The total-electron-yield mode was employed for both measurements at room temperature under application of magnetic field, 0.47 T, generated by an electromagnetic coil. The helicity-switching mode was used for the measurement of XMCD spectra at 1 Hz. In Fig. 4.9(a), Ni $L_{2,3}$ XAS spectra and its integrated intensity are presented. The $2p_{3/2}$ ($h\nu \sim 853$ eV) and $2p_{1/2}$ ($h\nu \sim 870$ eV) core excitations cause the two L_3 and L_2 peaks in the spectra, respectively. Before integration, the two-step background (fine solid line) was subtracted [96]. Similarly, the Ni $L_{2,3}$ ($2p \rightarrow 3d$) XMCD spectrum and its integrated value are shown in Fig. 4.9(b). From this spectrum, the spin ($m_{\text{spin}}^{\text{eff}}$) and orbital (m_{orb}) magnetic moment can be extracted by applying the magneto-optical sum rule [96] (Eq. (2.17) and Eq. (2.18)). This analysis gives the magnetic parameters, $m_{\text{spin}}^{\text{eff}} = 0.53 \mu_B$ and $m_{\text{orb}} = 0.067/\text{atom}$ at $B = 0.47$ T ($m_{\text{spin}} = 0.77 \mu_B/$ and $m_{\text{orb}} = 0.12/\text{atom}$ at the saturated magnetization), from the obtained spectra for the Ni film in Fig. 4.8(a). These values are basically consistent with previous experiments for bulk fcc Ni [178, 179]. The spectra obtained from this measurement were used in comparing the experimental polar RMOKE results with the theoretical calculation in the next section.

4.4.2 Ni *M*-edge polar resonant MOKE

In order to verify the calculation results [88], we conducted *M*-edge RMOKE measurements at the beamline, BL-18A, in KEK-PF. The Kerr rotation angle, θ_k , had been experimentally determined with RAE technique shown in Fig. 4.6 and 4.7. External magnetic fields, $B = \pm 0.47$ T, from permanent magnets (Nd) are applied perpendicular to sample surface. The field was inverted directly by changing the direction of the magnet.

In Fig. 4.10, the experimental results given by red circles show the θ_k (~ 10 degree) near Ni $M_{2,3}$ absorption edge. In order to verify the observed Kerr signals, we performed theoretical simulation. The calculation results are shown by the blue line in Fig. 4.10.

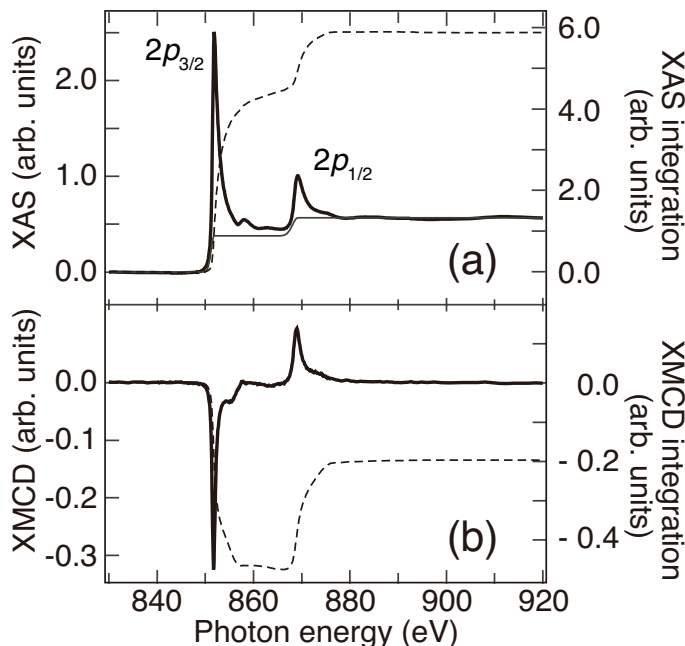


FIGURE 4.9: (a) X-ray absorption (XAS) spectrum (solid line) and (b) X-ray magnetic circular dichroism (XMCD) spectrum of the 15-nm Ni thin film shown in 4.8(a) under application of a magnetic field of 0.47 T perpendicular to the sample surface. The integration value in (a) and (b) is presented with the dotted line. This figure has been taken from [119] (Publication list No. 8)

The theoretical simulation was conducted using a cluster model calculation based on a localized Anderson impurity approach taking into account a configuration interaction (CI). This calculation incorporates both intra-atomic multiplet interactions and the many-body charge transfer. The details are described in Appendix C. This calculation regime is extensively applied for data analysis of experiments under core-level resonant condition, where photon energy is set to a specific absorption edge. For example, this model is applied to photoemission spectroscopy, resonant inelastic X-ray scattering (RIXS), resonant X-ray diffraction, XAS, and XMCD of d and f electron systems. In the core-level spectroscopy for d and f electron systems, the charge transfer effects and multiplet coupling have an essential influence on the spectrum structure.

The reflection coefficients for a bulk Ni crystal were calculated for the reflection configuration in Fig. 4.1 in the current simulation. Here, interference effects [159] originated from the multiple reflection due to the finite thickness of the Ni layer were neglected for simplicity. Low photon energy, $h\nu \sim 70$ eV and a large incident angle, $\theta_i = 45^\circ$ are taken in our experimental conditions. When compared with the standard RMOKE in the L -edge range, which employs high photon energy ($h\nu = 700 \sim 900$ eV)

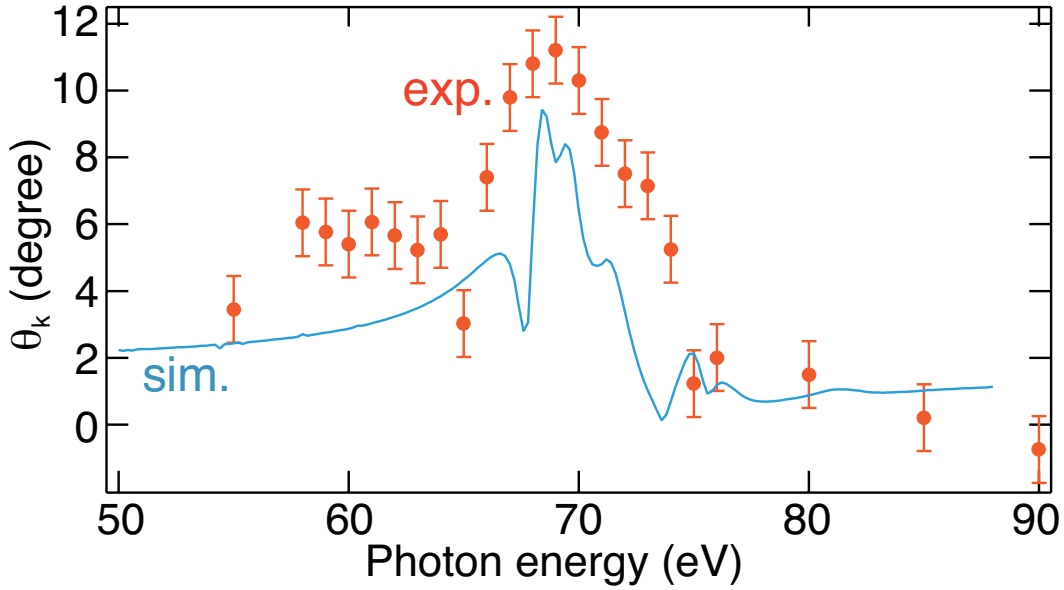


FIGURE 4.10: Kerr rotation angles, θ_k , spectrum of the Ni thin film are compared between values determined experimentally with EUV synchrotron radiation (exp.) and those from the calculation with the cluster model (sim.). Measurement was conducted at room temperature under a magnetic field of $B=0.47$ T. This figure has been taken from [119] (Publication list No. 8)

and small grazing incident angle ($\theta_i = 1 \sim 10^\circ$), the interference has a less influence on RMOKE in the *M*-edge range. The model parameters are independently extracted from other core-level spectroscopies. The simulation reproduced large Kerr rotation angles near the absorption edge observed in the experiments. Furthermore, the whole features of experimental results agree with the calculations. θ_k of the experimental values show larger than that of calculations. It is confirmed that the variation of the simulation results was marginal within angular errors in the experimental setup even if the model parameters were changed from the values extracted from the core-level spectroscopies which were independently conducted. Hence, the difference between experiment and calculation results is rather fundamental. We inferred that the deviation, particularly in the pre-edge range, may come from interference effect because of the film structure in the nanometer scale which was comparable with the wavelength used in the measurements. This interference effect has not been considered in the current bulk model.

4.5 Conclusion

Polar RMOKE measurements system has been developed and in this system, the Kerr rotation angle can be measured using rotating-analyzer ellipsometry (RAE) technique. In the RAE regime, reflection-type multilayer mirror has been applied as a polarizer by using it at Brewster angle. Using the developed measurement scheme, a demonstration of polar RMOKE using soft X-ray synchrotron radiation was performed. A giant Kerr angle ($> 10^\circ$) was observed at the M -edge of the Ni thin film at room temperature. These experimental results were consistent with simulation based on resonant scattering theory. These Kerr rotation angles in RMOKE are 50 times larger than angles experimentally determined for a Ni crystal in the visible range [68, 180] as shown in Fig. 2.8. We believe that the technique, developed in the current study, can be applied for other transition metal films. Because the RMOKE measurement has the element specificity and takes a photon-in and photon-out scheme in the setup, it can probe magnetization of a specific element in complicated magnetic compounds with applying external electromagnetic fields [15].

Here, we would like to summarize the characteristics of RMOKE compared to MOKE in visible region that has been known in this chapter.

- Element-specificity. Light interacts with core-levels which was localized to a certain element in RMOKE measurement while MOKE using visible light relates to transition between valence and conduction bands which are delocalized and itinerant.
- Simple experimental setup. For the conventional MOKE measurement in the visible range, an optical component for modulating the state of the polarization with high frequency and lock-in techniques have always been necessary to get a sizable signal-to-noise ratio. However, in the RMOKE setup, such optical components and techniques are not needed due to the large Kerr rotation angle.
- Giant magneto-optical (MO) response. Compared to MO effect in visible region, the Kerr rotation angle was more than 50 times larger in the case of Ni thin films. This enhancement relates to the sharper bandwidth of core states than that of the valence bands already pointed out in Sec. 2.4.4 [88].

The RMOKE measurement system developed in this chapter can be extended to time-resolved measurement using a free electron laser. This gives opportunities for

tracing magnetization dynamics element-selectively. It is of note that in our system, polarization analysis unit that is shown using a image in Fig. 4.6 is portable size so that it can be brought to a free electron laser facility even if it is located in foreign countries.

Chapter 5

Extension of resonant MOKE technique to sub-picosecond time resolution

5.1 Introduction

5.1.1 Pump-Probe Scheme

For tracing specific dynamics of a certain system or a motion in the experiment, one needs to capture its properties periodically in a stroboscopic way during the dynamics. The repeated measurements allow ones to make a movie and to reveal the nature of the system in detail. Pump-probe technique that is utilized in experiments is based on the same idea. In this technique, two pulses are used for investigating the evolution of the system. First pulse (pump pulse) gives a perturbation to a target system and second pulse (probe pulse), with a certain amount of delay time (Δt) with respect to the first pulse regarding arrival time to the system, probes its system influenced by the first pulse. Measurements using these two-pulses set are repeated many times until one gets enough signal-to-noise ratio and then by varying the delay time between these two pulses, one is able to obtain the time-evolution of the system. For clear interpretation of the obtained data, it is crucial that the interested system gets back to the equilibrium state between two pump pulses. This enables to excite the system reproducibly, or from the same initial state every time. The time resolution is defined by either 1) larger pulse width of pump or probe, 2) temporal jitter between pump and probe pulses or 3) data

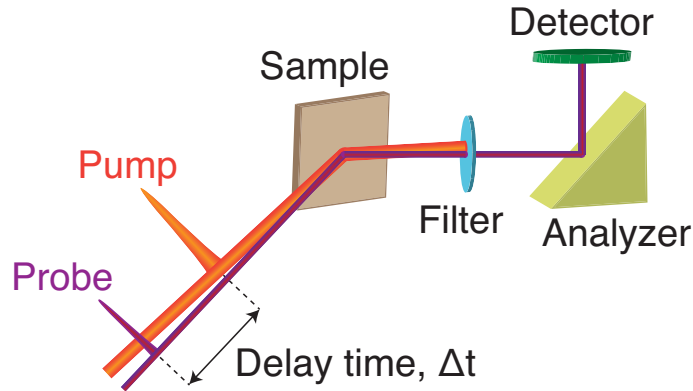


FIGURE 5.1: Schematic diagram of pump-probe technique for time-resolved resonant magneto-optical Kerr effect measurements. A filter is used in order to prevent pump lights from entering into a detector.

acquisition system. In the obtained time-dependent signal, noise partly comes from irreproducible contributions.

In order to trace the system in sub-picosecond timescales, ultrashort laser pulses in the femtoseconds regime should be employed. Electronic population in nonequilibrium states can be produced after intense laser irradiation to the target system. By using probe pulse that arrives with a certain amount of delay to the pump pulse, one can obtain laser-induced dynamics in sub-picoseconds timescale.

In this pump-probe scheme, the diameter of a pump pulse should be larger than that of probe pulse on the sample. In ultrafast spin dynamics study, so called femtomagnetism, typical fluence for inducing demagnetization, magnetization reversal or spin coherent precession on metallic samples is of the order of a few mJ/cm^2 . Given that a diameter of pump pulse is about $100\mu\text{m}$, a pulse energy corresponds to about $0.1\mu\text{J}$. In terms of the fluence of probe pulses it should be weak enough not to change the system properties.

The features of the light sources is given by the following parameters: a jitter between pump and probe light, pulse widths (fs), a spot size (μm), incident angles, fluences ($\text{J}/\text{cm}^2/\text{pulse}$), a photon energy (eV), an effect of higher order of light, polarizations, repetition rates (Hz), fluctuations for energy and incident intensity. It is also important to select a suitable detector that has a appropriate sensitivity in terms of time resolution, energy and photon flux.

In Fig. 5.1, schematic pump-probe technique for time-resolved resonant magneto-optical Kerr effect (TR-RMOKE) measurements are depicted.

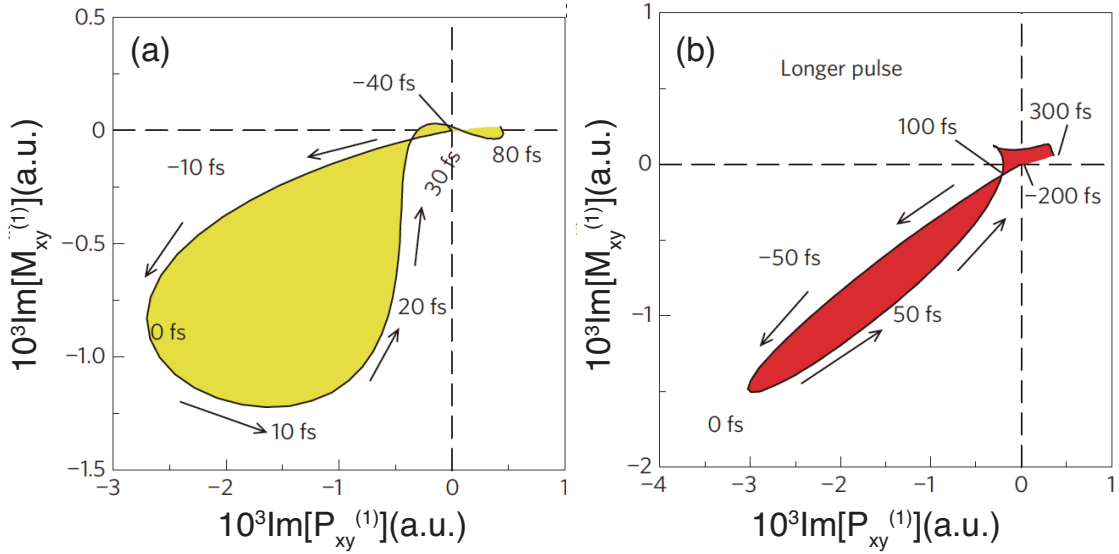


FIGURE 5.2: Phase diagram of polarization versus magnetization for pulse duration of 12 fs(a), and 64 fs (b). The vertical (longitudinal) axis expresses magnetic (optical) response. These were calculated assuming photon energy was 2.0 eV. Taken from [14].

5.1.2 Magnetic and optical response in TR-MOKE measurements

In this chapter, we have measured time-dependent Kerr rotation angle by *polarization analysis* for tracking spin dynamics. We have assumed that the detected transient Kerr rotation angles are proportional to the magnetic vector at each delay time. We briefly describe the relationship between the time-dependent Kerr signals and transient magnetization in this section.

Firstly, the discrepancy of the time evolution for the Kerr rotation and the ellipticity was experimentally observed within the hundred femtoseconds by Koopmans *et al.* [181]. This was explained theoretically by the state-blocking effect, or dichroic bleaching effect [182], which is caused by the transient saturation of a certain optical transition by a pump and a probe pulse if they have the same energy and polarization. This effect can be avoided by using different energies for pump and probe pulse. In [9], it was pointed out that coherent interaction between femtosecond laser pulses and the magnetization of target material. This should be taken into account in timescales of a few femtoseconds, which is characterized by dephasing time. In this timescale, optical and magnetic response behaves differently and the magneto-optic results should be carefully dealt with. In [14], it was shown that the pulse duration was also related to the relation between the optical and magnetic response in sub-picoseconds timescale. The

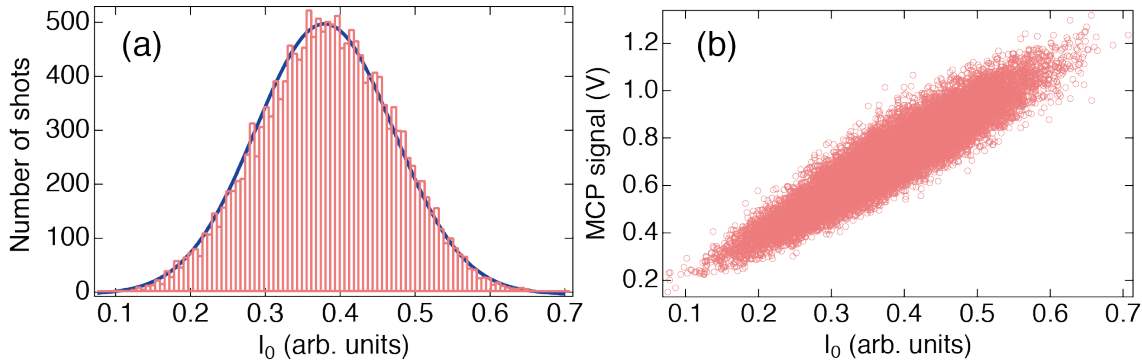


FIGURE 5.3: (a) Histograms of FEL incident intensity. The solid line represents the gaussian fit. (b) MCP signals detected by using RAE unit as a function of FEL intensity (I_0)

relation between optical and magnetic response was explored for different pulsewidth in Fig. 5.2. It was revealed that in experiments using light source with duration longer than the charge dephasing time, which is in the case of (b), the optical and magnetic response coincided each other. In this case, time-resolved magneto-optical measurements reflect the magnetization dynamics. In this thesis, because we have used laser pulses with duration larger than the typical dephasing time for metals, which is a few femtoseconds, we assume that the time-resolved magneto-optic data express the transient magnetic response of target systems.

5.1.3 Shot-by-shot measurement system

FEL has an inherent intensity fluctuation, so that shot-by-shot measurement scheme should be developed. In Fig. 5.3(a), the intensity fluctuation obtained at SACLA is shown. From the fitting by gaussian function, the fluctuation of FEL incident intensity was $\sim 30\%$. In 5.3(b), MCP signals measured by using RAE unit shown in Fig. 4.6 are plotted with respect to the FEL incident intensity. This shows the linearity of the MCP detector. By normalizing MCP signal by FEL incident intensity in a shot-by-shot way, the intrinsic signals originated from samples can be collected.

5.2 First time-resolved resonant MOKE measurement with a FEL

This section has been published as [8, 183].

5.2.1 Introduction

FERMI@ELETTRA in Italy is the only facility, at which we are capable of utilizing seeded-type free electron laser (FEL) in soft X-ray region, among currently operating FELs in the world. We have developed time-resolved resonant MOKE measurement system using FEL and connected the systems in tandem at a downstream side of beamline's measurement chamber at DiProI beamline in FERMI shown in Fig. 5.4.

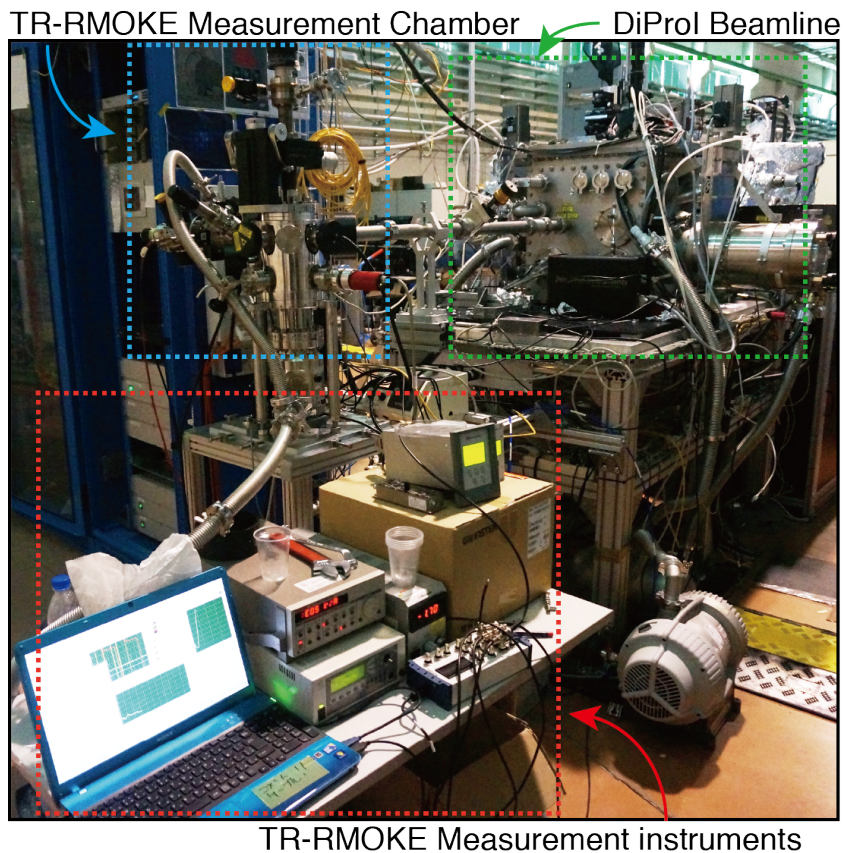


FIGURE 5.4: Image of measurement chambers and instruments for TR-RMOKE and DiProI beamline in FERMI@ELETTRA.

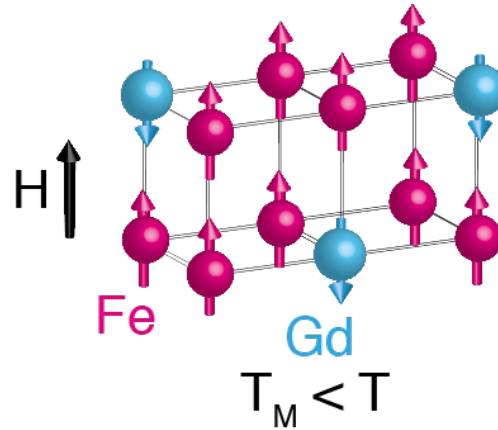


FIGURE 5.5: Schematic diagram of ferrimagnetic structure of GdFeCo. The direction of magnetic moment of Fe (Gd) sublattice is (anti-)parallel to that of the external field. This is the case when the sample temperature is above compensation temperature (T_M). About T_M , see Fig. 5.7.

In order to demonstrate that TR-RMOKE technique can be employed for tracing light-induced spin dynamics in sub-picoseconds timescale, we focus on magnetization reversal process of GdFeCo. GdFeCo is a ferrimagnetic metallic alloy, which has rare-earth (RE) and transition metal (TM) sublattices. These two sublattices couple anti-ferromagnetically as shown in Fig. 5.5.

In Fig. 5.6, various magnetization reversal schemes are shown and they range from nanoseconds down to sub-picoseconds timescale. Top figure shows magnetization reversal using external magnetic field. This field induces a precession with damping. The magnetization reversal with this scheme of GdFeCo was firstly observed by time-resolved visible MOKE measurements [184]. In this preceding study, temperature- and field-induced magnetization reversal has been reported in the timescale longer than 100 ps. In the middle figure, magnetic field pulse with duration that is equal to half of a precession period is used for magnetization reversal through the half precession. Magnetization reversal using this scheme takes place in picoseconds timescale [185]. In order to induce magnetization reversals faster than above two schemes, ultrashort laser pulses should be used. Interaction between light and matter has attracted attention in the magnetization reversal process after Kimel *et al.* [187] reported that the state of magnetization can be selectively influenced by the helicity of excitation laser pulse. The magnetization reversal of GdFeCo was shown to be helicity-dependent by using ultrashort laser pulse with circular polarization that acts as an effective magnetic field (so-called opto-magnetic effect)[188]. Only later, magnetization reversal without applying external a magnetic field, all-optical switching (AOS), has been reported by

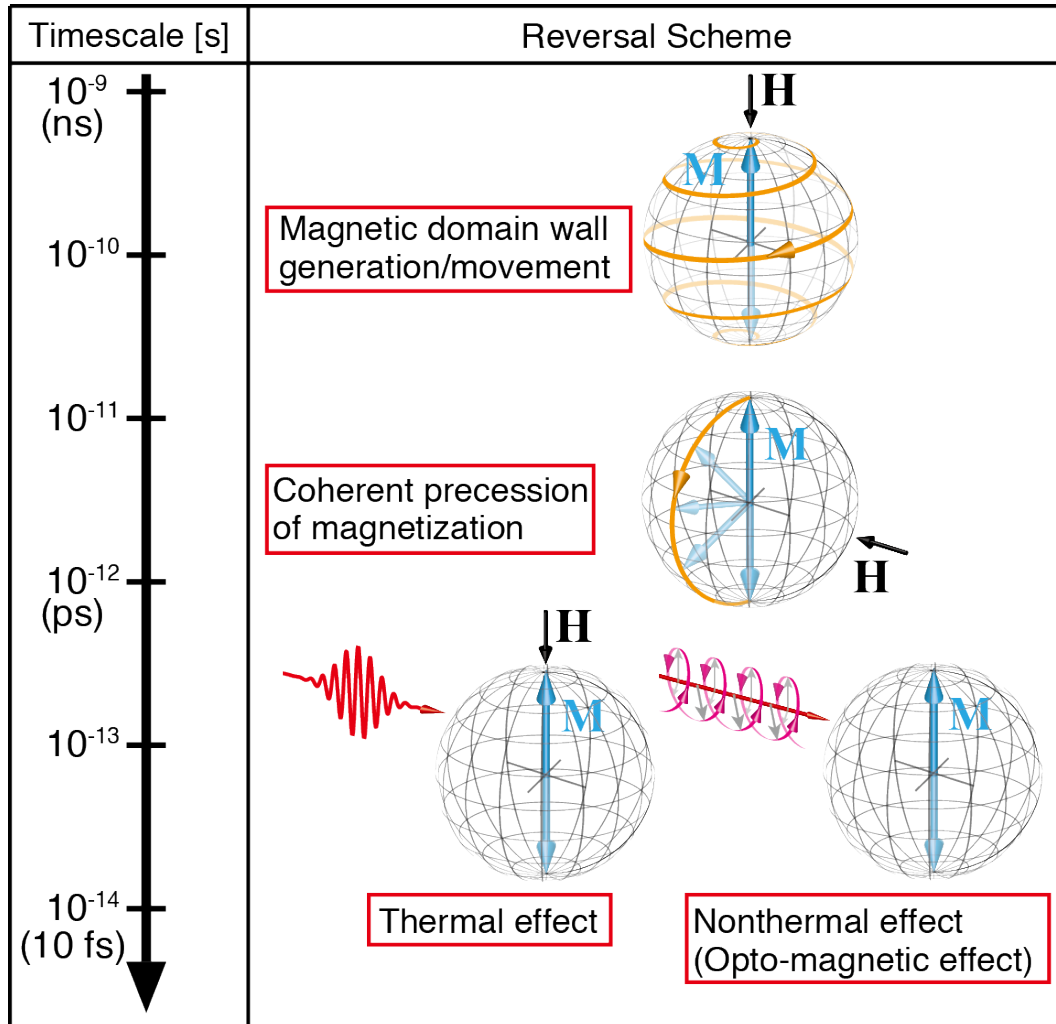


FIGURE 5.6: Magnetization reversal schemes are shown with respect to time axis ranging from nanosecond to sub-picoseconds timescale. Top two figures are made by referring to [186].

employing a excitation pulse with circular polarization [189, 190] or even linear polarization [20, 42, 191]. Recently, AOS which depends on helicity of an excitation pulse has been demonstrated on ferromagnetic alloy [192]. In order to describe the magnetization reversal experimentally observed in ferrimagnetic materials from a microscopic point of view, a number of models have been suggested: inverse Faraday effect (IFE) [193], the combination of ultrafast heating effect with IFE [194], superdiffusive current [195], transient ferromagnetic-like coupling between two non-equivalent sublattices because of the nonequilibrium nature [42], and exchange of angular momentum between two sublattices [196, 197]. The dynamical process of magnetization switching is also still

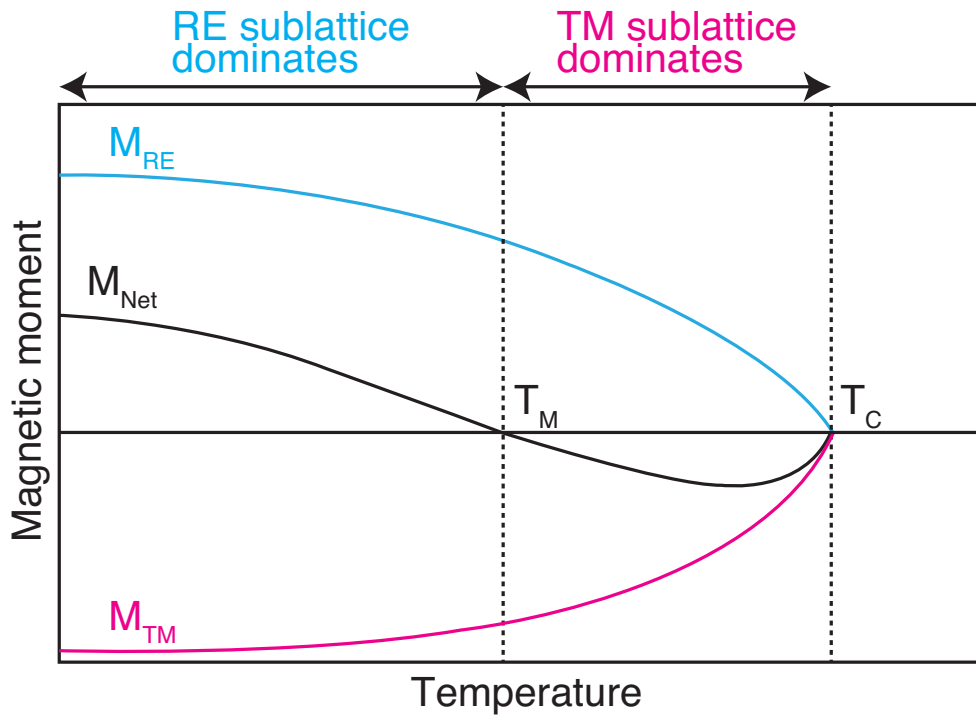


FIGURE 5.7: A schematic showing temperature dependence of magnetization of transition-metal (M_{TM}) and rare-earth (M_{RE}) sublattice. Net magnetization (M_{NET}) is also shown. At compensation temperature (T_M), $M_{NET}=0$.

debatable, whether it involves spin precession or only longitudinal modulus of magnetization [198]. Therefore the microscopic mechanism of magnetization reversal reported on ferrimagnetic alloys has still been controversial. In this section, magnetization reversal of GdFeCo is focused on using linearly polarized light by using ultrashort laser pulse with linear polarization. This magnetization switching involves with thermal effect, which excludes the non-thermal contribution, for example IFE, where an intense circularly polarized light acts as an effective magnetic field pulse that can induce magnetization switching.

Temperature dependence of each sublattice in GdFeCo differs each other, so that at a certain temperature, the total (net) magnetic moment (M_{NET}) becomes zero. This temperature is called compensation temperature (T_M). The illustration of temperature dependence of magnetization for each sublattice (M_{RE} for rare-earth and M_{TM} for transition metal) is shown in Fig. 5.7. Curie temperature (T_C) and T_M can be adjusted by varying the composition ratio.

5.2.2 Experiment

In Fig. 5.8 (a) and (b), the earlier studies are compared regarding the magnetization reversal of transition-metal sublattice, caused by the linearly polarized light, under each experimental configuration [42, 191]. In the experimental condition of Fig. 5.8(a), the external field was applied in the direction antiparallel to that of the initial Fe magnetization, which corresponds to the state before pumping, in the time-resolved X-ray magnetic circular dichroism (XMCD) experiment employing a laser-slicing light source at a synchrotron radiation facility [42]. In this measurement, the sample temperature was initially set below the T_M . It was reported that the Fe magnetization reverses to the direction of the external magnetic field in the hundreds of femtoseconds. During the magnetization reversal process, the temporal ferromagnetic state in the Gd-Fe coupling was observed. Experimental condition taken in other earlier study using a time-resolved XMCD-PEEM experiment is shown in Fig. 5.8(b) [191]. Here, in contrast to the case in Fig. 5.8(a), the Fe magnetization switching was observed when temperature before pumping was set to both above and below T_M . Furthermore, this magnetization reversal was measured without applying external magnetic field. It is still not known under which condition this magnetization reversal occurs regarding the sample temperature and the existence of the external magnetic field. Therefore it is necessary to investigate the influence of those parameters on the ultrafast magnetization switching. In the present study, we adopted the third experimental condition, shown in Fig. 5.8(c). In the present study, the sample temperature before pumping was set at room temperature. This is above the T_M (~ 250 K) of our target GdFeCo. The external field was applied in the initial Fe magnetization direction. The femtosecond time-resolved measurement of the resonant MOKE (RMOKE) was carried out utilizing the seeded-type FEL as a probe pulse. In the current study, the photon energy was tuned to the Fe M -absorption edge, to achieve element-selectivity. The magnetization reversal of Fe magnetic moment was traced in the subpicoseconds timescale.

5.2.3 Results and discussion

Static Property

Figure 5.9(a) represents the thin-film sample structure, where the ferrimagnetic alloy has the composition $\text{Gd}_{21}(\text{Fe}_{90}\text{Co}_{10})_{79}$. The $T_M \sim 250$ K of the $\text{Gd}_{21}(\text{Fe}_{90}\text{Co}_{10})_{79}$ is below room temperature. In the composition of our target alloy, the TM-sublattice magnetic moment is larger than the RE one at room temperature and the direction of the external magnetic field is parallel to that of the Fe magnetic moment. A multilayer

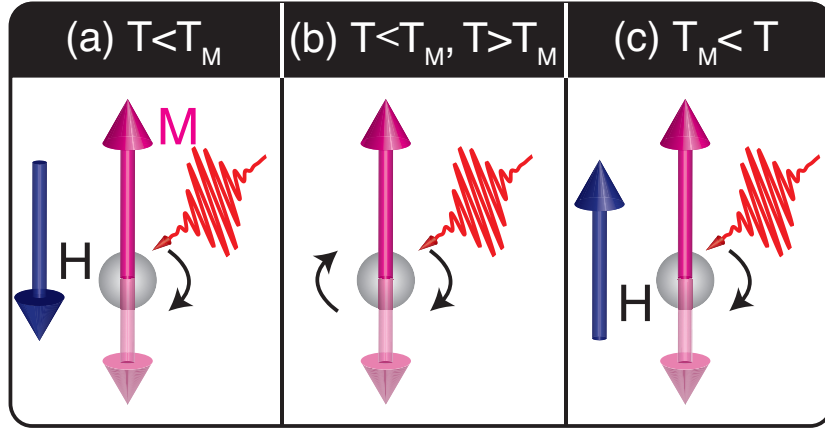


FIGURE 5.8: Comparison of experimental conditions in ultrafast magnetization reversal among (a) Ref. [42], (b) Ref. [191] and (c) this study; a direction of Fe magnetization before irradiation is shown by up-pointing red arrow. In (a) and (c), an external magnetic field is represented by the down-pointing blue arrow. The way the magnetization reverses is indicated by the black curved arrow caused by the pumping laser with linear polarization. The comparison with the T_M before pumping is shown at the lower part in each diagram.

film of Ta (2 nm)/GdFeCo (20 nm)/Ta (10 nm) was grown by means of RF magnetron sputtering on thermally oxidized silicon wafers. The top layer, Ta (2 nm) capping layer, keeps the GdFeCo oxidization and the Ta (10 nm) underlayer helps the GdFeCo layer adhere to the Si substrate. X-ray absorption spectroscopy (XAS) spectra for the target GdFeCo sample is shown in Fig. 5.9(b). The experimental results detected in the total electron yield (TEY) mode are presented with the red circles and the peak at the photon energy of 33 eV, 42 eV and 66 eV are assigned to the Ta $5p_{3/2}$, $5p_{1/2}$ and Co $3p$ absorption, respectively. This XAS measurement was carried out at the bending-magnet beamline, BL-5B, in UVSOR (Japan). The calculated XAS spectra for Fe $3p$ are shown with the blue line, which is based on a cluster model taking into account configuration interaction [119]. The simulation shows good agreement with the experiment. Fig. 5.9(c) compares experimentally measured and calculated Fe M -edge RMOKE spectra. The RMOKE measurements in the polar geometry were performed, where the external field, (± 0.47 T), was applied perpendicular to the sample face. The measurement geometry of time-resolved RMOKE (TR-RMOKE) with FEL was exactly the same as that of static RMOKE. The Kerr rotation angles were measured by employing the rotating analyzer ellipsometry (RAE) technique, as illustrated in the inset of the Fig. 5.10. The detailed description of the measurement system are given in Sec. 4.2.1. The RMOKE simulation (see Appendix. C and [119]) was made using the magnetic parameters extracted from the Fe $2p$ XMCD spectra

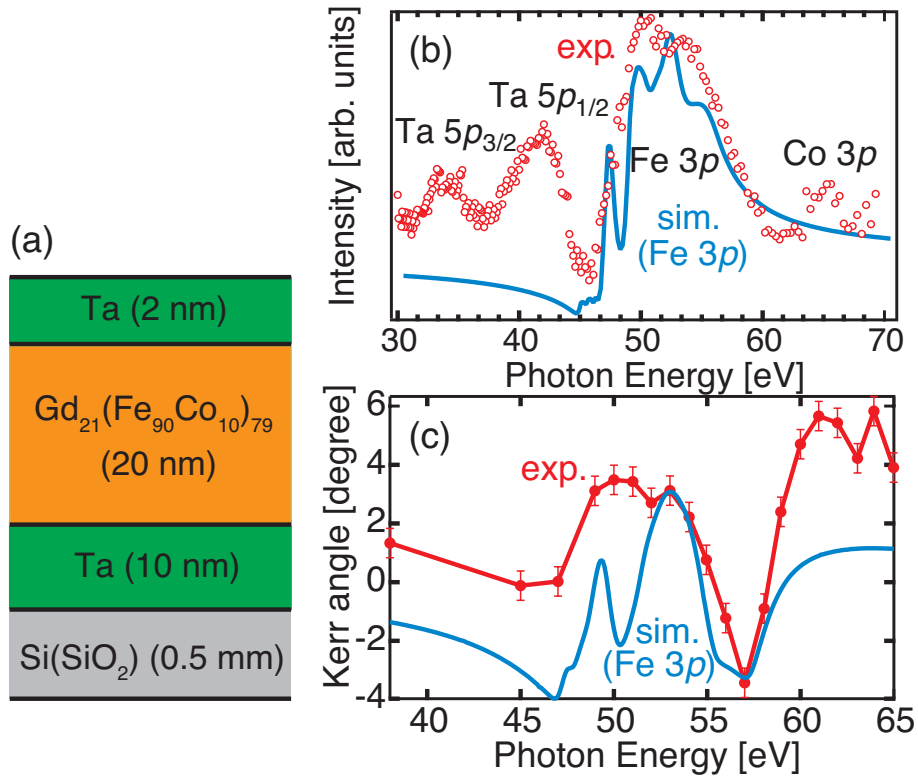


FIGURE 5.9: (a) A schematic diagram of a 20-nm-thick amorphous GdFeCo film. (b) XAS spectra of the GdFeCo film calculated (sim.) and measured experimentally (exp.) using TEY mode. (c) the photon energy dependence of the Kerr rotation angle, θ_K . Measurement was performed at room temperature under a magnetic field of $B = \pm 0.47$ T. In calculation, the resonant effect of Fe 3p edge was taken into account and the effect of Ta 5p- and Co 3p-edges were not been considered. This figure has been taken from [183] (Publication list No. 7)

measured at the undulator beamline, BL-16A, in Photon Factory (Japan). By applying the magneto-optical sum-rules, the orbital (m_{orb}) and spin ($m_{\text{spin}}^{\text{eff}}$) magnetic moment for Fe in GdFeCo were evaluated to be $m_{\text{orb}} = 0.096 \mu_B/\text{atom}$ and $m_{\text{spin}}^{\text{eff}} = 2.10 \mu_B/\text{atom}$, respectively. In Fig. 5.9(c), the resonant effect of M -edge Co and the optical interference effect due to the nanometer-scale film structure [119, 159] (not considered in the calculation) cause the difference between the experiment and simulation observed near 60 eV and 40 eV, respectively. From these static measurements, 53 eV is selected as the most suitable photon energy for tracking the transient Fe magnetization response in the GdFeCo alloy during the magnetization reversal in the present time-resolved measurement.

A schematic of the TR-RMOKE measurement system is presented in Fig. 5.10 using

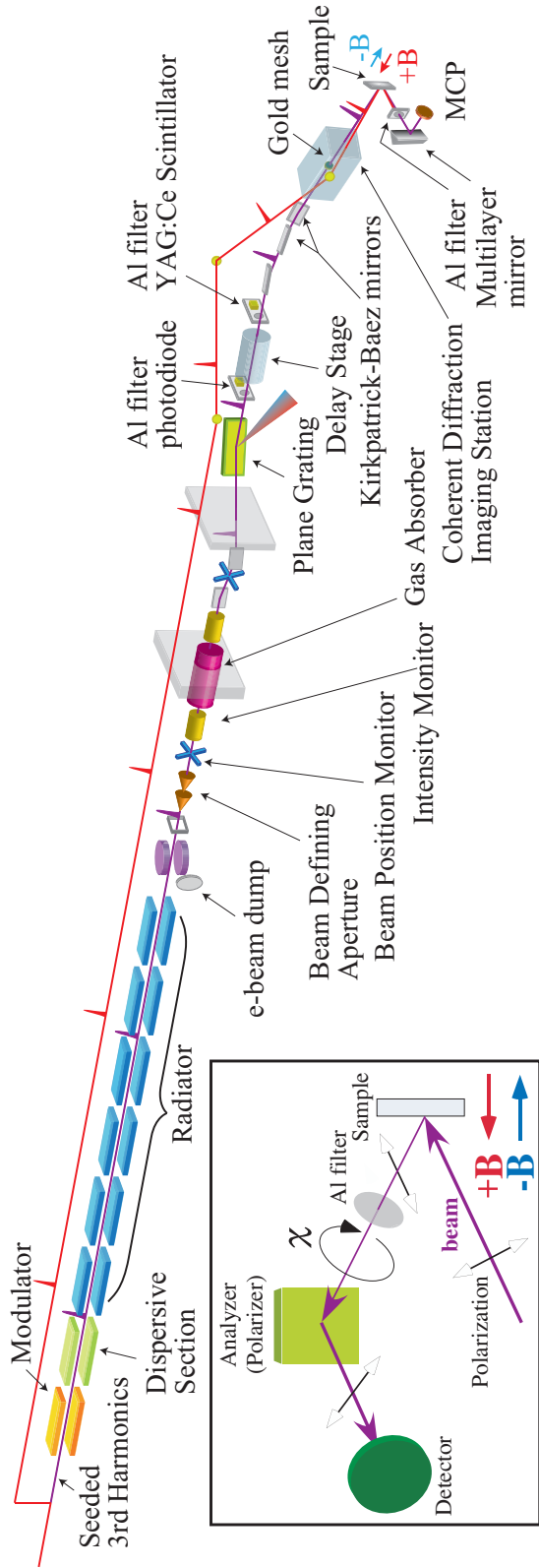


FIGURE 5.10: A schematic of the measurement scheme of time-resolved RMOKE using the seeded-type FEL at DiProI beamline in FERMI@ELETTTRA is shown with a femtoseconds-pump pulses which is also used as a seed for generating FEL. Measurement system developed in this study was connected in series to the end of the Coherent Diffraction Imaging station. (Inset) RAE part is presented: an analyzer, Mo/Si multilayer and a detector. This figure has been taken from [183] (Publication list No. 7)

the infrared (IR) lasers and seeded FEL as pump and probe pulses, respectively. The measurements at room temperature were performed using the seeded FEL at the DiProI beamline [199] in FERMI@Elettra (Italy). The FEL-1 that the photon energy from 12.4 to 62 eV (60-20 nm) can be available was employed with an electron beam energy of 1.2 GeV [102, 103]. Different from the self-amplified spontaneous emission (SASE) scheme which is commonly used, a HGHG seeding scheme that FERMI takes has much higher longitudinal coherence and spectral purity. In FERMI@ELETTRA, both linearly and circularly polarized light can be generated [64]. Furthermore, because seeded FEL is generated from the IR laser which is also used as a pump pulse, this scheme can be utilized for practically jitter-free time resolved experiments [200].

In the present measurements, we used 80-100 fs FEL pulses as a probe setting to 52.5 eV (23.6 nm), generated by an IR laser with a wavelength of 780 nm and repetition rate of 10 Hz which is also used as a pump. The IR laser and FEL had spot-size of 530 μm and 420 μm at the sample position, respectively. Time resolved measurement has been performed with the time resolution of 150 fs, which is limited by the pump-pulse duration. The pump and probe fluence were set to 14 mJ/cm^2 and 3 mJ/cm^2 , respectively. A YAG crystal is used for ensuring the spatial overlap between pump and probe pulses. Two steps were taken for determining the temporal overlapping of these pulses: 1) a copper antenna connected through a high bandwidth coax cable [200] was used with a fast oscilloscope to achieve the overlap within *pm* 50 ps, and 2) time-dependent reflectivity measurement on Si_3N_4 was performed in the FEL-pump/IR-laser-probe scheme for determining time zero within 250 fs [200, 201].

Concerning the experimental configuration, the IR laser (pump, linear-horizontally polarization) and the FEL (probe, linear-vertically polarization) were coaxially introduced to the target sample. The FEL reflected in the *s*-polarization geometry. The incident and reflected angle of the FEL were set at 45° . The reflected FEL moved to the RAE unit, as described in Sec. 4.2. An Al filter was used for attenuating the reflected IR laser. The Kerr rotation angle at each delay time between pump and probe pulses were measured in the same manner as those used in the static RMOKE measurement. The fluctuation of FEL intensity was monitored using a gas-cell in a shot-by-shot way.

Ultrafast Magnetization reversal of Fe sublattices

In Fig. 5.11, energy diagram related TR-RMOKE measurements of GdFeCo is schematically shown. In pump-probe measurements, pump pulses are used for excitation of Fe

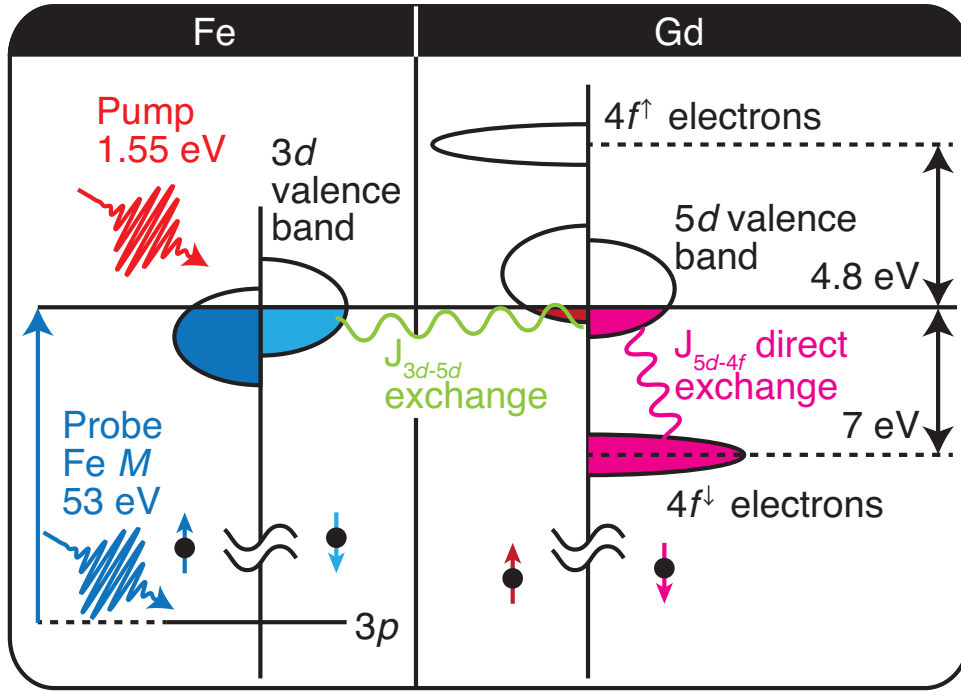


FIGURE 5.11: Electronic structure related in TR-RMOKE measurements of GdFeCo. 4f state positions of Gd are referred by [62].

3d spins into mobile sp states [195]. In this pump excitation, Gd 4f spins do not participate in the process.

The results of time-resolved RMOKE measurements are shown in Fig. 5.12(a). Each panel shows the results of RAE at each delay time indicated in the top. The normalized intensity shown in the vertical axis means that the intensity measured at MCP was normalized with respect to the incident FEL intensity. The reflected intensity from the analyzer is detected by MCP with respect to χ , as shown in the inset of Fig. 5.10. At each delay time, RAEs were performed under applying external field, ± 0.47 T, perpendicular to the sample surface, which correspond to the two curves (blue and red) in Fig. 5.12(a). Cosine fitting results are shown with the solid lines. The angle zero in each panel corresponds to the extinction state without external field. In the time-resolved measurement, the phase difference between the two curves gives the Kerr rotation angle at each delay time. The Kerr rotation angle measured at the delay time of -100 fs was 3.1 degree, which reproduced the value obtained from the static RMOKE measurement (3.2° at the photon energy of 53 eV) as shown in Fig. 5.9. The polar configuration which was taken in the current TR-RMOKE measurement reflects the

out-of-plane component of Fe magnetic moment in GdFeCo. Figure 5.12(b) schematically depicts the transient magnetization behavior with regard to the applied magnetic field, which is deduced from the temporal variation of the Kerr rotation angles. The arrow length at each delay time shown in the Fig. 5.12(b) is proportional to the magnitude of the Kerr rotation angle. The sign of the Kerr rotation angle changed at the delay time of 200 fs, which indicates the switching of Fe magnetic moment. The sample was in room temperature before the irradiation of the pump pulse, which was higher than T_M . In the earlier studies [42], the magnetization reversal was observed for the sample set below the T_M before pumping. These facts show that the laser-induced magnetization reversal occurs regardless of the temperature with respect to the T_M before the pumping. The contribution from the nonthermal effect involving IFE that was employed in the earlier studies [188] is excluded in this study because the linearly polarized light was employed. Therefore, thermal effect from the pump pulse and the exchange of angular momentum between two sublattices are thought to have a contribution in this magnetization reversal. Considering the repetition rate (10 Hz) of pump-probe sets, the magnetic moment of the Fe sublattice returned to the initial state 100 ms after the irradiation of pump pulse. The path for angular momentum transfer is mainly closed between the sub-lattices of Gd and Fe [196]. It is of note that the coherent coupling between photons and spins should also be considered regarding the exchange of angular momentum in the magnetization switching process. In Fig. 5.13, time-dependent results obtained through this research using TR-RMOKE with FEL are compared with preceding study using TR-XMCD with laser slicing [42]. The timescale of magnetization reversal of TM sublattice is the same between the two measurements. Our TR-RMOKE measurements reveal that this scheme can be used for tracking laser-induced transient magnetization in sub-picoseconds timescale. This is the first demonstration using resonant MOKE for tracing magnetization dynamics element selectively. The importance here is that the measurement has been performed for detecting transient out-of-plane magnetization in the reflection regime, which has a potential to apply to a wide variety of materials ranging from ultrathin magnetic films to thick bulk systems with out-of-plane magnetization as well as magnetic compounds with in-plane magnetization. This is the clear contrast when compared with the conventional TR-XMCD technique which needs to make samples thin enough for transmission measurements for detecting perpendicular magnetization.

From a methodological point of view, visible MOKE is widely used for tracking averaged magnetization dynamics of the target magnetic materials [68]. In the section, we present the RMOKE feature that allows for tracking transient magnetization in the

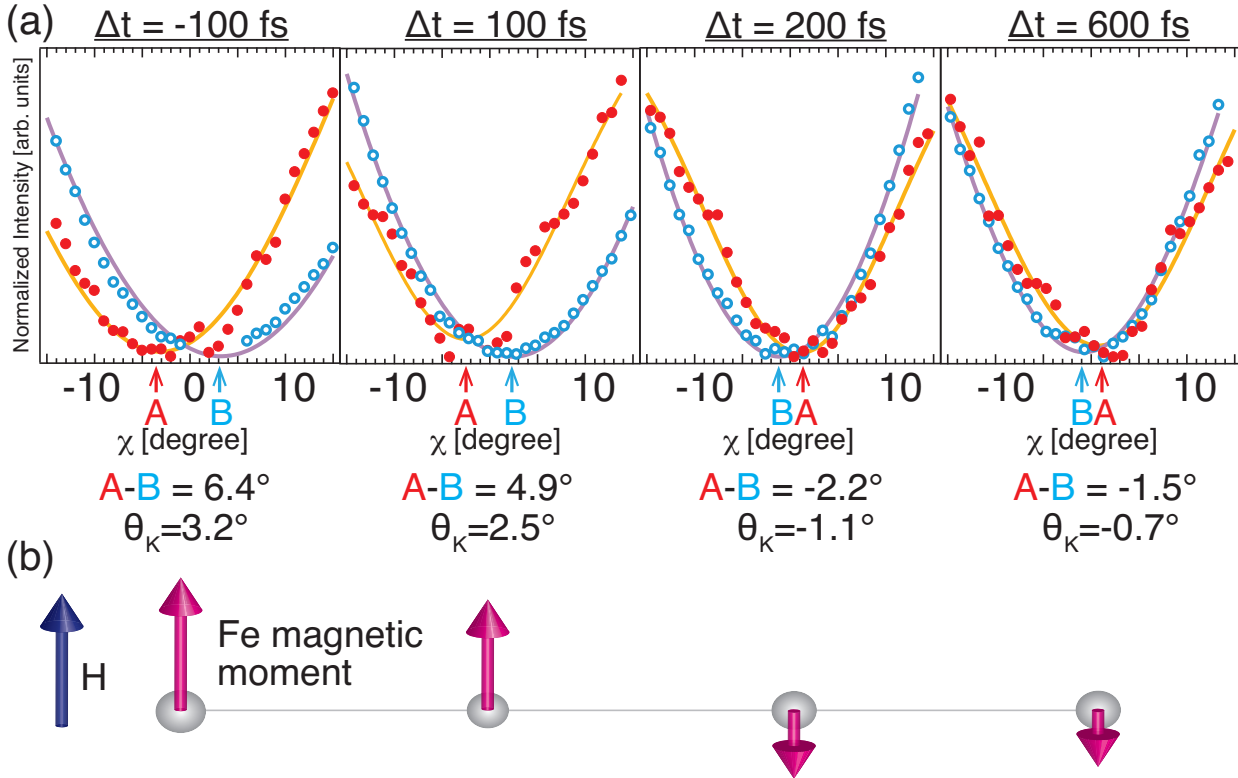


FIGURE 5.12: (a) RAE results (circles) at each delay time using FEL tuning to the photon energy of 53 eV. Solid lines represent the cosine fitting to the experimental values. (b) A schematic of the transient Fe magnetic moment with regard to an applied magnetic field, \mathbf{H} . The arrow length at each delay time corresponds to the magnitude of the Kerr rotation angle shown in (a).

subpicoseconds timescale with element specificity. Regarding a static measurement, XMCD has largely been utilized for probing spin and orbital magnetic moment through magneto-optical sum rules [96] in the various detection mode: the electron-yield, reflection, transmission and fluorescence yield mode at synchrotron radiation facilities. Up to now, magnetization dynamics pumped by linearly polarized light element selectively have been tracked by employing TR-XMCD in a reflection detection mode. In principle, both RMOKE and XMCD come from the absorption difference by a target magnetic materials between right- and left-circularly polarized light. Both spin-orbit and exchange splitting give the difference of absorption. Both technique can be used to investigate a depth-resolved profile of magnetization by varying the angle of incident light [202]. However, when compared with XMCD, the intensity measurements, RMOKE technique with the polarization analysis can give both dispersive and absorptive component of magneto-optical constants with a single experiment [148]. Furthermore, since the Kerr rotation angle can be extracted from the phase difference of curves measured

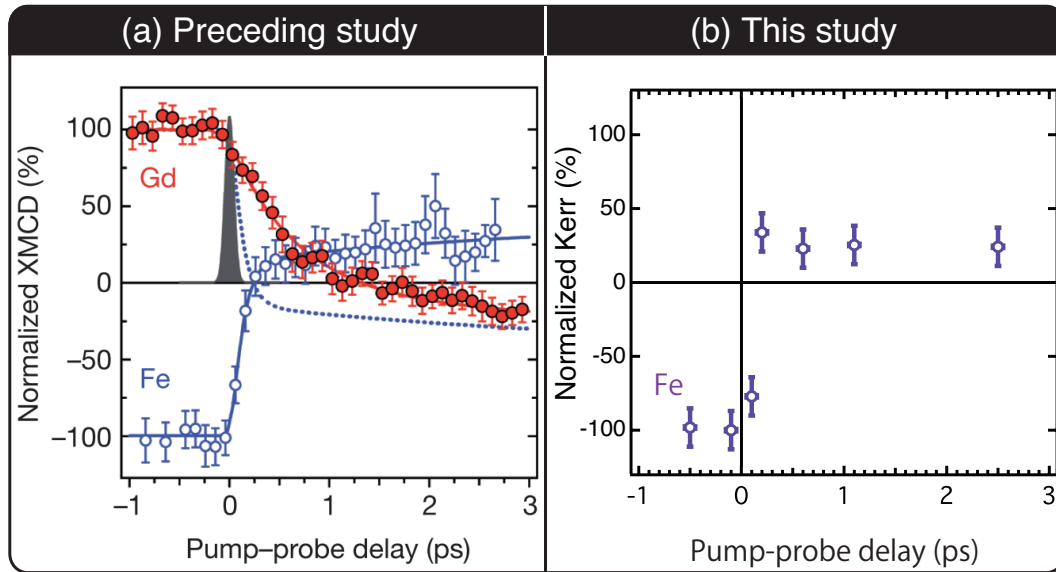


FIGURE 5.13: Comparison of pump-probe measurements between (a) TR-XMCD using laser slicing ([42]) and (b) Fe M -edge TR-RMOKE using FEL (this study)

by rotating the ellipsometry unit in the RAE method, this measurement scheme can detect small amount of change of Kerr angles [119]. The static RMOKE experiment shown in Fig. 5.9(c) shows that near 53 eV, the Fe M edge, nearly constant Kerr rotation angle (between 3 to 4 degrees) was detected with respect to photon energy. Therefore in the time resolved measurement on GdFeCo using FEL, RMOKE is more suitable choice than XMCD. It has been discussed that the time-dependent MOKE signals is not proportional to the magnetization during the femtosecond pulse due to excitation into a highly non-equilibrium state [203]. Since our target timescale in the current experiment was much larger than the dephasing time of correlation between spins and photons, the modulation effect caused by the non-equilibrium state can be disregarded in analyzing the time-dependent magnetization variation.

5.2.4 Conclusion

In conclusion, we measured ultrafast switching of Fe magnetization moment in a ferrimagnetic alloy, GdFeCo, within several hundred femtoseconds utilizing a seeded-type FEL set to the M -edge of Fe. Our results showed that magnetization switching due to ultrafast heating effect occurred when the temperature before pumping was above T_M . Through compared with the preceding results ([42]), the presented study showed that T_M was not crucial for the magnetization reversal. Further theoretical studies

are required for capturing the microscopic point of view for the light-induced ultrafast magnetization reversal. However, the new measurement scheme, TR-RMOKE using FEL will open the way to investigate both in-plane and out-of-plane magnetization dynamics of magnetic compounds element selectively.

5.3 Sensitivity for magnetization dynamics of subnanometer ultrathin magnetic film

Contents described in this section will be published elsewhere in the next 5 years and thus are currently unavailable on the web.

5.4 Development for resonant MOKE measurement system with a HHG laser

This section has been published as [204].

5.4.1 Introduction

Although using light in the soft X-ray region is useful, the availability of the measurements using FEL is limited because it is a large-facility based light source. The FEL can be used for one or two weeks per year. However nowadays, these drawbacks can modestly be resolved by using table-top laboratory-based soft X-ray light sources, high harmonic generation (HHG) laser (Fig. 5.14). HHG laser is able to produce ultrashort soft X-ray light pulses with the longitudinal and transverse coherence. Ti:S laser with ultrashort duration (tens of femtoseconds) is extensively used for driving laser of HHG. The pulse duration of HHG laser is less than that of the driving laser. Therefore the pulsewidth of HHG laser is known to be the smallest among pulsed light sources in the soft X-ray region and reaches down to subfemtosecond timescale. Because the linearly polarized HHG laser is compatible with RMOKE technique, a HHG laser can be employed as a compact tool for element-selective investigations of static and dynamical properties of magnetism in a laboratory environment [15, 39, 40, 205, 206]. These measurements were made using the geometry for transverse MOKE, and the spin variation was traced by measuring the intensity of the reflected beam from a magnetic sample. Such *intensity* measurements are restricted to the in-plane magnetization on a sample surface. In order to probe out-of-plane as well as in-plane components of magnetization element-selectively using linearly polarized light, RMOKE measurements with polarization analysis are indispensable. So far, RMOKE measurements with polarization analysis have been a large-facility based technique using synchrotron radiation (SR) [119, 128, 129, 132, 156, 158, 207]. The purpose of this development using HHG laser system is to conduct M -edge RMOKE measurements with polarization analysis on transition metals, which opens a way to develop time-resolved RMOKE measurements with polarization analysis in the future. Here, we present the development for RMOKE measurement systems with the polarization analysis and the first demonstration of longitudinal RMOKE measurements using the linearly polarized HHG laser. Rotating-analyzer ellipsometry (RAE) was incorporated for the polarization analysis.

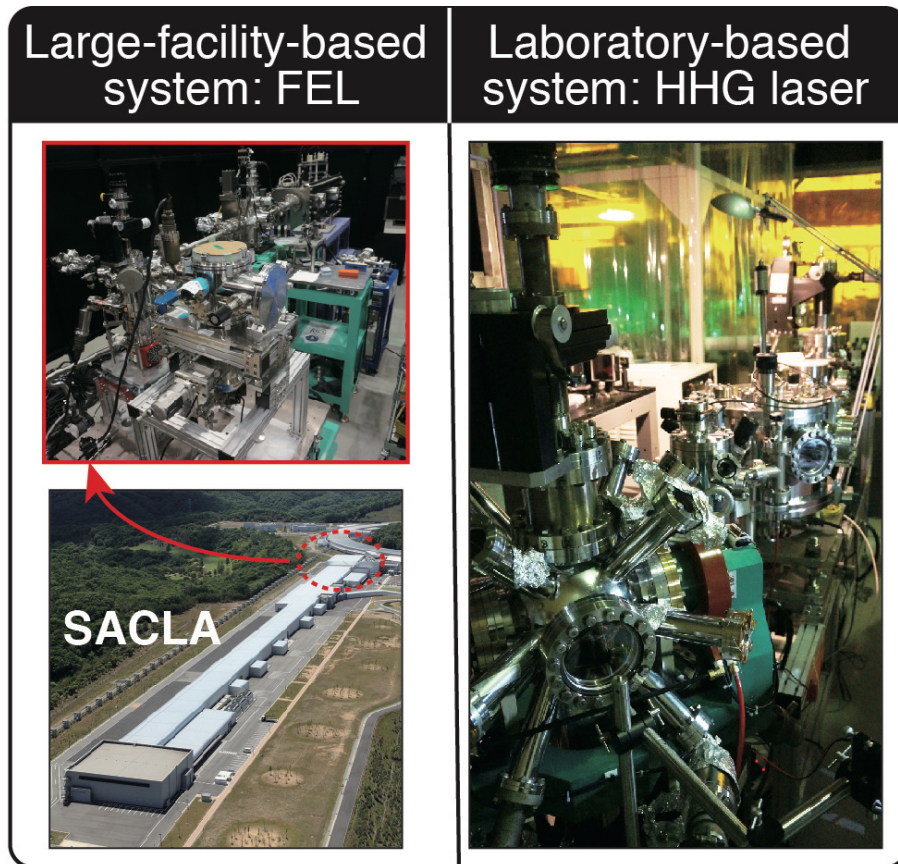


FIGURE 5.14: Comparison of large-facility based light source, FEL at SACLA, and a laboratory-based light source. In the image of SACLA, the end station of SXFEL beamline is shown. The image of SACLA was taken from <http://xfel.riken.jp/>.

5.4.2 Developments

Figure 5.15 presents the schematic diagram of the measurement system, which we call HHG beamline. The beamline is comprised of 1) titanium-sapphire (Ti:S) laser, 2) the gas-cell chamber, 3) the differential-pumping chamber, 4) the multilayer-mirror chamber, 5) the spectrometer chamber and 6) the electromagnetic-coil chamber connected with RAE unit. The 1) is used for the seed of the HHG. At 2), high harmonics with respect to the seed laser are generated. 3) is a vacuum buffer chamber between 2) and 4) with the vacuum pressure level of the order of 10^0 Pa and 10^{-6} Pa, respectively. At 4), the specific energy window is picked up from the high harmonic spectrum. 5) is used for evaluating the HHG spectrum. Finally, at 6) the RMOKE measurements with the polarization analysis are performed. The detailed explanations for each section are given below.

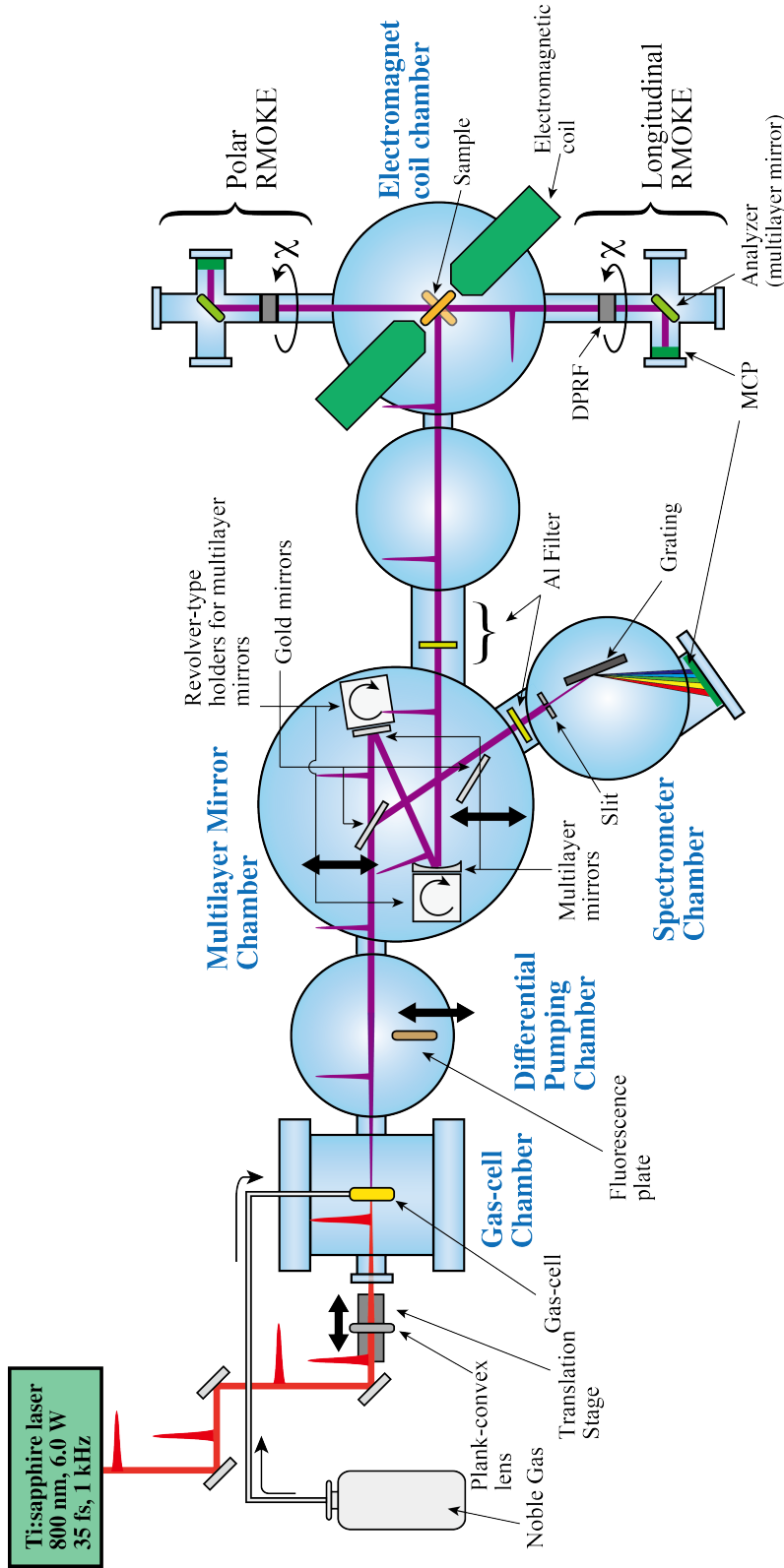


FIGURE 5.15: Schematic diagram (top-view) of RMOKE measurement system with a HHG laser. *p*-polarized Ti:sapphire laser is used and its electric field lies in the paper plane. Fluorescent plate in differential pumping chamber can be introduced on the light axis for confirming that the fundamental laser goes through the gas-cell holes. Gold mirror in multilayer mirror chamber can be translated into the light axis when measuring HHG spectra using spectrometer. By rotating the sample with regard to the axis normal to the paper surface, the in-plane or out-of-plane field can be applied with respect to the sample film surface, corresponding to longitudinal or polar RMOKE measurement, respectively. As a noble gas, Ne is used. There is the focus lens located at an upstream side of the gas-cell chamber with the focal length of 400 mm.

1) Ti:S laser system

Commercial Ti:S laser system, Astrella-1K-USP from Coherent, Inc., is implemented on an optical bench, which avoids a vibration influence, inside a hutch that keeps dusts and contaminants from entering. Temperature inside the hutch is kept and stabilized. The variation of temperature is within 0.5 degree over 48 hours. As a seed for HHG, this Ti:S laser is used. Pulse energy is around 6.0 W with the duration of < 35 fs and the wavelength of 800 nm at a repetition rate of 1 kHz.

2) Gas-cell chamber

First, the gas-cell chamber positions at the side of incoming beam in the HHG beam-line. A sapphire window is used as the incident port of the gas-cell chamber for enhancing a transmission of 800 nm light. At the gas-cell position, intense-fundamental laser and noble gas, Ne or Ar, introduced from an external gas line, interact together and generate odd numbered harmonics. At the upstream side of the gas-cell chamber, the plank-convex lens with a focal length of 400 mm is employed in order to focus the fundamental laser at the gas-cell position. The internal diameter of gas-cell is 4 mm and the diameter of a hole for introducing fundamental laser is $300 \mu\text{m}$. The high harmonic generation is extremely sensitive to the coupling condition between fundamental laser and the noble gas, therefore there are several adjusting mechanisms; i) focusing lens is mounted on the linear translation stage and focusing point can be adjusted with respect to the gas cell position. ii) gas-cell position itself is also adjustable by using *xyz*-stages, which enables the accurate alignment. iii) In addition to the translational adjustment of gas-cell, there are two axes for angular adjustments. From a gas cylinder, the noble gas is supplied to the gas-cell and it fills the internal space continuously. The gas-cell chamber is kept being pumped with turbo molecular pump (TMP). The pressure at gas-cell chamber with keeping flow of the noble gas is around 2.0 Pa. For controlling the gas flow quantitatively, a mass flow meter is equipped to the external gas line. Depending on the noble gas, the color of its ionization is different. In Fig. 5.16, ionization of Ne and Ar is shown.

3) Differential-pumping chamber

The differential pumping chamber follows the gas-cell chamber. This acts as a buffer chamber for improving the vacuum level gradually from the gas-cell chamber to the multilayer-mirror chamber. Inside this chamber, there is a translation stage. A fluorescence plate is equipped at the tip of the stage for confirming the fundamental laser passes through the hole of the gas-cell properly.

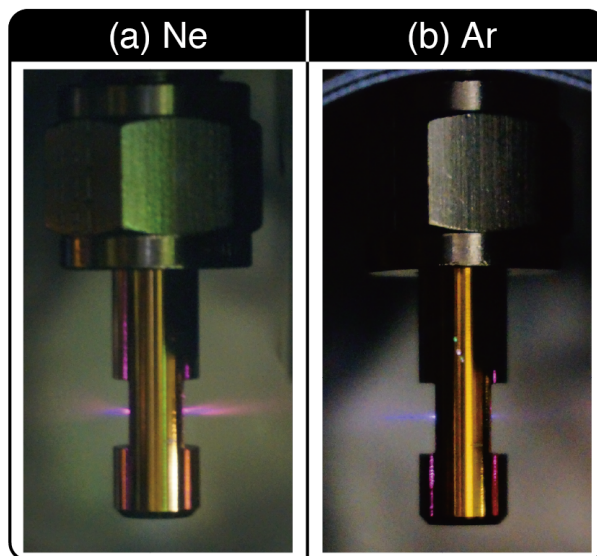


FIGURE 5.16: Ionization at gas-cell caused by interaction between fundamental laser and (a) Ne and (b) Ar.

4) Multilayer-mirror chamber

This chamber contains two multilayer mirrors and plays a role similar to the double crystal X-ray spectrometer implemented in an typical X-ray beamline at the third generation SR facility. These two reflection-type multilayer mirrors select particular energy window high harmonic spectra.

The incident angle is 9° , from the surface normal for both multilayer mirrors. The light injected into the first multilayer mirror, a plane mirror, has all of the components of the odd-numbered harmonics and a large part of the fundamental laser that is not transformed into high harmonics. After reflection from the first multilayer, the beam proceeds to the second multilayer, a concave mirror. This second multilayer also acts as a focusing mirror with length of 1214 mm for horizontal and 1278 mm for vertical direction. The difference is due to the nature of the concave mirror. If the toroidal mirror is used, the focal length for the vertical direction becomes the same as that for horizontal direction. The multilayer mirrors can be aligned using motorized angular adjusting system for vertical and horizontal direction under ultrahigh vacuum environment. Each multilayer mirror is mounted on the revolver-type holder that can accommodate four multilayers. Depending on a desired energy window, appropriate set of multilayer mirrors are chosen by rotating the revolver using a wobble stick without breaking the vacuum. The calculated reflectivity from these multilayer mirrors is presented in Fig. 5.17 in the case of Mo/Si with 12.4 nm periodicity and 30 repetition number, which

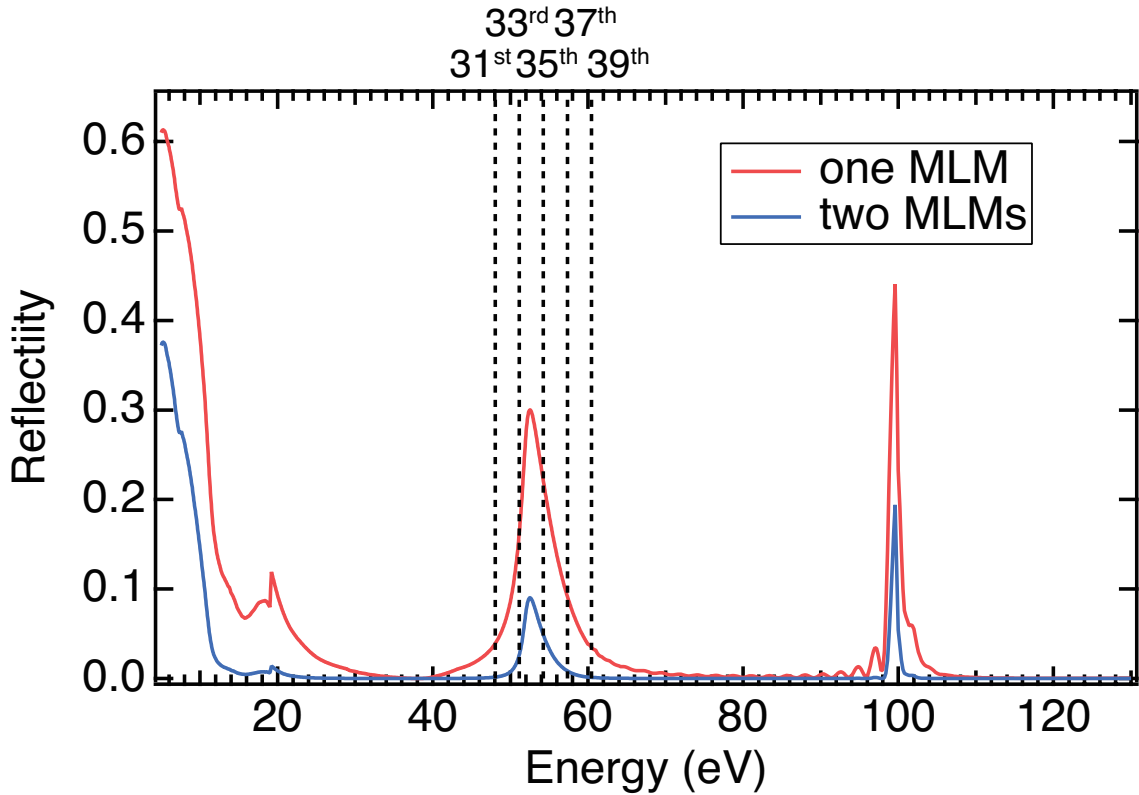


FIGURE 5.17: Calculated reflectivity (left axis) as a function of photon energy (5 - 130 eV) for Mo/Si multilayer mirror (MLM) installed in MLM chamber by using optical constants in Ref. [208] done by NTT-AT Inc., which is a manufacturer of the MLM. Red line is the reflectivity using one MLM and blue one is the reflectivity using two MLMs. High harmonic orders are also indicated assuming that fundamental laser is 800 nm. These harmonics region corresponds to M absorption edge of Fe.

is optimized for the M -edge of Fe (the photon energy of 53–54 eV). The reflectivity spectra of the multilayer mirror shows a peak around 53 eV. There is also a peak around 100 eV, which is the second-order Bragg peak.

There is a finite reflectivity below 20 eV in the reflectivity of the multilayer mirror as well as at a higher narrow energy window defined by the multilayer composition. In order to eliminate the energy lower than 20 eV, Al, N-Parylene (C_8H_8) $_n$, or Sc filter can be installed inside the triplex gate valve, which is connected to either the spectrometer or the electromagnetic coil chamber, at the downstream side of the multilayer mirror chamber. The transmission of Al filter with the thickness of 70 nm is given as the red curve in Fig. 5.18 In general, conversion efficiency of fundamental laser into the high harmonics is $\sim 10^{-5}$ – 10^{-8} [209, 210]. Therefore most part of the fundamental

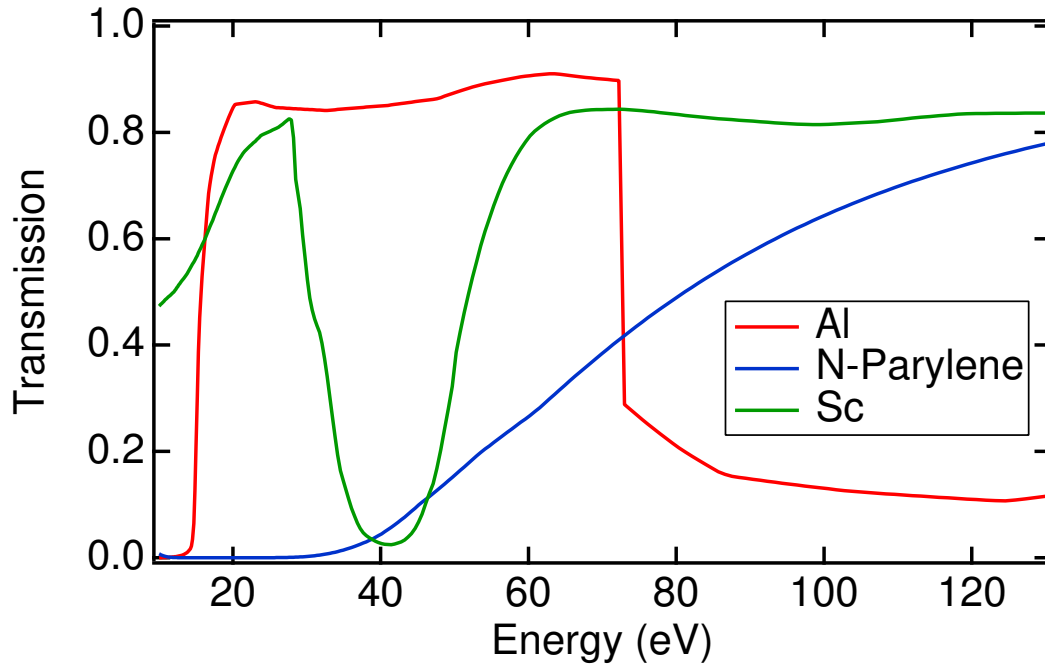


FIGURE 5.18: Calculated transmission for 700 Å Al (red), 1700 Å N-Parylene (blue) and 250 Å Sc (green) filter installed in the triplex gate valve located behind the MLM chamber [171].

laser passes through the gas-cell. Al filter removes the energy component below the ultraviolet range including fundamental laser. Due to Al $L_{2,3}$ -edges, this filter also attenuates energy above 72 eV. N-Parylene is used for attenuating light near 20 eV that cannot be eliminated by the Al filter. Depending on experiments, Sc filter is introduced for attenuating energy ~ 40 eV. The calculated transmission is shown in Fig. 5.18.

5) Spectrometer chamber

HHG spectrum measurements are exclusive with regard to the RMOKE measurements. When HHG laser is introduced to the spectrometer chamber from the multilayer mirror chamber, the Au mirror is translated onto the beam axis as shown in Fig. 5.15. There are two Au mirrors inside the multilayer mirror chamber; upstream one is used when the whole HHG spectra are measured and the downstream one is employed when the energy window selected by multilayer mirrors is evaluated. The HHG light is transferred to the Rowland-type grating with 1200 grooves/mm (30-002, Shimadzu Inc.). The incident angle into the grating is 87° from the surface normal. The diffracted light with energy-dependent angle variation are measured by micro-channel

plate (MCP) (Hamamatsu Photonics Inc., F2813-22P58, 22 means 2 stages and channel diameter is 15 μm and P58 corresponds to fluorescent material). The fluorescent plate behind the MCP makes it possible to visualize the spectra. At the incident port of the spectrometer, there is an incident slit with the horizontal width of hundreds of μm . Assuming that the Rowland condition is met, the width of the incident slit determines the energy resolution of the spectrometer. In the current setup with the 200 μm width, measurements are done with $E/\Delta E \approx 90$ at 53 eV.

6) Electromagnetic-coil chamber

Electromagnetic coil generates magnetic fields up to ± 0.5 T with a homogeneity of 1 % over 1 cm diameter sphere by supplying electric current with the maximum of ± 22 A by a bipolar power supply (BWS40-15, Takasago Inc.). A water-cooling system is equipped for the magnetic pole during operation. The magnetic pole itself is positioned inside the vacuum. With this electromagnetic coil, we can apply a magnetic field perpendicular and parallel with regard to the sample surface, which is enabled by the rotation of the sample holder with respect to the axis normal to the paper surface as shown in Fig. 5.15. The HHG hits a sample with an incident angle of 45° and the reflected light is transferred to a RAE unit for the polarization analysis. The RAE unit is comprised of the reflection-type multilayer mirror (Mo/Si, periodicity 15.6 nm, repetition number 10) and MCP detector (F4655, Hamamatsu Photonics Inc.). The transferred light impinges on the multilayer mirror in the RAE unit with the incident angle of 45° , where the ratio between s - and p -polarized reflectivity (r_s/r_p) is on the order of ten. By using the differential pumping rotary flange driven by a pulsed motor, this unit can be rotated together with respect to the light axis of the reflected light from the sample. At both sides of the ports normal to the incident light, RAE unit can be equipped as shown in Fig. 5.15. Depending either on a longitudinal or polar geometry, one of the RAE units is employed for the determination of Kerr rotation angle. Combining these two geometries, in-plane and out-of-plane magnetization can be measured in an element-selective way without breaking the vacuum if the magnetization is not canted. In the oblique incidence in the currently developed setup, the detected Kerr angle contains both polar and longitudinal contributions if the magnetization is canted from the direction either parallel or perpendicular to the sample surface in a system. By using liquid-He flow-type cryostat and temperature controller, sample temperature can be varied from 10–300 K. Measurements are usually operated under 5×10^{-6} Pa. In this vacuum pressure level, the degas from the magnetic pole does not deteriorate the pressure. The volume inside the chamber is so small, 9200 cm^3 . For pumping the this volume, it takes less than a hour from atmospheric pressure.

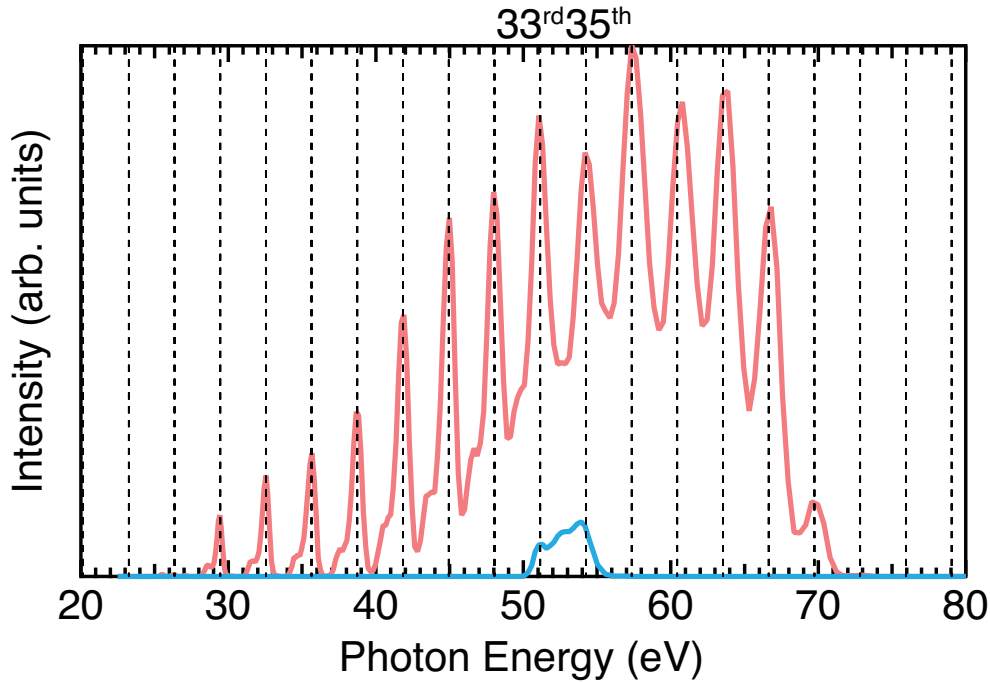


FIGURE 5.19: High-order harmonics spectra before (red) and after (blue) the multilayer mirrors as shown in Fig. 5.15. Cutoff energy was 45th order, which corresponds to ~ 70 eV. After reflection from two multilayer mirrors, the energy window around Fe M -edge is obtained. The vertical broken line indicates the position of the harmonic order.

5.4.3 Experiment

HHG spectrum

In Fig. 5.19, the HHG spectra before and after the reflection from two multilayer mirrors (Mo/Si, periodicity: 12.4 nm, repetition number: 30) are presented for the fundamental laser with the fluence of 2.67 mJ/pulse, which gives photon flux of $\sim 1.1 \times 10^{16}$ photons/pulse. In this measurement, Ne gas was employed for the generation of high-order harmonics. The input beam size into the focal lens is ~ 10 mm. The comparison between the two spectra confirms that multilayer mirrors act as a monochromator. The separation of the energy window around Fe M -edge from the whole HHG spectra was successfully performed. Other energy region can also be extracted if a different multilayer mirror, which has a peak of reflectivity at a specific energy region, is used. The broadened spectra are due to the deviation from the ideal Rowland condition.

Under the following parameter; $I_p=21.56$ eV (ionization potential) for Ne, $\lambda=800$ nm, pulse energy: 2.67 mJ/pulse, pulse width: ~ 100 fs, and beam diameter: 100 μm , the ponderomotive energy (Eq. (3.10)) is estimated to be 20.2 eV and the cut-off energy is expected to be 86 eV by using Eq. (3.11) in the framework of three-step model described in Sec. 3.2. The observed cutoff energy is smaller than the calculated one. There are several factors that are sensitive to high harmonic generation efficiency; 1) misalignment of gas-cell to fundamental laser, 2) optimization of focal length, 3) selection of interaction length and hole diameter of gas-cell, and 4) noble gas pressure. It is supposed that improvement of these factors enhances the accuracy of phase-matching condition, which results in the extended cut-off energy.

Demonstration of longitudinal RMOKE

We demonstrated longitudinal RMOKE measurements on Fe(001)- $p(1\times 1)$ films terminated by oxygen (Fe(001)) grown on MgO(001) substrates [211] using the light with the energy window shown in Fig. 5.19. The power of the fundamental laser was set to 2.67 W. Current target sample is the in-plane magnetization film. The results obtained using this system are shown in Fig. 5.20. The whole data for both magnetic field directions shown in Fig. 5.20 was collected within 20 minutes including the time for the field reversal. The experimental data are fitted by Eq. (4.10).

$1.9^\circ \pm 0.25^\circ$ of the Kerr rotation angle was extracted. The error bar is determined from the fitting. In the visible range, the Kerr angle of an iron thin film in the longitudinal geometry is ~ 0.02 degree [212]. In the current study, the giant magneto-optical response was demonstrated due to the resonant enhancement at the inner-core absorption edge [119, 128, 129, 132, 156, 158, 207]. The order of the Kerr rotation angle in the RMOKE measurement is more than the experimental resolution using RAE method. If the optical alignment is fully optimized and the RAE measurement is conducted in a wider χ range (0° - 360°) than that shown in Fig. 5.20, the resolution for determining the Kerr angle using the RAE technique reaches to ~ 0.01 degree [213, 214].

If one tries to measure unknown magnetic samples, in principle, hysteresis loops can be also measured with the current system. This gives basic magnetic properties such as coercive field and Kerr angles at a saturation field as shown in the previous reports using synchrotron radiation for RMOKE measurements [156]. In the hysteresis loop measurements, one can measure the intensity dependence on external magnetic field under fixing the χ at the angle where cosine curve becomes zero (At this point the largest variation of the field-dependent intensity is expected).

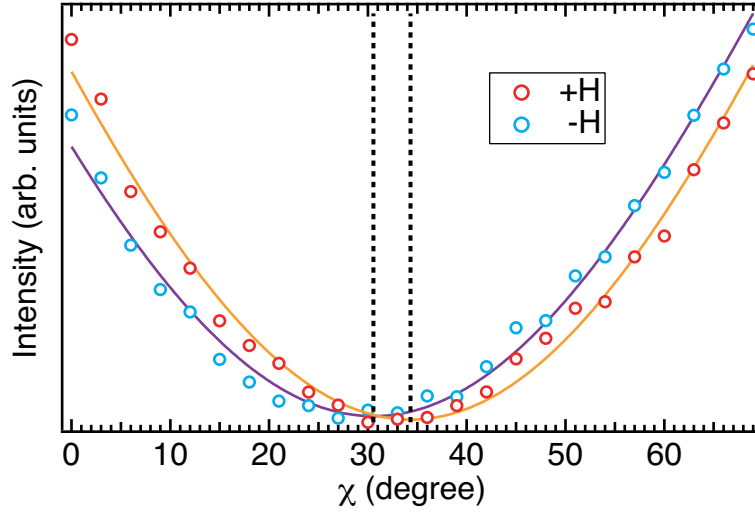


FIGURE 5.20: Demonstration of longitudinal RMOKE on Fe under surface-parallel magnetic field, $+H = 240$ mT (red circles) and $-H = -240$ mT (blue circles), application with $h\nu \sim 53$ eV. The broken vertical lines indicate the minimum positions determined by fitting using cosine curves (solid lines).

It is of interest to compare the RMOKE technique with a conventional probing technique of a ferromagnetic order, X-ray magnetic circular dichroism (XMCD), which uses circularly-polarized light in the HHG regime.

There were various methods for generating circularly-polarized high harmonics emission as discussed in Sec. 2.3, however these techniques for generating circularly-polarized high harmonics need much more complex experimental setup and fine-tuning of optical alignments. Furthermore, the degree of circular polarization, which depends on the photon energy and should be measured precisely, is below 75 %, so that the XMCD signals tend to become smaller than the intrinsic magnetic signals. In the preceding *M*-edge XMCD researches using HHG laser, transmission geometry was employed, which also makes a limitation regarding the material groups that the XMCD using HHG can apply. The number of photon flux itself in the case of circular HHG pulse was the similar order to that of linear HHG pulse [27, 29]. It was shown that for 3*d* transition metals, Fe, Co and Ni, the XMCD asymmetry were 7 %, 12 %, and 3 % respectively. Noise levels at the off-resonance region were 1-2 % (Fe), 3-5 % (Co), and 1 % (Ni). According to these preceding reports, signal-to-noise ratio (SNR) of *M*-edge XMCD for 3*d* transition metals is in 2 ~ 7. On the other hand, in the *M*-edge RMOKE, the SNR reaches to the order of 100 ~ 1000 by taking into account the resolution (~ 0.01 degree) of Kerr angle in RAE. Therefore, the probing technique in the linear-polarization scheme is preferred for detecting in-plane and out-of-plane

components of magnetization if the target sample has a minute magnetization. This is the case for ultrathin magnetic films and diluted magnetic semiconductors. It is of note that acquisition times for a certain energy range around M edge are shorter in XMCD (a few minutes \sim 10 hours [28]) than in RMOKE (tens of minutes \sim 2 hours).

5.4.4 Conclusoin and future prospects

We developed the RMOKE measurement system with the polarization analysis using laboratory-based light source, HHG laser. In this measurement schemes, in-plane and out-of-plane magnetization can be detected in the polar and longitudinal geometries, respectively. We selected the energy near Fe M edge from the high harmonic spectra by using two Mo/Si multilayer mirrors and the Al filter. We demonstrated longitudinal RMOKE measurements on the Fe film with this system using the RAE method. Kerr angle of 1.9° , which was 100 times larger than that in the visible range, was observed. This scheme has a sufficient resolution for detecting the Kerr angle in the M -edge RMOKE measurement.

It is of note that the currently developed system can easily evolved into the measurement for the vectorial magnetization in three dimension for ultrathin films by using p - and s -polarized light and two polar geometries, where in-plane azimuth angle of the sample is different by 90° each other, and one longitudinal configuration [215]. In addition, the transmission-type XMCD measurements can be possible by introducing a detector at the opposite port with respect to the incident port in our measurement system.

This system can be applied to the multi-component magnetic compounds with out-of-plane magnetization, such as $L1_0$ ferromagnetic alloy, and ferrimagnetic alloy composed of ferromagnet and rare-earth metals, e.g. GdFeCo, and TbFeCo [11] as well as the in-plane magnetic system. The mechanism of their magnetization behavior, especially magnetization reversal, in the sub-picoseconds timescale is one of the central issues in the field of femtomagnetism. Besides, the buried magnetism can be investigated using this system [12]. This material category has a nanometer-scale layered structure, such as magnetoresistance, spin-valve materials and magnetic topological insulators.

The nature of the ultrashort pulse of HHG laser can also be used for tracking laser-induced phenomena. In fact, HHG laser has been intensively applied in the field of ultrafast spin, carrier and molecular dynamics [216–219]. Recently, time-resolved TR-RMOKE in the transverse geometry and TR-XMCD measurements were conducted

on $3d$ transition metals in the energy region near M edges using the HHG laser as discussed in Sec. 2.2. Different from those previous researches, if our measurement schemes are extended into time-resolved scheme (Appendix D), TR-RMOKE using the polarization analysis can be performed under the magnetic field parallel (longitudinal) and perpendicular (polar) to the sample surface for multi-component magnetic materials. This polarization analysis gives time-dependent Kerr angles and ellipticity, both of which is required for extracting the intrinsic magnetization response ((see Sec. 5.1.2)) as pointed out by the preceding theoretical study [220]. It is expected that the time-resolved RMOKE with the RAE technique using the table-top HHG laser will be extensively facilitated in the field of femtomagnetism. We have already extended the static RMOKE measurement system using HHG laser, presented in this section, into time-resolved regime, which is presented in Appendix D.

5.5 Conclusion

In this chapter, we have extended RMOKE technique developed in Chapter 4 into the time-resolved scheme. Firstly, we demonstrated the first experiment of TR-RMOKE by observing ultrafast magnetization reversal of GdFeCo using FEL at FERMI. Not only did we show the ability that traces in sub-picosecond timescale, but also the role of the compensation temperature in magnetization reversal process. Secondly, we applied the TR-RMOKE measurements to ultrathin magnetic films and revealed that this method can trace with better signal-to-noise ratio and shorter measurement time compared to the conventional TR-XMCD measurements. Through the TR-RMOKE and TR-XMCD measurements, we explored the timescale of magnetization dynamics for Au/Fe/Au systems. In the relaxation process, we showed that the existence of the interface makes the lattice degree of freedom dominant in the relaxation from the laser-induced demagnetization process. Furthermore, the demagnetization timescale of a-few-monolayer Fe film was discovered within ~ 300 fs. Using the TR-RMOKE technique with a smaller jitter value, it is expected that the intrinsic demagnetization timescale will be extracted, which gives the importance of the spin-orbit coupling in spin-flip processes in the demagnetization phenomena. Thirdly, we developed RMOKE measurement systems using a HHG laser, which is a laboratory-based light source. These measurement schemes can be complementarily used with FEL measurements for investigating ultrafast spin dynamics.

Finally, we give open questions in the study of ultrafast spin dynamics, which the new technique developed in this thesis, TR-RMOKE using a FEL, can be applied in order to deepen the understanding of the mechanism underlying the laser-induced phenomena. Basically, this technique have sensitivity to a subnanometer-scale system with the sub-picosecond time resolution, it is suitable to investigate the role of interface in the magnetization dynamics, which is poorly understood in this field.

- An observation of ultrafast angular momentum transfer between baths of the spin and the lattice degree of freedom. This technique will reveal the role of interface in the angular-momentum transfer, which gives deeper insight regarding the demagnetization and the magnetization reversal process.
- Interaction between ultrashort pulses and magnetic materials such as chiral spin structures which is interfacially induced and has two competing energies between exchange and spin-orbit interaction. This can be measured by using circularly polarized pumping pulses.

- The role of exchange interaction in the ultrafast spin dynamics. This can be investigated by combining the TR-RMOKE technique with high magnetic fields that suppress the spin dynamics and enable one to observe dynamics related to the exchange interaction.
- The role of spin currents (so called superdiffusive current in this field) that affects demagnetization process. Especially, it is still not well known how the transient spin accumulation at interfaces acts in the nonlocal spin current transport. This can be investigated by pumping the magnetic layer from one side of a target heterostructure and probing the nonmagnetic layer from the other side of the system in the TR-RMOKE regime.
- Direct observation of the phonon excitation in the transient magnetization phenomena. Combining TR-RMOKE with time-resolved diffraction technique, spin and phonon excitation can be traced simultaneously.
- The role of exchange couplings of metallic alloys and multilayer systems in ultrafast magnetization reversal. So far, the magnetization reversal has been observed in the limited material groups, alloys and heterostructures. Although the underlying mechanism of the laser-induced magnetization reversal is still not clear, it seems that the intersublattice and interfacial exchange interaction plays an important role in this process. In order to investigate this topics, element-selective methods are required, and the TR-RMOKE technique fits for this study.

Chapter 6

Resonant enhancement of second harmonic generation in the EUV region

This chapter is covered by the publication list [3]. This paper is in press in the journal of Physical Review Letters.

6.1 Introduction

In Chapter 5, we have developed time-resolved resonant MOKE (TR-RMOKE) using a free electron laser (FEL) and a high harmonic generation (HHG) laser. It is quite important from the spintronic point of view that the detection of magnetization at buried interface, where the spatial inversion symmetry (IS) is broken. Therefore it is desired to develop a measurement scheme with element selectivity and probing ability that detects signals from systems without IS. In the visible region, magnetization-induced second harmonic generation (MSHG) has been often used for the detection of systems that lack IS as explained in Sec. 2.2. SHG measurements in soft x-ray range is expected to give information of electric and magnetic ordering for each element in noncentrosymmetric media as presented in Sec. 2.4.5. However, in the soft X-ray region, nonlinear optical effects have not been observed until recently. As a first step in this direction, the SHG signals in the soft x-ray range from noncentrosymmetric media needs to be verified. In this chapter, we explore the feasibility of soft-x-ray SHG

measurements that detect crystallographic SHG which has time invariant property as shown in Fig. 6.1. This corresponds to $\chi^{(i)}$ which is introduced in Sec. 2.4.5.

Soft x-ray SHG

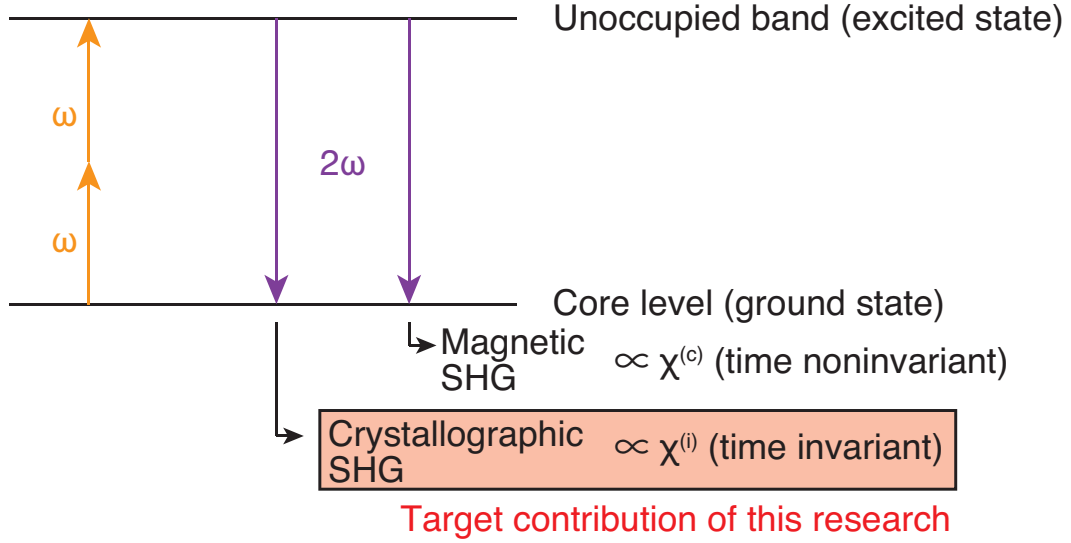


FIGURE 6.1: SHG signals in the electric-dipole regime are composed of terms that have time-invariant ($\chi^{(i)}$) and invariant ($\chi^{(c)}$) tensor. SHG itself has not been reported in the preceding study. In this chapter, we focus on detecting SHG signals from crystallographic component ($\chi^{(i)}$) as a first step in the direction of the nonlinear regime of magneto-optical effects in the soft x-ray range.

The extremely low nonlinear optical signals in the ultraviolet \sim X-ray range have allowed researchers to only perform transmission experiments of the gas phase or ultrathin films [221–226]. In this chapter, we present SHG of the reflected beam of a soft X-ray FEL from a solid, which is enhanced by the core-level resonant effect in the material. The effect inherently indicates addition of element specificity in SHG and it will be applicable for a wide range of samples, from nonlinear crystals to heterojunctions.

The phenomena of SHG can be expressed in terms of the second-order nonlinear susceptibility $\chi_{ijk}^{SHG}(2\omega; \omega)$, which becomes zero for centrosymmetric systems in the electric-dipole regime [227–230]. The $\chi_{ijk}^{SHG}(2\omega; \omega)$ can be enhanced when the photon energy ($2\omega; \omega$) matches the energy difference of the electronic states of a material (Fig. 6.2(a)). With the electric fields $E_j(\omega)$ and $E_k(\omega)$, the SHG $P_i(2\omega)$ is expressed as $P_i(2\omega) = \epsilon_0 \sum_{jk} \chi_{ijk}^{SHG}(2\omega; \omega) E_j(\omega) E_k(\omega)$. Under the perturbation approximation,

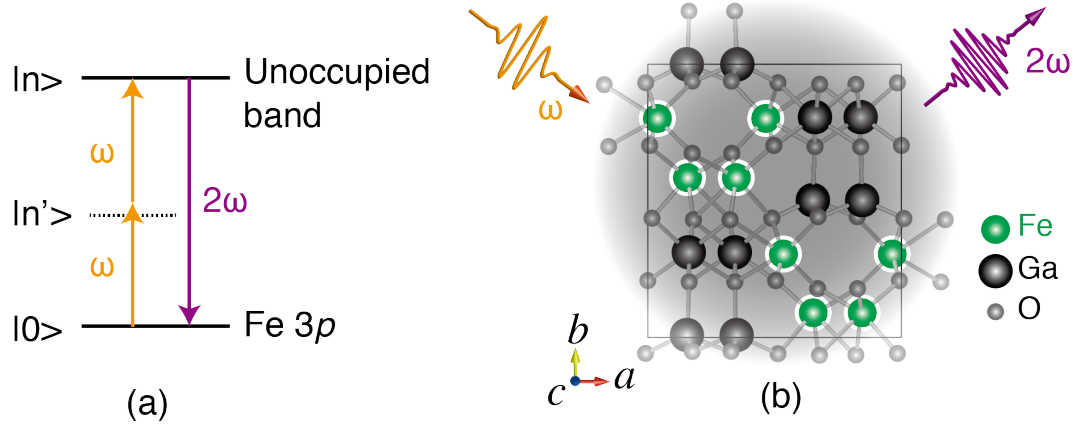


FIGURE 6.2: **Second harmonic generation in the GaFeO_3 crystal using Fe $3p$ resonance.** **a** Energy diagram of SHG. The notations, 0 , n' , and n represent the ground state, virtual state, and excited state, respectively. **b** Projection view along the c axis of the crystal structure of GaFeO_3 .

$\chi_{ijk}^{SHG}(2\omega; \omega)$ is simply written as [229]

$$\chi_{ijk}^{SHG}(2\omega; \omega) = \frac{N}{\epsilon_0 \hbar^2} \sum_{nn'} \left(\frac{\langle i \rangle_{0n} \langle j \rangle_{nn'} \langle k \rangle_{n'0}}{(\omega_{n0} - 2\omega)(\omega_{n'0} - \omega)} + \frac{\langle j \rangle_{0n} \langle i \rangle_{nn'} \langle k \rangle_{n'0}}{(\omega_{n0} + \omega)(\omega_{n'0} - \omega)} + \frac{\langle j \rangle_{0n} \langle k \rangle_{nn'} \langle i \rangle_{n'0}}{(\omega_{n0} + \omega)(\omega_{n'0} + 2\omega)} \right). \quad (6.1)$$

where $\langle j \rangle_{0n}$ is the j th Cartesian component of the dipole transition matrix element and N is the total atomic/molecular number density. The notations 0 , n' , and n represent the ground state, virtual state, and excited state, respectively (Fig. 6.2(a)). The denominators of the first and second terms, corresponding to the resonance factors and $\chi_{ijk}^{SHG}(2\omega; \omega)$, become large by the condition $2\omega = \omega_{n0}$ or $\omega = \omega_{n'0}$. Thus, if the photon energy of the ultrashort pulse laser can be tuned to the binding energy of the core-level state or the absorption edge in a material, the SHG signal in the soft X-ray region is likely to be enhanced by the core-level resonance effect.

SHG signals were detected when the photon energy with double frequency 2ω was above the absorption edge of the sample. The core-level resonance inherently indicates addition of element specificity to the SHG experiment. Furthermore, in the transmission-type SHG measurements, a phase-matching condition is important for coherent amplification of second harmonic waves which interact with second-order polarization. Therefore, the second harmonics are usually observed in a specific direction with respect to the direction of the fundamental wave. However, in the reflection measurement geometry, the phase-matching condition is automatically satisfied, which

results in that the present method can be used for various samples and experimental conditions. We also found good compatibility of the SHG measurement with the working principles of self-amplified spontaneous emission FEL (SASE-FEL). Experiments of optical frequency conversion with SXFEL are expected to reveal the origins of nonlinear effects in multicomponent materials and trace the ultrafast dynamics at the interfaces of heterojunctions.

6.2 Experiment

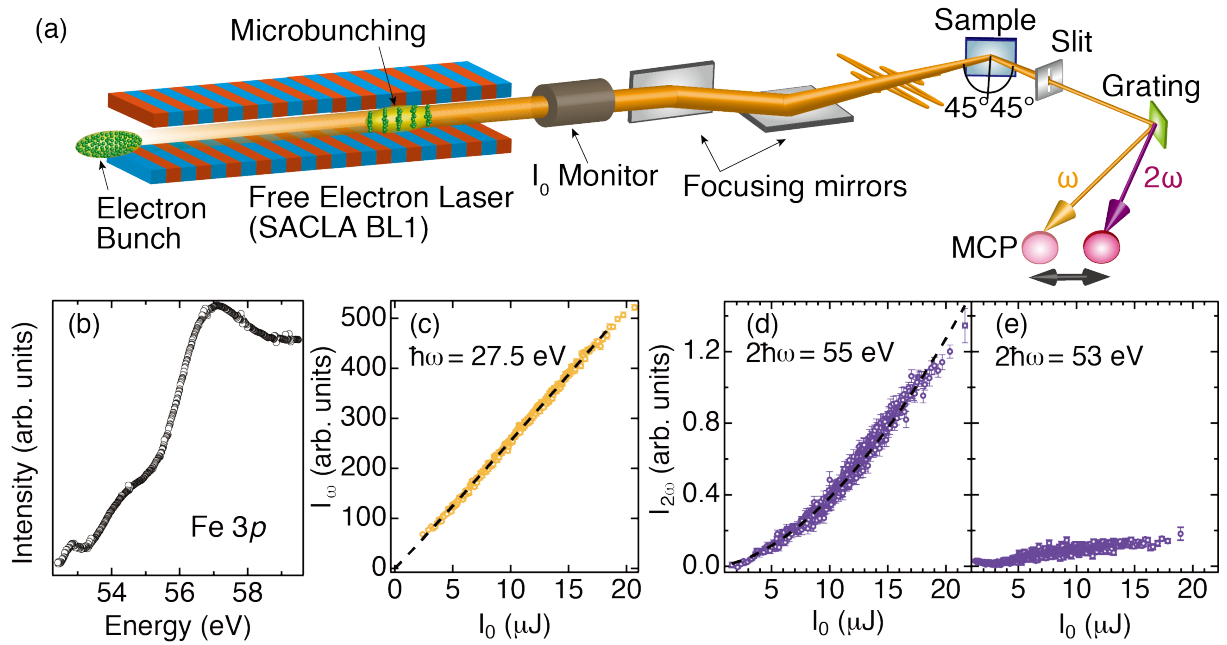


FIGURE 6.3: Measurement of SHG using SXFEL. (a) Schematic diagram of the SXFEL beamline (BL1) at SACLA and the SHG measurement system. (b) Fe 3p absorption spectrum of the GaFeO₃ crystal. (c) Intensity plot of the ω component of the reflected SXFEL pulses I_ω with respect to the individual incident intensity I_0 at the photon energy $\hbar\omega = 27.5$ eV. (d) Plot of $I_{2\omega}$ at the photon energy of $2\hbar\omega = 55$ eV. (e) Plot of $I_{2\omega}$ at the photon energy of $2\hbar\omega = 53$ eV. The dashed lines shown in (c) and (d) were fitted by a power law. The $I_{2\omega}$ values are normalized for comparison.

We measured the SHG signal from GaFeO₃ [231], which has a non-centrosymmetric orthorhombic structure with space group $Pc2_1n$ at room temperature and is known to show SHG in the visible region [232]. Figure 6.2(b) shows a projection view of the crystal structure along the c axis with spontaneous polarization along the b axis. The photon energy of the SXFEL pulse was set to near the half of the Fe 3p absorption edge

(Fig. 6.3). This absorption spectrum of the GaFeO₃ crystal was taken at a bending-magnet beamline, BL5B [233] at UVSOR facility in Japan. The absorption originated from Fe 3*p* edge is risen from ~ 54 eV. Thus, the SHG resonance condition ($2\omega = \omega_{n0}$) is satisfied by the energy difference between the Fe 3*p* level and the unoccupied band, as shown in Fig. 6.2(a). The SHG experiment was performed with a SXFEL pulse generated at BL1 (the SXFEL beamline) of SACLA [234, 235]. Figure 6.3(a) shows an overview of the beamline and the measurement system. A FEL beam was generated by the principle of SASE, which is associated with formation of the microbunching structure of an electron beam. The SXFEL was operated with a repetition rate at 60 Hz. Owing to the SASE scheme, the intensity of the SXFEL pulses fluctuated by 32%, which was evaluated by the coefficient of variation, and the incident power I_0 was evaluated using photoionization of Ar gas at the I_0 monitor in a shot-by-shot manner. With the spectrometer installed at the beamline, we confirmed that the intensity of the second-order harmonics of SXFEL or spontaneous undulator radiation was below the detection limit. The SXFEL pulses with durations of 100 fs and energies of up to 25 μ J were irradiated onto the sample with the *p*-polarized configuration along the spontaneous polarization axis (*b* axis) of the GaFeO₃ crystal with an incident angle of 45° with respect to the sample normal. The spot size of FEL at sample position was ~ 100 μ m. The reflected SXFEL beam with an angle of 45° entered into a spectrometer composed of a slit, a grating, and a microchannel plate (MCP) detector. The spectral intensities of the reflected light (I_ω and $I_{2\omega}$) were measured by the MCP position, as shown in Fig. 6.3(a). The intensities of the spectral components ω and 2ω were measured in a shot-by-shot manner with individual I_0 shots. Setting the spectrometer at the 2ω configuration, we confirmed that the photoluminescence light from the sample after the two-photon absorption process [236, 237] was below the detection limit.

6.3 Results

6.3.1 Second harmonic generation measurement using FEL

Figure 6.3(c) shows a plot of the variation of the reflected intensity at a photon energy of $\hbar\omega = 27.5$ eV with respect to the incident intensity I_0 . The dashed line represents fitting using the power law $\propto I_0^\beta$. The exponent coefficient $\beta = 1.0$, which means linearity of the ω component. The intensity of the 2ω component ($2\hbar\omega = 55$ eV) shows apparent nonlinear dependence with I_0 , as shown in Fig. 6.3(d). Moreover,

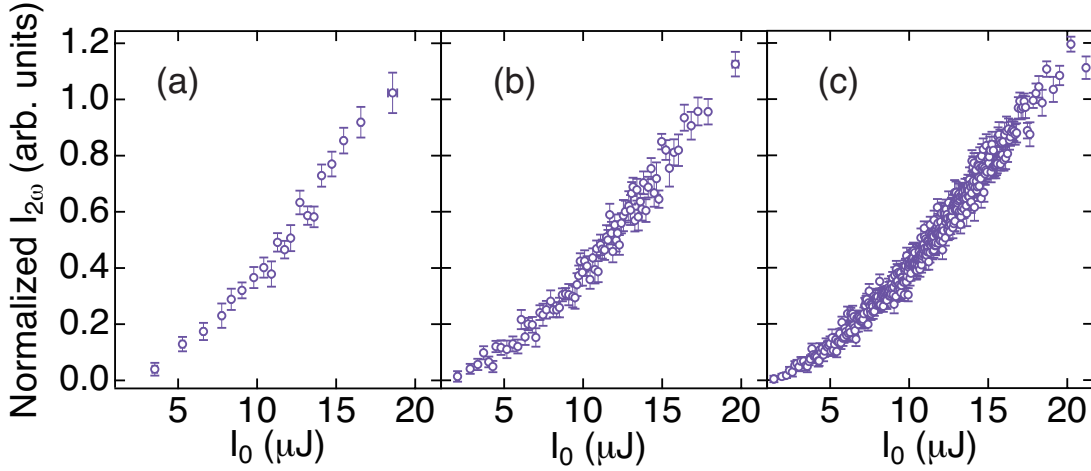


FIGURE 6.4: Measurement of the SHG power dependence. Temporal variation of the $I_{2\omega}$ - I_0 diagrams during the measurements.

the 2ω signal disappears when the photon energy is tuned to $2\hbar\omega = 53$ eV ($\hbar\omega = 26.5$ eV), which is below the Fe $3p$ absorption edge (Fig. 6.3(e)).

It is worth noting that the individual measurements of the $I_{2\omega}$ - I_0 diagrams in Figs. 6.3 were performed without artificial regulation of the I_0 intensity and they were completed after several minutes. The inherent intensity fluctuation of SXFEL allows experimentalists to automatically obtain the data, as shown in Fig. 6.4. For a single measurement at each data point, the data points ($I_{2\omega}$, I_0) of individual shots initially appear random, but they show apparent dependence after a sufficient number of shots. Good compatibility between the SHG measurements and SXFEL is beneficial for efficient experiments in limited beam time.

Figure 6.5 shows $I_{2\omega}$ - I_0 diagrams in the logarithmic scale with different photon energies. The features of Fe $3p$ absorption of GaFeO₃ are observed above 54 eV and, correspondingly, quadratic intensity dependence of the SHG light is shown in Fig. 6.5 observed in the same region. From power-law fitting, the exponent coefficients are $\beta = 1.7$ ($2\hbar\omega = 55$ eV), $\beta = 1.9$ ($2\hbar\omega = 57$ eV), and $\beta = 1.9$ ($2\hbar\omega = 59$ eV). The experimental values consistently match the quadratic intensity dependence ($\beta = 2$) of the SHG light. These results unambiguously indicate detection of SHG light from the GaFeO₃ crystal, which is enhanced by the resonance effect of the Fe $3p$ core level.

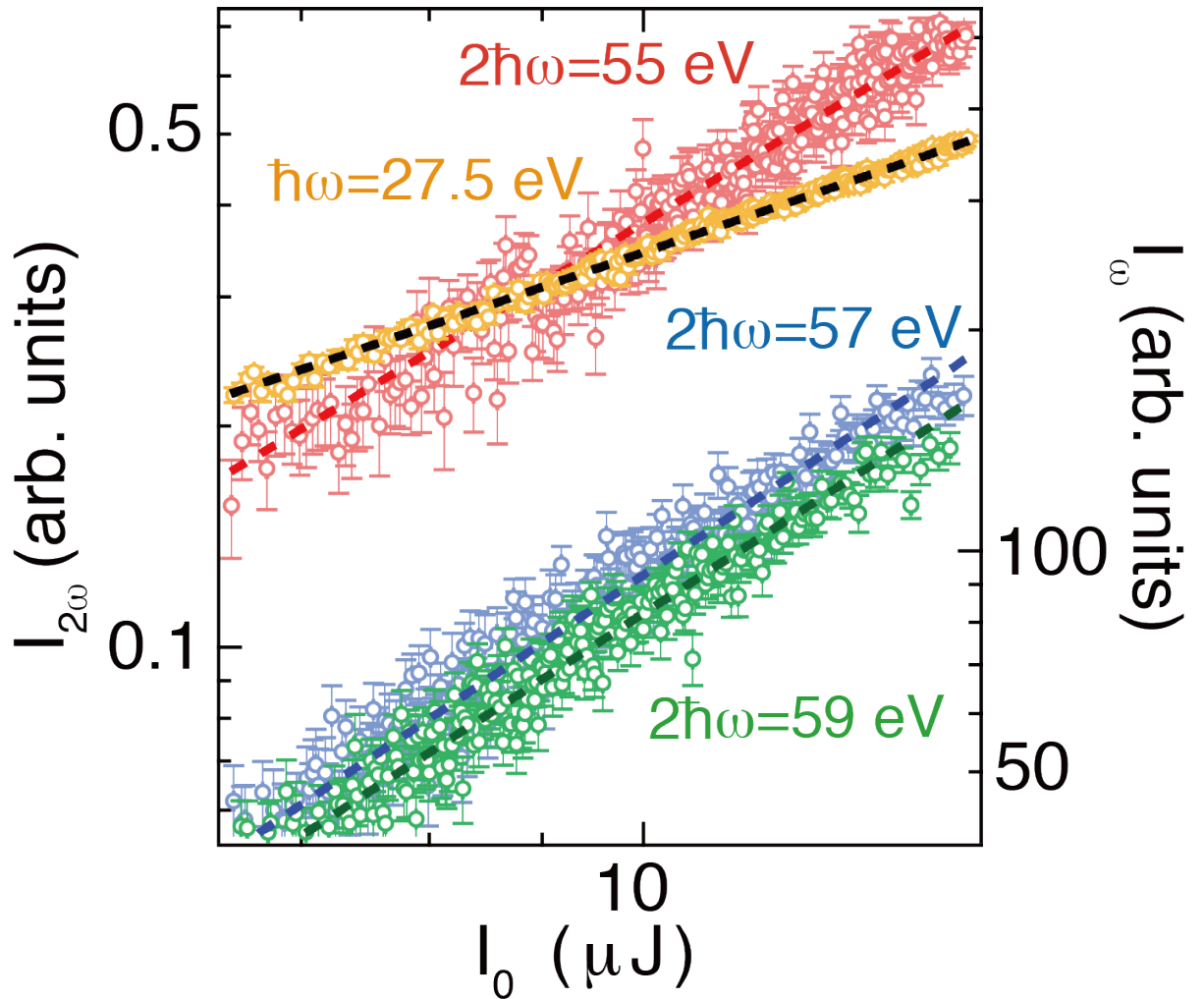


FIGURE 6.5: Logarithmic $I_{2\omega}$ - I_0 diagrams. $I_{2\omega}$ is plotted on the left axis for the photon energy of $2\hbar\omega = 55$ eV (red circle), $2\hbar\omega = 57$ eV (blue circle), and $2\hbar\omega = 59$ eV (green circle). The dashed lines were fitting using a power law. I_ω (orange circle) is plotted on the right axis for $\hbar\omega = 27.5$ eV.

6.3.2 X-ray photoelectron spectroscopy

We performed X-ray photoelectron spectroscopy (XPS) around O 2s peak on GaFeO₃ using synchrotron radiation at BL-2A MUSASHI of the Photon Factory (PF), KEK, Japan. Fig. 6.6 shows the normal-emission XPS spectrum obtained at room temperature with the incident photon energy of 56 eV. The total energy resolution evaluated by the Au 4*f* state is 41 meV for the photon energy of 56 eV. The peak positions were determined using multi-peak fitting composed of two Gaussian functions after the subtraction of the background defined by the quadratic function. The quadratic

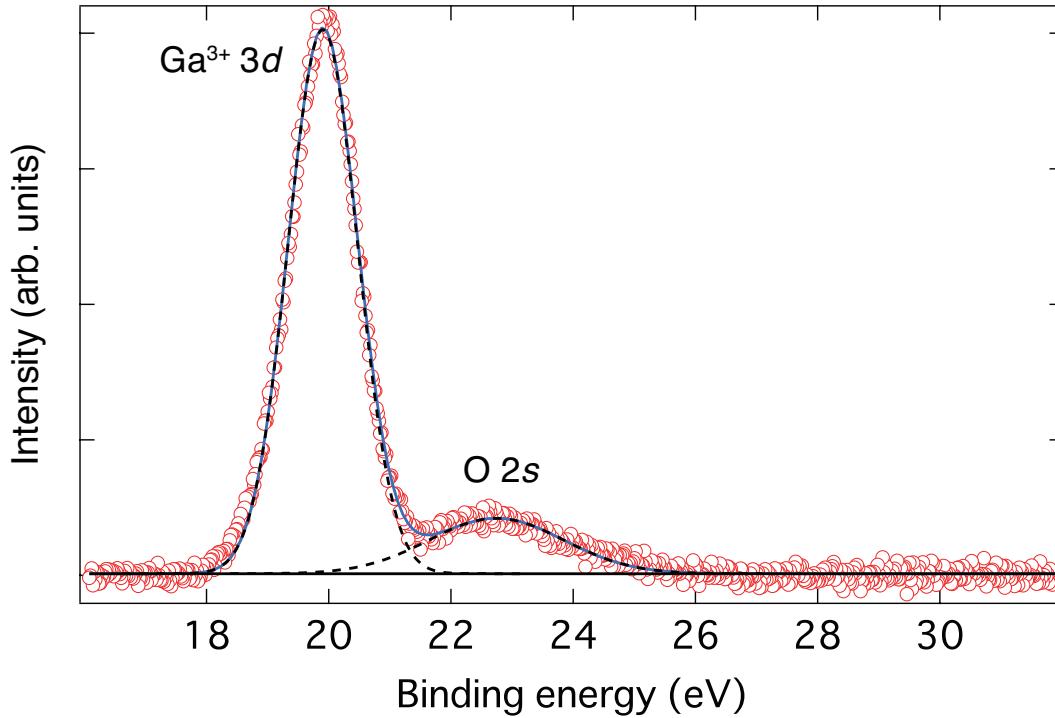


FIGURE 6.6: X-ray photoelectron spectroscopy of O 2s in GaFeO₃. X-ray photoelectron spectroscopy spectrum measured with the photon energy of 56 eV at room temperature. Red circles are experimental results. Blue solid line is the fitting composed of two gaussian functions. Each gaussian fitting results are shown in dotted black lines.

function for the background was generated through the fitting to the XPS raw data with masking the certain range from 17.6 eV to 25.8 eV as the unit of binding energy. The O 2s peak is partially overlapped with the oxidized Ga 3d peaks. Ga³⁺ 3d state can be seen in 19.9 eV. The O 2s peak is located at the 22.7 eV. These positions are consistent with the preceding reports [238, 239].

6.4 Discussion

The transition from O 2s to Fe 3d state corresponds to the energy slightly lower than $\hbar\omega$ used in the experiments. Therefore, there is a possibility that the double resonance condition shown in Fig. 6.7 were met in this SHG measurements. In this resonance condition, the transition from Fe 3p to O 2s state occurs when distribution of the Fe 3p states spreads over the O site and a magnitude of the matrix element becomes finite. This intriguing condition occurs in the SHG process that gives the additional enhancement that apparently satisfies the first term in Eq. (6.1).

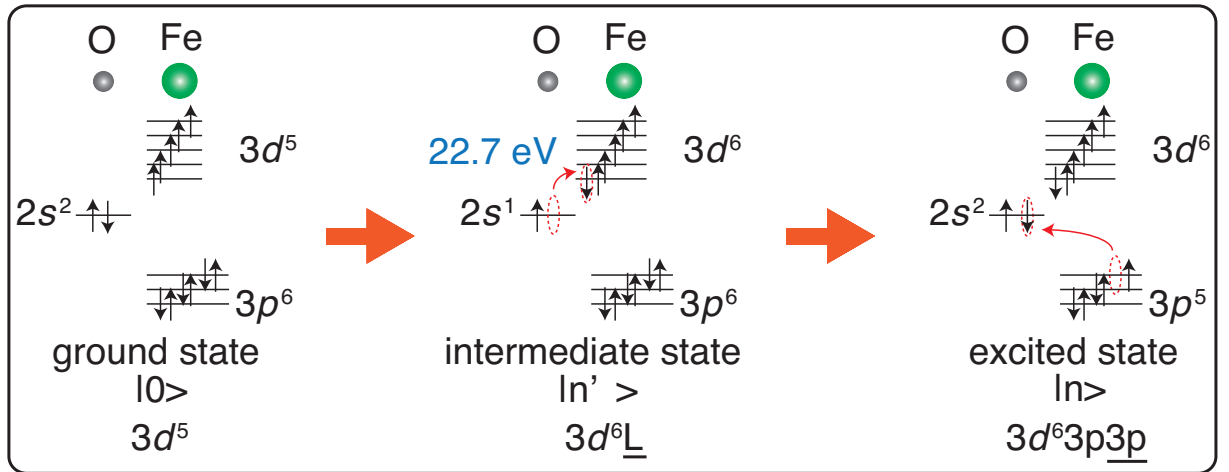


FIGURE 6.7: Possible double resonance mechanism in SHG measurements for GaFeO₃.

6.5 Conclusion

For the first time, we observed SHG from a nonlinear crystal in the soft X-ray region in the reflection geometry under the possible double resonant condition. The observation indicates addition of element specificity in SHG. The present method can be extended to a variety of samples, including the interfaces of heterojunctions, and many applications, such as the interface of the spintronic heterojunction under operation. Magnetization-induced SHG can be achieved with element selectivity of the magnetic atom at the interface.

The current measurement showed the feasibility of measuring crystallographic components of SHG signals in the soft x-ray range. In the previous SHG measurements in the visible range, the magnetic SHG signal is as large as that of the crystallographic contribution [91]. We here clarify the application of this technique which is sensitive both to crystallographic (including electric) and magnetic symmetry information. In principle, the target groups are i) a noncentrosymmetric crystallographic structure without magnetic order, ii) a centrosymmetric crystallographic structure with noncentrosymmetric magnetic order, iii) a noncentrosymmetric crystallographic structure with centrosymmetric magnetic order, and iv) a noncentrosymmetric crystallographic structure with noncentrosymmetric magnetic order. Therefore, the nonlinear-optical technique in the soft x-ray range has a various applications in the field of condensed matter physics and chemistry as follows:

- Ultrafast spin dynamics of antiferromagnets: antiferromagnetic order belongs to a larger variety of material groups including insulators, metals, semiconductors, superconductors, and semimetals, while ferromagnetic order is mostly observed in metallic materials. Furthermore, the antiferromagnetic order has much larger exchange interaction between spin sublattices when compared with ferro/ferrimagnetic order, which results in much faster spin dynamics than that of ferro/ferrimagnetic materials [240, 241]. The laser-induced ultrafast spin dynamics of a ferro/ferrimagnetic order can be traced by linear magneto-optical measurements that are developed in the previous chapter, however the antiferromagnetic order cannot be detected within the linear regime. The time-resolved SHG measurements in the soft x-ray range can trace the dynamics of antiferromagnetic order as well as ferro/ferrimagnetic order in a noncentrosymmetric media. This will provide deeper insight into the coherent interaction between femtosecond laser pulses and magnetic materials in the highly nonequilibrium state and reveal the role of exchange interaction in the magnetization dynamics.
- Multiferroics: multiferroic materials are known to show a coexistence of electric and magnetic order [242]. This class of materials has a potential to be implemented in new-generation devices in which the magnetization can be controlled by electric fields rather than magnetic fields or electric currents. This will provide faster, and more energy-efficient devices. The target materials are mostly multicomponent systems, such as BiFeO_3 , or orthorhombic/hexagonal RMnO_3 with $\text{R} = \text{Sc}, \text{Y}, \text{In}$ or Dy-Lu and so on [243]. Therefore, element-selective measurements are indispensable for investigating these materials. Among multiferroic materials, spin-driven multiferroicity has attracting attention because it shows the close correlation between the electric and magnetic order and partly shares the domain boundaries between those two ferroic orders [244]. The multiferroicity with this scheme (magnetic-order induced ferroelectricity) at room temperature has not been observed yet. Element-selective SHG measurements developed in this chapter will give a powerful tool for investigating these class of materials because, in principle, SHG is sensitive to the breaking of spatial and time inversion symmetry. Furthermore, recently not only bulk materials but also thin films or heterostructures are intensively investigated in this community for seeking new magnetoelectric functionalities that can be tuned at room temperature such as hexagonal YMnO_3 -permalloy [245], BiFeO_3 - CoFe heterostructures [246], and $\text{PbZr}_x\text{Ti}_{1-x}\text{O}_3$ - LaSrMnO_3 - $\text{PbZr}_x\text{Ti}_{1-x}\text{O}_3$ [247] and so on. For distinguishing roles carried by each element in the ferroic orders that appear only at the

interface, SHG in the soft x-ray range can also be effective because it can detect signals from the interface element selectively. Dynamical features that are important for the development of multiferroic devices have not well investigated yet so far. The current technique has a potential to extend into measurements in the time domain and can be useful also for the ultrafast spin dynamics that closely coupled with the ferroelectric order.

- Magnetic topological insulator: two groups of ferromagnetism in the topological insulators are reported: one is in the system with the interface between the ferromagnetic layer and the topological insulator layer [248, 249], and the other is in the diluted magnetic topological insulators [250, 251]. The origin of those ferromagnetisms, which breaks the time-reversal symmetry in the topological insulator, is still under debate. The ferromagnetism at the interface in the former case can be investigated by using magnetic SHG measurements in the soft x-ray range.
- Catalysis science: for developing energy-efficient solar cell, thin-layers structure has been attracting attention recently [252]. In these systems, at the interface, charges are separated and chemical energy transformation occurs in catalytic reactions [253]. Furthermore by using a optical laser together with a soft-x-ray FEL, surface/interface chemistry reactions can be traced with the subpicosecond time resolution [254]. Therefore, static and dynamical SHG measurements in the soft X-ray range can separately detect element in a series of chemical reactions. The current technique makes it possible to detect the presence of specific reaction products at the interface between solid and liquid/gas of a catalyst.

Chapter 7

Conclusions

7.1 Summary

We developed RMOKE techniques in the extreme ultraviolet (EUV) / soft X-ray region and extended them into time-resolved techniques using a free electron laser (FEL). These new techniques can detect out-of-plane as well as in-plane magnetization with element selectivity, track the laser-induced magnetization at the sub-picosecond timescale, and measure with a sensitivity to subnanometer-scale system.

- A static RMOKE measurement technique in a polar geometry was developed. Using rotating-analyzer ellipsometry (RAE), we measured the Kerr angle in the EUV region. The M -edge RMOKE measurement of Ni thin films using synchrotron radiation revealed a giant Kerr rotation angle, 50 times larger than that observed using conventional visible MOKE. The overall features of the spectrum were reproduced by a simulation based on resonant scattering theory. To extract more microscopic features from the RMOKE spectrum, first-principles calculations are required, but such calculations are beyond the scope of this thesis. We showed that our technique can be used to detect of out-of-plane magnetization with element selectivity.
- We extended the RMOKE technique into the time-resolved regime. We studied the ferrimagnetic alloy, GdFeCo, by using time-resolved RMOKE (TR-RMOKE) with a free electron laser (FEL) at FERMI@ELETTRA. By measuring the time-dependent Kerr angle using RAE, we tracked the ultrafast magnetization reversal of the Fe sublattice in GdFeCo at a delay time of 200 fs after irradiation with the

pump pulse. Considering the timescale of the magnetization reversal, our results are consistent with earlier results measured with time-resolved X-ray magnetic circular dichroism (TR-XMCD). Thus, TR-RMOKE can track magnetization dynamics at the sub-picosecond timescale. The mechanism of magnetization reversal in highly non-equilibrium states is not yet understood well, so further investigation is needed in other magnetic systems and ferrimagnetic systems. However, we revealed that the compensation temperature, T_M , was independent of the ultrafast magnetization reversal.

- We used the TR-RMOKE technique to study magnetic films with sub-nanometer thickness by using FEL at SACLA. We showed that TR-RMOKE with FEL can detect out-of-plane magnetization dynamics at the sub-picosecond timescale with a better signal-to-noise ratio and shorter measurement time than TR-XMCD with synchrotron radiation using laser slicing, the conventional element-selective technique. We revealed the timescales of the demagnetization and the relaxation process, which also depended on the thickness of the ultrathin magnetic layer, by using the developed TR-RMOKE technique and conventional TR-XMCD. We found that our technique is useful for revealing the magnetization dynamics of ultrathin magnetic systems with perpendicular magnetization, which are useful in spintronic devices.
- We developed RMOKE measurement system in a polar and longitudinal geometry using laboratory-based light source, a high harmonic generation (HHG) laser. The specific energy can be extracted from HHG spectrum by using two multilayer mirrors and an Al filter. Using this system, the longitudinal RMOKE measurements were demonstrated on the Fe thin film. We observed giant Kerr rotation angle, 1.9° , which is 100 times larger than that observed in visible MOKE.
- We explored the nonlinear effect in EUV region. We observed second harmonic generation (SHG) from a non-centrosymmetric crystal, GaFeO_3 , by using FEL in the reflection geometry. This was the first observation of SHG in the EUV region. Because of the existence of O $2s$ and the relatively broad spatial distribution of $3p$ states in Fe, the condition of double resonance seems to be met, which produced resonant enhancement of SHG signals. These results open the way toward extending the RMOKE technique developed in this thesis into the nonlinear regime.

7.2 Future prospect

The following can be considered as future prospects.

- Better time resolution using FEL: the time-resolution for the TR-RMOKE experiments using FEL in this thesis was limited by the pulse duration or jitter, which was approximately 100–300 fs. For time-resolved MOKE in the visible region, the typical temporal resolution is below 100 fs. By improving the upstream condition of the FEL facility and reducing jitter between the pump and probe pulse, TR-RMOKE using FEL can detect magnetization dynamics at timescales below 100 fs. Because demagnetization occurs at a timescale below 100 fs, improving the temporal resolution is also important in the FEL measurements.
- Laboratory-based time-resolved RMOKE studies involving the polarization analysis: We developed an RMOKE measurement system that uses rotating-analyzer ellipsometry with a high harmonic generation laser. Polarization analysis of RMOKE in polar and longitudinal geometries reveals the out-of-plane and in-plane magnetization, allowing one to use a laboratory-based light source to track the three dimensional spin information with element-selectivity. Our method can be used to complement methods using with a free electron laser, a source which requires a large facility, severely limiting its opportunity.
- Determination of the dispersive and absorptive part of the optical constants and dielectric tensor in the soft X-ray region: Polarization analysis of MOKE reveals both polarization rotation and ellipticity, which contain the dispersive and absorptive properties of the optical constants. The RMOKE investigated in this thesis can determine these material-dependent quantities in the EUV / soft X-ray region. This information is important for investigating linear and nonlinear optics and the magneto-optical effect in the EUV / soft X-ray region, in which element-selective measurements can be conducted.
- Optical components in the soft X-ray region using RMOKE: Through the RMOKE, the polarization state, θ_K , drastically changes, so this property can be used to change the polarization state in this energy region. Polarization is usually controlled by an undulator, but if we use the RMOKE of magnetic films we can change the polarization of the incident light without changing the upstream optical parameters. In transmission or reflection configurations, circularly polarized light can be generated just by inserting magnetic materials in the light axis in the EUV / soft X-ray region.

- Voltage effect on ultrafast spin dynamics: Recently voltage-induced magnetization has been intensively investigated because it enables the control of magnetism without applying a current or magnetic field, which cause heat problems. To develop ever-faster devices that operate using electric voltage, it is crucial to unravel the fundamental properties of how voltage affects ultrafast magnetization dynamics in a wide variety of materials. This research can be conducted using time-resolved RMOKE using FEL.
- Element-selective, time-dependent depth, and lateral profiles of magnetic structures: the RMOKE can be used to observe depth profiles by changing the incident angle and photon energy. Furthermore this method can be applied to an element-selective imaging technique that gives lateral magnetic information. By extending these properties to the time domain, one can track time-dependent three-dimensional magnetization dynamics with depth, and lateral resolution. These measurements are important for developing magnetic devices made from magneto-resistive, spin-valve, and exchange-coupled materials.
- Nonlinear RMOKE in the EUV / soft X-ray region using FEL: In magnetic materials, the SHG signal, or second-order nonlinear susceptibility, depends on magnetization. Therefore, our observation of resonant SHG in the soft X-ray region suggests that it is possible to probe interface magnetism with element selectivity by using the nonlinear RMOKE technique. This nonlinear effect in the EUV / soft X-ray region can also be applied to an imaging technique that can probe ferroelectric domains as well as ferromagnetic domains by using a phase-sensitive technique.

Appendix A

Magnetic moment of 3d transition metals

Magnetic properties of 3d transition metals, Fe, Co, and Ni, and alloys containing them have been one of the central target in magnetism study. This is because ferromagnetism at room temperature is shown only in Fe, Co and Ni and they have a sizable magnetic moment at room temperature. Curie temperature, spin and orbital magnetic moment for Fe, Co and Ni are shown in Table A.1.

TABLE A.1: The Curie temperature (T_C) [202], number of 3d electrons (n_{3d}) [96, 255, 256], spin magnetic moment ($m_{\text{spin}}^{\text{eff}}$), ($m_{\text{spin}}^{\text{eff}}$), orbital magnetic moment (m_{orb}) and its ratio ($m_{\text{orb}}/m_{\text{spin}}^{\text{eff}}$) [96, 179]. The values of magnetic moment are experimentally determined.

Element	Curie T_C [K]	n_{3d}	$m_{\text{spin}}^{\text{eff}}$	m_{orb}	$m_{\text{orb}}/m_{\text{spin}}^{\text{eff}}$
Fe (bcc)	1043	6.61	1.98	0.086	0.043
Co (hcp)	1388	7.51	1.55	0.153	0.099
Ni (fcc)	631	8.55	0.6	0.06	0.1

Magneto-optical effect can be observed in the system with spin-orbit (Δ_{SO}) and exchange interaction (Δ_{EX}). Spin-orbit splitting between $2p_{3/2}$ and $2p_{1/2}$ is $\Delta_{\text{SO}} \sim 13\text{--}16$ eV [257]. Δ_{SO} for $3p$ edge is one tenth as large as that of $2p$ edge. Exchange splitting for $2p$ states is $\Delta_{\text{EX}} \sim 0.3\text{--}0.9$ eV [63] and for $3p$ states is ~ 1 eV [258–261]. Exchange splitting for 3d valence states is $\Delta_{\text{EX}} \sim 1\text{--}2$ eV [257].

Appendix B

Experimental methods

B.1 RHEED

Reflection high energy electron diffraction (RHEED) is technique for probing the process of film growth around sample surface *in situ*. A high energy electron beam is utilized for this measurements and the wavelength of a electron can be expressed using de Broglie formula as,

$$\lambda[\text{\AA}] = \frac{h}{p} = \frac{h}{2meV} = \sqrt{\frac{150.412}{V}} \quad (\text{B.1})$$

where h is Plank constant, p is electron momentum, m is electron mass, e is an elementary charge and V is acceleration voltage for electrons. Depending on the electron energy, measurement schemes vary: transmission electron diffraction for 100 keV \sim 1 MeV, RHEED (forward scattering) for 10 \sim 100 keV and lo-energy electron diffraction (back scattering) for \sim 100 eV. For RHEED, the wavelength is $\lambda = 0.1 \text{ \AA}$ for 15 keV, which is one tenth of that of typical hard X-ray. Therefore, in order to measure clear forward-scattering diffraction spots or streaks, a high-energy electron beam should incident on the sample with grazing angle $\sim 1\text{--}3^\circ$. Due to this setup using grazing angle, this technique is often combined with molecular beam epitaxy and enables one to observe surface properties such as reconstruction periodicities, surface orientation and lateral lattice parameter of sample during film growth.

The intensity of diffraction wave can be written as,

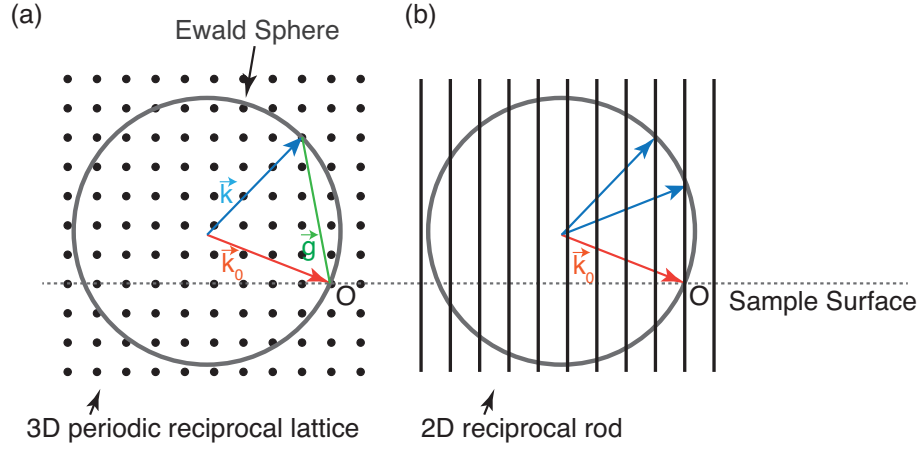


FIGURE B.1: Schematic diagram of construction of Ewald sphere in (a) three dimensional and (b) two dimensional reciprocal space. θ is grazing angle of electron beam on sample.

$$I(\vec{g}) = I_0 \frac{1}{r^2} |f_{unit}(\vec{g})|^2 |L(\vec{g})|^2 \quad (\text{B.2})$$

where $f_{unit}(\vec{g})$ is a crystal structure factor and $L(\vec{g})$ is Laue function. This expression is obtained in the framework of Born approximation, or kinematic theory of diffraction which does not consider multiple scattering.

There are several factors that keep in mind in analyzing RHEED data.

- Laue (Bragg) condition: when the following relation is met, Laue function has sharp maximum. \vec{g} is scattering vector, \vec{a} , \vec{b} , \vec{c} is unit lattice vector in three dimensional real space and h , k , and l is an integer.

$$\vec{g} \cdot \vec{a} = h, \quad \vec{g} \cdot \vec{b} = k, \quad \vec{g} \cdot \vec{c} = l \quad (\text{B.3})$$

This is satisfied when the scattering vector \vec{g} is expressed as

$$\vec{g} = h\vec{a}^* + k\vec{b}^* + l\vec{c}^* \quad (\text{B.4})$$

- Elastic Scattering: Considering only elastic scattering, the wavevector (\vec{k}) of the diffracted wave has the same magnitude as that (\vec{k}_0) of the incident wave.

$$|\vec{k}_0| = |\vec{k}| \quad (\text{B.5})$$

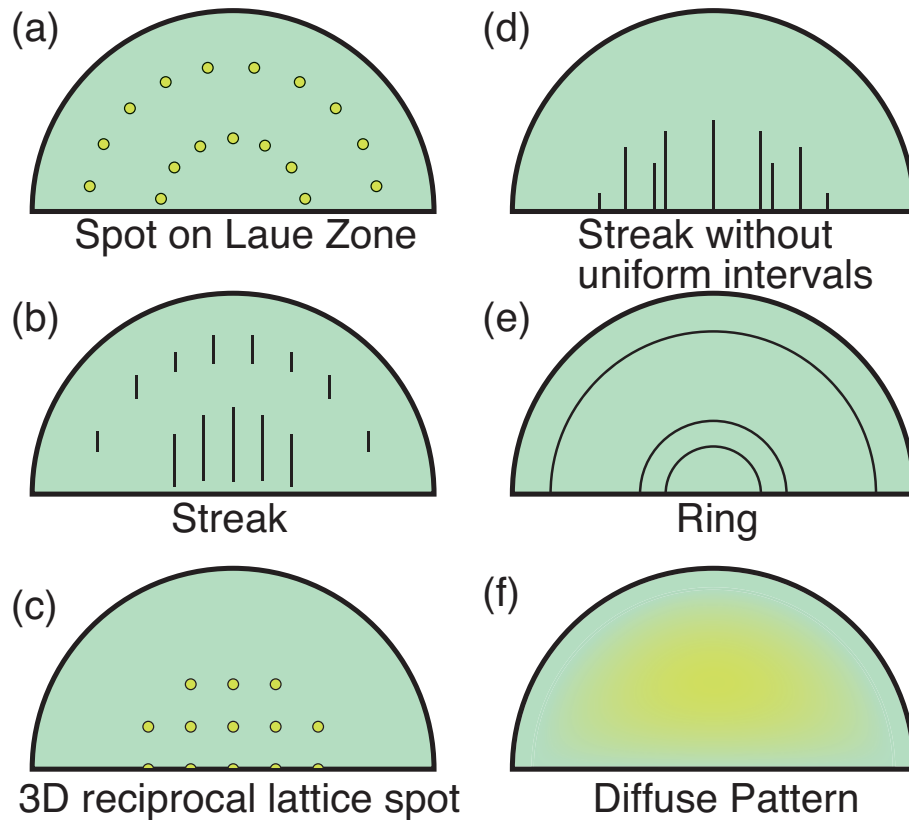


FIGURE B.2: Typical RHEED pattern for a) Surface with complete flatness and periodicity, b) Surface with in-plane coherent length smaller than that in a), d) Surface with nanometer-sized islands, d) Rotationally disordered surface, e) Polycrystal. Each of the RHEED pattern and f) amorphous.

- Ewald sphere: Ewald sphere construction is an intuitive method for showing diffracted condition. A sphere of radius $1/\lambda$ ($=-\vec{k}_0=-\vec{k}$) is drawn with its origin at the tail end of k_0 in reciprocal space with its origin at the head end of k_0 . Then, the diffracted point appears where the sphere and the reciprocal lattice point intersect B.1(a). Equations B.4 and B.5 are satisfied under this Ewald Sphere.
- Extinction rule: Crystal structure factor becomes zero when (hkl) takes a certain combination value, which vary depending on the crystal structure.
- Effect of inelastic scattering and multiple scattering: One of effect of the inelastic scattering is Kikuchi line/band that is a distinct features showing specific crystal orientation and the flatness of the surface.

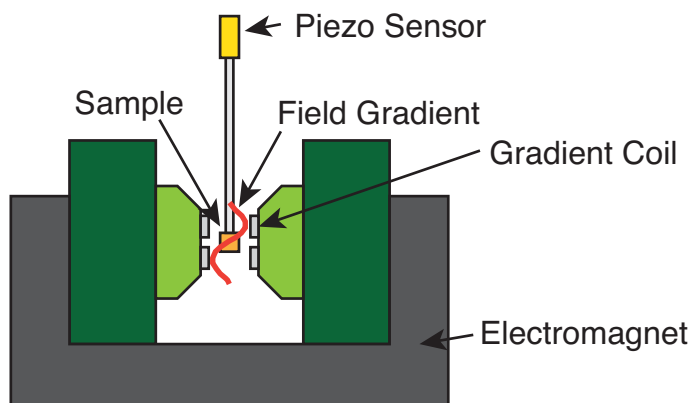


FIGURE B.3: Schematic diagram of an alternating gradient magnetometer.

- Reciprocal lattice rod: Reciprocal lattice of two dimensional surface corresponds to rod normal to surface. In this case, shown in Fig. B.1(b)

Depending on the surface structure, RHEED pattern can be categorized as the following: a) Surface with complete flatness and periodicity, b) Surface with in-plane coherent length smaller than that in a), d) Surface with nanometer-sized islands, d) Rotationally disordered surface, e) Polycrystal. Each of the RHEED pattern and f) amorphous in Fig. B.2.

B.2 Alternating gradient magnetometer

Alternating Gradient Magnetometer (AGM, MicroMag 2900, Princeton Measurements Co.) can be used for measuring hysteresis curve with absolute magnetization values under applying magnetic field either parallel or perpendicular to sample surface. Magnetic coils attached on the poles of electromagnet generate field-gradient and it gives force parallel to the field-gradient on a sample shown in Fig. B.3. The force is measured with piezoelectric sensor. AC field generated by the coils modulates field-gradient periodically and the sample vibrates with a certain amount of amplitude that is proportional to magnetic moment. The sensitivity of this method is enhanced by setting AC-field frequency around the resonance of sample holder. The advantage of this method is high sensitivity (a few μemu) and the measurement speed compared to vibrating sample magnetometer (VSM) which is also employed for measuring magnetization curve. Basically, piezoelectric sensor detects force so that the signals is affected

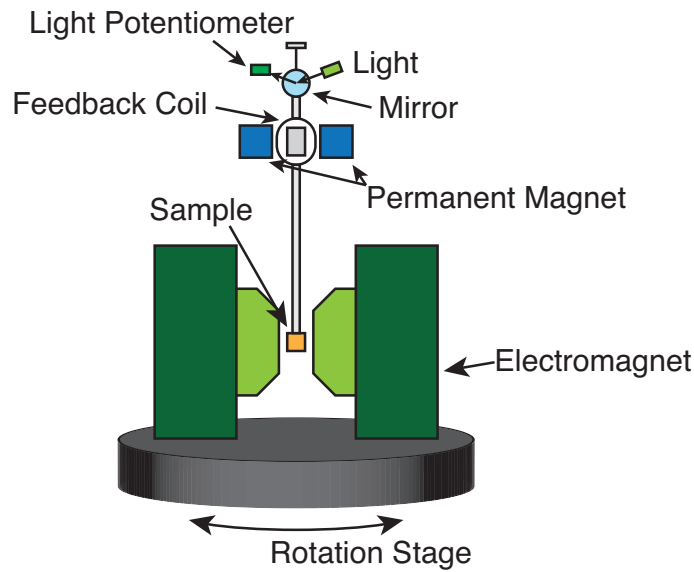


FIGURE B.4: Schematic diagram of a torque magnetometer.

by air-vibration, sample position with respect to sample holder, and tiny dust on sample holder.

B.3 Torque Magnetometer

Torque magnetometer is suitable for measuring magnetic anisotropy. In this thesis, this method was employed for evaluating perpendicular magnetic anisotropy (PMA) of MgO/Fe/Au and Au/Fe/Au films in Sec. ???. PMA can also be measured from difference between in-plane and out-of-plane magnetization curve, however torque magnetometer can directly determine PMA energy and has high sensitivity to magnetic anisotropy than other methods for measuring it.

In this measurement, magnetic field is applied to a sample using electromagnetic (EM) coil and reaches to saturation magnetization. The sample is sandwiched by the two magnetic poles. When the magnetic field is applied in some direction which is not parallel to the easy magnetization axis of sample, torque is generated for rotating the sample so that the direction of external field coincide with the easy axis (Fig. B.4). Torque magnetometer (TRT-2, Toei Inductory Co., Ltd) measures magnetic-field-direction dependence of torque during rotation of electromagnetic coil under magnetic field application with constant magnitude, 15 kOe. Torque can be expressed as,

$$T(\theta) = -\frac{\partial E(\theta)}{\partial \theta} \quad (\text{B.6})$$

, in which E is anisotropy energy. Effective PMA energy that includes shape anisotropy can be expressed,

$$E_{\text{eff}} = K_{\text{eff}} \sin^2 \theta \quad (\text{B.7})$$

Then, torque, $T(\theta)$, becomes

$$T(\theta) = -K_{\text{eff}} \sin 2\theta \quad (\text{B.8})$$

Therefore, torque curve obtained by rotating EM coil 360° is sine curve with two oscillation and amplitude corresponds to the effective anisotropy energy.

Appendix C

Configuration-interaction cluster-model calculation

In this section, calculations used in Sec. 4.4.2 are described [262–264].

We select a central Ni atom with appropriate linear combinations of $3d$ orbitals on neighboring Ni atomic sites to serve as a reservoir of holes denoted by L. The ground state $|g\rangle$ of the system is described by a linear combination of three configurations: $3d^8$, $3d^9\bar{L}$, and $3d^{10}\bar{L}^2$. For the ground state, we used parameters similar to those in [264]: charge transfer energy (Δ) = -0.75 eV, on-site Coulomb interaction between $3d$ states (U_{dd})=1.5 eV, core-hole potential (U_{dc})=2.5 eV, and hybridization energy (V)=1.6 eV. The Slater integrals (Racah parameter) for evaluating the parameters are calculated with the Hartree-Fock method [262–264] and rescaled by 80 %.

The X-ray scattering cross section generally can be divided into a non-resonance term (Thomson scattering) and resonance term (anomalous scattering). Conventional X-ray diffraction and X-ray scattering with non-resonant condition can be described mainly by Thomson scattering. However, at or near resonance for a specific absorption edge, the scattering cross section is dominated by the anomalous term, which is a second-order optical process described by the Kramers-Heisenberg formula. Thus, soft X-ray MOKE at the resonance condition must also be described by this second-order optical process. Furthermore, it is well known that in XAS and photoemission at the M -edge for $3d$ transition metal systems, the final state cannot be described simply by a $3p$ hole configuration because of super Coster-Kronig Auger decay and Fano interference. For quantitative analysis of resonant X-ray MOKE at the M -edge region of transition metal systems, we have to take into account all the above contributions. The present

MOKE calculation based on the Kramers-Heisenberg formula was carried out with the transition probability given by [262–264]

$$F(h\nu_{out}, h\nu_{in}) = \sum_f \left| \langle f | V_R \frac{1}{E_g + h\nu_{in} - H_0 + i\hat{\Gamma}} (V_R - i\pi\rho V_A V_R) | g \rangle \right|^2 \times \delta(E_g + h\nu_{in} - E_f - h\nu_{out}) \quad (C.1)$$

where V_R and V_A represent the electric dipole excitation and the Auger decay, respectively, $\hat{\Gamma}$ is a lifetime operator in the intermediate state, ρ is the density of states of the photoionization continuum, $h\nu_{in}$ and $h\nu_{out}$ are the incident and emitted photon energies, and E_g and E_f are the energies of $|g\rangle$ and $|f\rangle$, respectively. The calculation takes into account the Fano interference between the $3p \rightarrow 3d$ and $3d \rightarrow \varepsilon_f$ transitions through the $3p - 3d3d$ super Coster-Kronig transition. The lifetime $\hat{\Gamma}$ in the intermediate state, $|i\rangle$, has been taken as the multiplet-term-dependent lifetime from the Auger decay:

$$\Gamma = \pi \sum_n | \langle A | \frac{1}{r} | i \rangle |^2 \delta(E_A - E_i) \quad (C.2)$$

In the formula, $|A\rangle$ corresponds to the configuration of $3d^{n-1}\varepsilon_f$, where ε_f is a continuum photoelectron state and $1/r$ represents the Coulomb potential where r is the distance between particles. To our knowledge, no theoretical calculations have been reported for the RMOKE with the Fano effect and multiplet term-dependent lifetime.

For p -polarization in the polar RMOKE geometry, the complex Kerr angle is defined by

$$\theta_k + i\eta_k = -r_{sp}/r_{pp} \quad (C.3)$$

where θ_k and η_k are the Kerr rotation angle and ellipticity, respectively, and r_{sp} and r_{pp} are defined as:

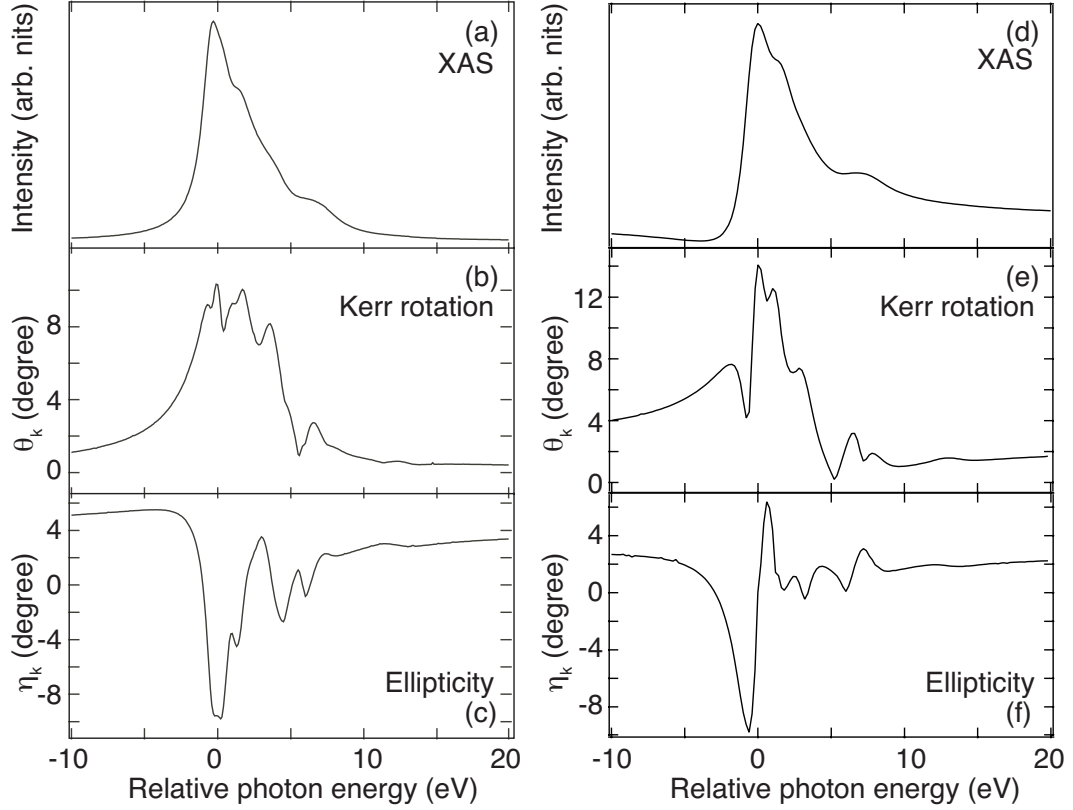


FIGURE C.1: (a) X-ray absorption spectrum (XAS), (b) Kerr rotation (θ_k), and (c) Ellipticity (η_k) of the Ni crystal at the saturated magnetization, calculated with the cluster model. (d) X-ray absorption spectrum (XAS), (e) Kerr rotation (θ_k), and (f) Ellipticity (η_k) of the Ni crystal at the saturated magnetization, calculated with the same manner as the (a), (b) and (c). For comparison, the calculations in (a), (b) and (c) were made *without* the Fano effect, while those in (d), (e) and (f) were done *with* the Fano effect.

$$r_{sp} = E_s^r/E_p^i \quad (\text{C.4})$$

$$r_{pp} = E_p^r/E_p^i. \quad (\text{C.5})$$

Fig. C.1(a)-(c) shows the XAS, Kerr, and ellipticity spectra for the CI model without Fano interference, while Fig. C.1(d)-(f) shows them taking into account the Fano effect. In both cases, at the absorption edge, θ_k is as large as 10° , indicating a large MOKE. Contribution of the Fano interference can be found in the pre-edge energy region. For example, the Kerr rotation angle is large and has sharp photon energy dependence with

the Fano effect in Fig. C.1(d), while it is small and dull without the Fano effect in Fig. C.1(b).

Finally, we show calculated results compared with experimental values in Fig. C.2. In the left figure (a), the Fano effect was not included in the calculation, while in the right figure (b), it was taken into account.

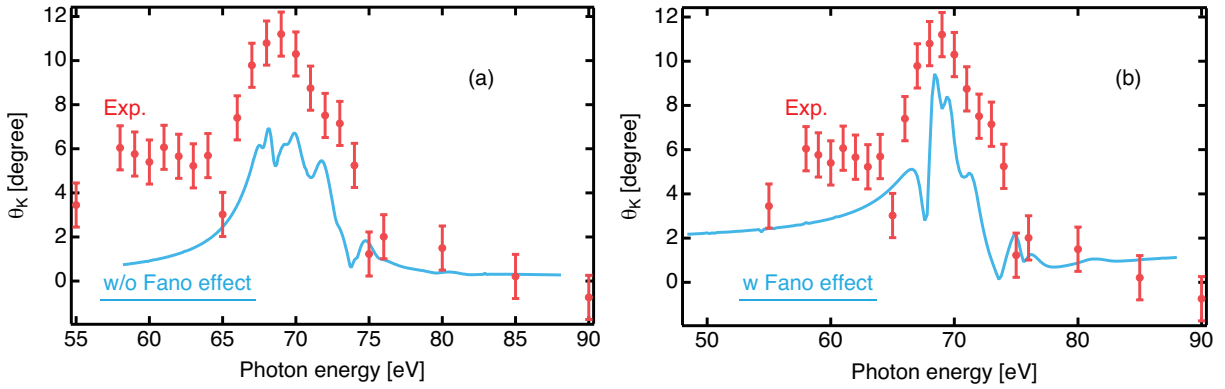


FIGURE C.2: Compare the calculation with experimental results. Fano effect was not included in the calculation for (a) and was taken into account for (b). The calculated Kerr rotation angles in Fig. C.1(b) and (e) are reduced to 67 % to compensate the difference of total magnetic moment, determined with XMCD (Fig. 4.9).

Appendix D

Time-resolved resonant MOKE measurement system using a HHG laser

We extended our resonant MOKE (RMOKE) measurement systems using a high harmonic generation (HHG) laser, presented in Sec. 5.4, into time-resolved regime. Figure D.1 shows the TR-RMOKE system using HHG laser.

At beam splitter the beam is separated to reflected light (89 %) for probe and transmitted light (11 %) for pump pulse (FABS-800-R89-0-UF-1008, LEO Inc.). Delay stage is used for making time-delay between pump and probe pulse (Sigma Tech Inc.). The focal length of lens behind delay stage is determined so that the diameter of pump laser at sample position is ~ 1 mm. Assuming that the pump pulse energy is 0.33 mJ/pulse, the fluence at sample position is ~ 40 mJ/cm². This value is enough for demagnetizing or reversing magnetization. Depending on the experiments, the pump power can be attenuated using $\lambda/2$ wave plate (2-CPW-Z0-L/2-0800, Altechna Inc.) and thin film polarizer (2-BFP-0800-A-2040, Altechna Inc.) by rotating the wave plate. The pump pulse is incident on thin film polarizer with 56° (from surface normal), which is the Brewster angle of this film.

Spatial overlap between pump and probe pulse is confirmed by using fluorescent plate on sample holder. Temporal overlap between pump and probe pulse is first determined using photodiode which is located in front of the electromagnetic coil chamber within ± 50 ps (this corresponds to ± 15 mm of optical path length). Then, accurate overlapping

with tens of femtoseconds time resolution is defined by phenomena of demagnetization or magnetization reversal on target sample.

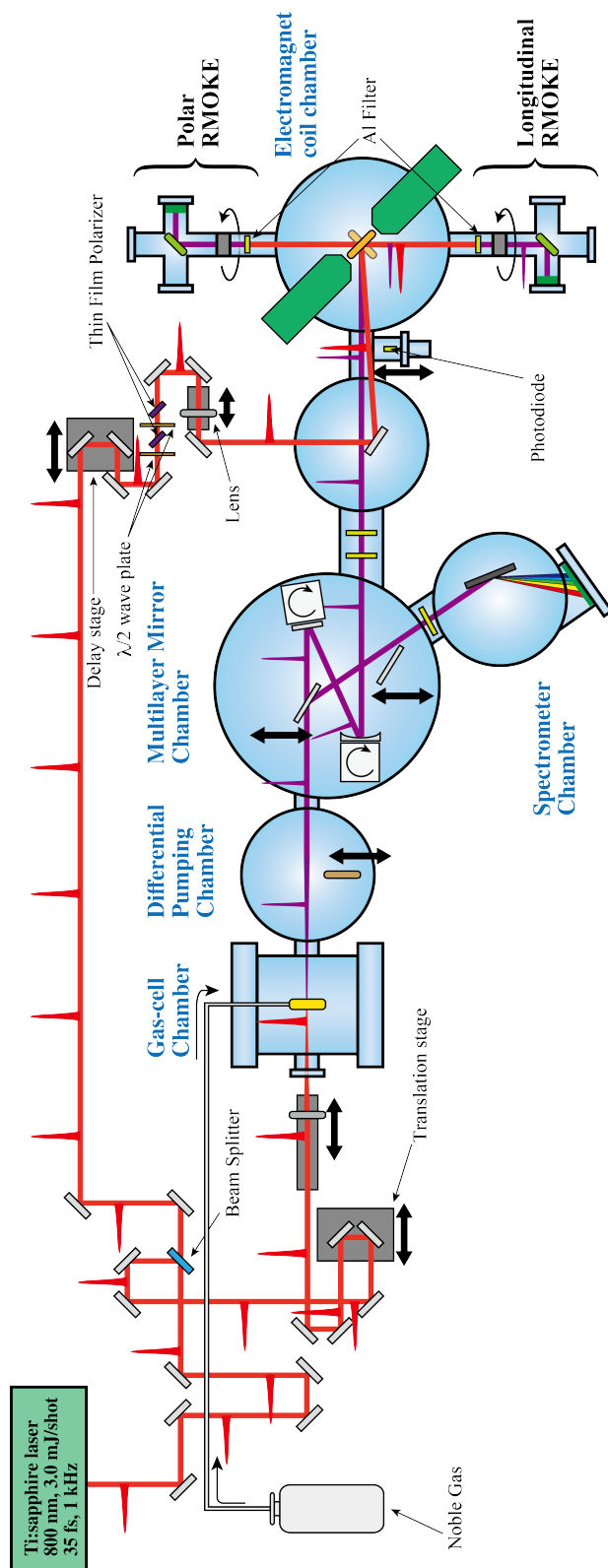


FIGURE D.1: Schematic diagram of TR-RMOKE measurement system using HHG laser. Photodiode is used for overlapping between pump and probe pulses within ± 50 ps. The lens located behind delay stage on the pump beam line has 750 mm focal length.

Publications

Publications included in this thesis

- 1. Ultrafast spin dynamics of out-of-plane magnetization of ultrathin iron film**
Sh. Yamamoto, K. Yamamoto, Y. Hirata, N. Pontius, C. Schüßler-Langeheine, S. Yamamoto, T. Kato, D. Oshima, S. Iwata, H. Wadati, and I. Matsuda
to be submitted for publication
- 2. Ultrafast demagnetization and relaxation of in-plane magnetization of ultrathin iron film**
Sh. Yamamoto, K. Yamamoto, Y. Hirata, N. Pontius, C. Schüßler-Langeheine, S. Yamamoto, T. Kato, D. Oshima, S. Iwata, H. Wadati, and I. Matsuda
to be submitted for publication
- 3. Femtosecond resonant magneto-optical Kerr effect measurement on an ultrathin magnetic film at a soft X-ray free electron laser**
Sh. Yamamoto, Y. Kubota, K. Yamamoto, Y. Takahashi, K. Maruyama, Y. Suzuki, R. Hobara, M. Fujisawa, D. Oshima, S. Owada, T. Togashi, K. Tono, M. Yabashi, Y. Hirata, S. Yamamoto, M. Kotsugi, H. Wadati, T. Kato, S. Iwata, S. Shin, and I. Matsuda
submitted
- 4. Study of element selectivity in SHG of GaFeO₃ by soft X-ray free electron laser**
Sh. Yamamoto, T. Omi, H. Akai, Y. Kubota, Y. Takahashi, Y. Suzuki, Y. Hirata, K. Yamamoto, R. Yukawa, K. Horiba, H. Yumoto, T. Koyama, H. Ohashi, S. Owada, K. Tono, M. Yabashi, E. Shigemasa, S. Yamamoto, M. Kotsugi, H. Wadati, H. Kumigashira, T. Arima, S. Shin, and I. Matsuda
Phys. Rev. Lett. **120**, 223902 (2018).

5. **Resonant magneto-optical Kerr effect measurement system using a high harmonic generation laser**

Sh. Yamamoto, D. Oumbarek, M. Fujisawa, T. Someya, Y. Takahashi, T. Yamamoto, N. Ishii, K. Yaji, S. Yamamoto, T. Kanai, K. Okazaki, M. Kotsugi, J. Itatani, S. Shin, and I. Matsuda

J. Electron. Spectrosc. Relat. Phenom. **222**, 68-73 (2018).

6. **Measurement of resonant magneto-optical Kerr effect using a free electron laser**

Sh. Yamamoto, and I. Matsuda

Appl. Sci. **7**, 662 (2017).

7. **Ultrafast spin-switching of a ferrimagnetic alloy at room temperature traced by resonant magneto-optical Kerr effect using a seeded free electron laser**

Sh. Yamamoto, M. Taguchi, T. Somaya, Y. Kubota, S. Ito, H. Wadati, M. Fujisawa, F. Capotondi, E. Pedersoli, M. Manfredda, L. Raimondi, M. Kiskinova, J. Fujii, P. Moras, T. Tsuyama, T. Nakamura, T. Kato, T. Higashide, S. Iwata, S. Yamamoto, S. Shin, and I. Matsuda

Rev. Sci. Instrum. **86**, 083901 (2015).

8. **Observing of a giant Kerr rotation in a ferromagnetic transition metal by *M*-edge resonant magneto-optic Kerr effect**

Sh. Yamamoto, M. Taguchi, M. Fujisawa, R. Hobara, S. Yamamoto, K. Yaji, T. Nakamura, K. Fujikawa, R. Yukawa, T. Togashi, M. Yabashi, M. Tsunoda, S. Shin, and I. Matsuda

Phys. Rev. B **89**, 064423 (2014).

Bibliography

- [1] Y. Kajiwara, K. Harii, S. Takahashi, J. Ohe, K. Uchida, M. Mizuguchi, H. Umezawa, H. Kawai, K. Ando, K. Takanashi, et al., *Nature* **464**, 262 (2010).
- [2] N. Setter, D. Damjanovic, L. Eng, G. Fox, S. Gevorgian, S. Hong, A. Kingon, H. Kohlstedt, N. Park, G. Stephenson, et al., *J. Appl. Phys.* **100**, 051606 (2006).
- [3] M. Mochizuki, X. Yu, S. Seki, N. Kanazawa, W. Koshibae, J. Zang, M. Mostovoy, Y. Tokura, and N. Nagaosa, *Nat. Mater.* **13**, 241 (2014).
- [4] L. Bogani and W. Wernsdorfer, *Nat. Mater.* **7**, 179 (2008).
- [5] F. Donati, S. Rusponi, S. Stepanow, C. Wäckerlin, A. Singha, L. Persichetti, R. Baltic, K. Diller, F. Patthey, E. Fernandes, et al., *Science* **352**, 318 (2016).
- [6] M. Albert, M. Franchin, T. Fischbacher, G. Meier, and H. Fangohr, *J. Phys.: Condens. Matter* **24**, 024219 (2011).
- [7] K. Carva, *Nat. Phys.* **10**, 552 (2014).
- [8] S. Yamamoto and I. Matsuda, *Appl. Sci.* **7**, 662 (2017).
- [9] J.-Y. Bigot, M. Vomir, and E. Beaurepaire, *Nat. Phys.* **5**, 515 (2009).
- [10] E. Beaurepaire, J.-C. Merle, A. Daunois, and J.-Y. Bigot, *Phys. Rev. Lett.* **76**, 4250 (1996).
- [11] A. Kirilyuk, A. V. Kimel, and T. Rasing, *Rev. Mod. Phys.* **82**, 2731 (2010).
- [12] F. Hellman, A. Hoffmann, Y. Tserkovnyak, G. S. Beach, E. E. Fullerton, C. Leighton, A. H. MacDonald, D. C. Ralph, D. A. Arena, H. A. Dürr, et al., *Rev. Mod. Phys.* **89**, 025006 (2017).
- [13] E. Carpene, E. Mancini, C. Dallera, M. Brenna, E. Puppini, and S. De Silvestri, *Phys. Rev. B* **78**, 174422 (2008).

- [14] G. Zhang, W. Hübner, G. Lefkidis, Y. Bai, and T. F. George, *Nat. Phys.* **5**, 499 (2009).
- [15] D. Rudolf, L.-O. Chan, M. Battiato, R. Adam, J. M. Shaw, E. Turgut, P. Maldonado, S. Mathias, P. Grychtol, H. T. Nembach, et al., *Nat. Commun.* **3**, 1037 (2012).
- [16] T. Nozaki, Y. Shiota, S. Miwa, S. Murakami, F. Bonell, S. Ishibashi, H. Kubota, K. Yakushiji, T. Saruya, A. Fukushima, et al., *Nat. Phys.* **8**, 491 (2012).
- [17] J. Milano, L. Steren, and M. Grimsditch, *Phys. Rev. Lett.* **93**, 077601 (2004).
- [18] M. Hangyo, M. Tani, and T. Nagashima, *Int. J. Infrared Millimeter Waves* **26**, 1661 (2005).
- [19] S. Parchenko, T. Satoh, I. Yoshimine, F. Stobiecki, A. Maziewski, and A. Stupakiewicz, *Appl. Phys. Lett.* **108**, 032404 (2016).
- [20] A. Khorsand, M. Savoini, A. Kirilyuk, A. Kimel, A. Tsukamoto, A. Itoh, and T. Rasing, *Phys. Rev. Lett.* **110**, 107205 (2013).
- [21] Y. Ogawa, Y. Kaneko, J. He, X. Yu, T. Arima, and Y. Tokura, *Phys. Rev. Lett.* **92**, 047401 (2004).
- [22] H. Regensburger, R. Vollmer, and J. Kirschner, *Phys. Rev. B* **61**, 14716 (2000).
- [23] H. Höchst, D. Rioux, D. Zhao, and D. L. Huber, *J Appl. Phys.* **81**, 7584 (1997).
- [24] H.-C. Mertins, P. Oppeneer, J. Kuneš, A. Gaupp, D. Abramssohn, and F. Schäfers, *Phys. Rev. Lett.* **87**, 047401 (2001).
- [25] M. Schwickert, G. Guo, M. Tomaz, W. O'Brien, and G. Harp, *Phys. Rev. B* **58**, R4289 (1998).
- [26] M. Finazzi, L. Duo, and F. Ciccacci, *Surf. Sci. Rep.* **64**, 139 (2009).
- [27] O. Kfir, P. Grychtol, E. Turgut, R. Knut, D. Zusin, D. Popmintchev, T. Popmintchev, H. Nembach, J. M. Shaw, A. Fleischer, et al., *Nat. Photon.* **9**, 99 (2015).
- [28] T. Fan, P. Grychtol, R. Knut, C. Hernández-García, D. D. Hickstein, D. Zusin, C. Gentry, F. J. Dollar, C. A. Mancuso, C. W. Hogle, et al., *Proc. Natl. Acad. Sci. U.S.A.* **112**, 14206 (2015).

-
- [29] G. Lambert, B. Vodungbo, J. Gautier, B. Mahieu, V. Malka, S. Sebban, P. Zeitoun, J. Luning, J. Perron, A. Andreev, et al., *Nat. Commun.* **6**, 6167 (2015).
- [30] L. J. Ament, M. Van Veenendaal, T. P. Devereaux, J. P. Hill, and J. Van Den Brink, *Rev. Mod. Phys.* **83**, 705 (2011).
- [31] G. Fabbris, D. Meyers, L. Xu, V. Katukuri, L. Hozoi, X. Liu, Z.-Y. Chen, J. Okamoto, T. Schmitt, A. Uldry, et al., *Phys. Rev. Lett.* **118**, 156402 (2017).
- [32] M. Dean, R. Springell, C. Monney, K. Zhou, J. Pereiro, I. Božović, B. Dalla Piazza, H. Rønnow, E. Morenzoni, J. Van Den Brink, et al., *Nat. Mater.* **11**, 850 (2012).
- [33] M. Minola, D. Di Castro, L. Braicovich, N. Brookes, D. Innocenti, M. M. Sala, A. Tebano, G. Balestrino, and G. Ghiringhelli, *Phys. Rev. B* **85**, 235138 (2012).
- [34] L. Müller, C. Gutt, B. Pfau, S. Schaffert, J. Geilhufe, F. Büttner, J. Mohanty, S. Flewett, R. Treusch, S. Düsterer, et al., *Phys. Rev. Lett.* **110**, 234801 (2013).
- [35] Y. Yamasaki, T. Sudayama, J. Okamoto, H. Nakao, M. Kubota, and Y. Murakami, in *J. Phys.: Conf. Ser.* (IOP Publishing, 2013), vol. 425, p. 132012.
- [36] C. M. Günther, E. Guehrs, M. Schneider, B. Pfau, C. von Korff Schmising, J. Geilhufe, S. Schaffert, and S. Eisebitt, *J. Opt.* (2017).
- [37] S. Eisebitt, J. Lüning, W. Schlotter, M. Lörngen, O. Hellwig, W. Eberhardt, and J. Stöhr, *Nature* **432**, 885 (2004).
- [38] A. Tanaka, C. Chang, M. Buchholz, C. Trabant, E. Schierle, J. Schlappa, D. Schmitz, H. Ott, P. Metcalf, L. Tjeng, et al., *Phys. Rev. B* **88**, 195110 (2013).
- [39] L.-O. Chan, M. Siemens, M. M. Murnane, H. C. Kapteyn, S. Mathias, M. Aeschlimann, P. Grychtol, R. Adam, C. M. Schneider, J. M. Shaw, et al., *Phys. Rev. Lett.* **103**, 257402 (2009).
- [40] E. Turgut, J. M. Shaw, P. Grychtol, H. T. Nembach, D. Rudolf, R. Adam, M. Aeschlimann, C. M. Schneider, T. J. Silva, M. M. Murnane, et al., *Phys. Rev. Lett.* **110**, 197201 (2013).
- [41] E. Ferrari, C. Spezzani, F. Fortuna, R. Delaunay, F. Vidal, I. Nikolov, P. Cinquegrana, B. Diviacco, D. Gauthier, G. Penco, et al., in *Photonics* (Multidisciplinary Digital Publishing Institute, 2017), vol. 4, p. 6.

- [42] I. Radu, K. Vahaplar, C. Stamm, T. Kachel, N. Pontius, H. Dürr, T. Ostler, J. Barker, R. Evans, R. Chantrell, et al., *Nature* **472**, 205 (2011).
- [43] C. Stamm, T. Kachel, N. Pontius, R. Mitzner, T. Quast, K. Holldack, S. Khan, C. Lupulescu, E. Aziz, M. Wietstruk, et al., *Nat. Mater.* **6**, 740 (2007).
- [44] F. Willems, C. Smeenk, N. Zhavoronkov, O. Kornilov, I. Radu, M. Schmidbauer, M. Hanke, C. von Korff Schmising, M. Vrakking, and S. Eisebitt, *Phys. Rev. B* **92**, 220405 (2015).
- [45] D. J. Higley, K. Hirsch, G. L. Dakovski, E. Jal, E. Yuan, T. Liu, A. A. Lutman, J. P. MacArthur, E. Arenholz, Z. Chen, et al., *Rev. Sci. Instrum.* **87**, 033110 (2016).
- [46] M. Dean, Y. Cao, X. Liu, S. Wall, D. Zhu, R. Mankowsky, V. Thampy, X. Chen, J. Vale, D. Casa, et al., *Nat. Mater.* **15**, 601 (2016).
- [47] B. Pfau, S. Schaffert, L. Müller, C. Gutt, A. Al-Shemmary, F. Büttner, R. De-launay, S. Düsterer, S. Flewett, R. Frömter, et al., *Nat. Commun.* **3**, 1100 (2012).
- [48] B. Vodungbo, J. Gautier, G. Lambert, A. B. Sardinha, M. Lozano, S. Sebban, M. Ducouso, W. Boutu, K. Li, B. Tudu, et al., *Nat. Commun.* **3**, 999 (2012).
- [49] C. Graves, A. Reid, T. Wang, B. Wu, S. De Jong, K. Vahaplar, I. Radu, D. Bernstein, M. Messerschmidt, L. Müller, et al., *Nat. Mater.* **12**, 293 (2013).
- [50] F. Büttner, C. Moutafis, M. Schneider, B. Krüger, C. Günther, J. Geilhufe, C. v. K. Schmising, J. Mohanty, B. Pfau, S. Schaffert, et al., *Nat. Phys.* **11**, 225 (2015).
- [51] N. Bukin, C. McKeever, E. Burgos-Parra, P. Keatley, R. Hicken, F. Ogrin, G. Beutier, M. Dupraz, H. Popescu, N. Jaouen, et al., *Sci. Rep.* **6** (2016).
- [52] C. von Korff Schmising, B. Pfau, M. Schneider, C. Günther, M. Giovannella, J. Perron, B. Vodungbo, L. Müller, F. Capotondi, E. Pedersoli, et al., *Phys. Rev. Lett.* **112**, 217203 (2014).
- [53] K. Holldack, N. Pontius, E. Schierle, T. Kachel, V. Soltwisch, R. Mitzner, T. Quast, G. Springholz, and E. Weschke, *Appl. Phys. Lett.* **97**, 062502 (2010).
- [54] N. Pontius, T. Kachel, C. Schüßler-Langeheine, W. Schlotter, M. Beye, F. Sorgenfrei, C. Chang, A. Foehlich, W. Wurth, P. Metcalf, et al., *Appl. Phys. Lett.* **98**, 182504 (2011).

-
- [55] M. Först, A. Caviglia, R. Scherwitzl, R. Mankowsky, P. Zubko, V. Khanna, H. Bromberger, S. Wilkins, Y.-D. Chuang, W. Lee, et al., *Nat. Mater.* **14**, 883 (2015).
- [56] S. Khan, K. Holldack, T. Kachel, R. Mitzner, and T. Quast, *Phys. Rev. Lett.* **97**, 074801 (2006).
- [57] K. Holldack, J. Bahrtdt, A. Balzer, U. Bovensiepen, M. Brzhezinskaya, A. Erko, A. Eschenlohr, R. Follath, A. Firsov, W. Frentrup, et al., *J. Synchrot. Radiat.* **21**, 1090 (2014).
- [58] T. Tsuyama, S. Chakraverty, S. Macke, N. Pontius, C. Schüßler-Langeheine, H. Hwang, Y. Tokura, and H. Wadati, *Phys. Rev. Lett.* **116**, 256402 (2016).
- [59] B. L. Henke, E. Gullikson, and J. C. Davis, *At. Data Nucl. Data Tables* **54**, 181 (1993).
- [60] K. Takubo, K. Yamamoto, Y. Hirata, Y. Yokoyama, Y. Kubota, S. Yamamoto, S. Yamamoto, I. Matsuda, S. Shin, T. Seki, et al., *Appl Phys. Lett.* **110**, 162401 (2017).
- [61] T. Miyahara, S.-Y. Park, T. Hanyu, T. Hatano, S. Moto, and Y. Kagoshima, *Rev. Sci. Instrum.* **66**, 1558 (1995).
- [62] J. Erskine and E. Stern, *Phys. Rev. B* **8**, 1239 (1973).
- [63] J. Kuneš and P. M. Oppeneer, *Phys. Rev. B* **67**, 024431 (2003).
- [64] E. Allaria, B. Diviacco, C. Callegari, P. Finetti, B. Mahieu, J. Viefhaus, M. Zangrando, G. De Ninno, G. Lambert, E. Ferrari, et al., *Phys. Rev. X* **4**, 041040 (2014).
- [65] E. Roussel, E. Allaria, C. Callegari, M. Coreno, R. Cucini, S. D. Mitri, B. Diviacco, E. Ferrari, P. Finetti, D. Gauthier, et al., in *Photonics* (Multidisciplinary Digital Publishing Institute, 2017), vol. 4, p. 29.
- [66] A. A. Lutman, J. P. MacArthur, M. Ilchen, A. O. Lindahl, J. Buck, R. N. Coffee, G. L. Dakovski, L. Dammann, Y. Ding, H. A. Dürr, et al., *Nat. Photon.* **10**, 468 (2016).
- [67] B. Vodungbo, A. B. Sardinha, J. Gautier, G. Lambert, C. Valentin, M. Lozano, G. Iaquaniello, F. Delmotte, S. Sebban, J. Lüning, et al., *Opt. Express* **19**, 4346 (2011).

- [68] P. Oppeneer, Handbook of Magnetic Materials **13**, 229 (2001).
- [69] T. Rasing, M. G. Koerkamp, B. Koopmans, and H. v. Berg, J. Appl. Phys. **79**, 6181 (1996).
- [70] Z. Qiu and S. D. Bader, J. Magn. Magn. Mater. **200**, 664 (1999).
- [71] Z. Yang and M. Scheinfein, J. Appl. Phys. **74**, 6810 (1993).
- [72] Y. M. Strelhniker and D. J. Bergman, in *Proc. of SPIE* (International Society for Optics and Photonics, 2015), pp. 954705–954705.
- [73] R. Kubo, Can. J. Phys. **34**, 1274 (1956).
- [74] R. Kubo, J. Phys. Soc. Jpn. **12**, 570 (1957).
- [75] P. Bruno, Y. Suzuki, and C. Chappert, Phys. Rev. B **53**, 9214 (1996).
- [76] G. Krinchik and V. Artem'ev, Sov. Phys. JETP **26**, 1080 (1968).
- [77] Š. Višňovský, R. Krishnan, M. Nývlt, and V. Prosser, J. Magn. Soc. Jpn. **20**, 41 (1996).
- [78] P. Oppeneer, T. Maurer, J. Sticht, and J. Kübler, Phys. Rev. B **45**, 10924 (1992).
- [79] D. Weller, G. Harp, R. Farrow, A. Cebollada, and J. Sticht, Phys. Rev. Lett. **72**, 2097 (1994).
- [80] P. Oppeneer, T. Kraft, and H. Eschrig, Phys. Rev. B **52**, 3577 (1995).
- [81] Y. Kudryavtsev and I. Lezhnenko, Sov. Phys. Solid State, **23**, 249 (1981).
- [82] T. Suzuki, D. Weller, C.-A. Chang, R. Savoy, T. Huang, B. Gurney, and V. Speriosu, Appl. Phys. Lett. **64**, 2736 (1994).
- [83] P. Van Engen, K. Buschow, and M. Erman, J. Magn. Magn. Mater. **30**, 374 (1983).
- [84] Š. Višňovský, V. Pařízek, M. Nývlt, P. Kielar, V. Prosser, and R. Krishnan, J. Magn. Magn. Mater. **127**, 135 (1993).
- [85] G. Di and S. Uchiyama, J. Appl. Phys. **75**, 4270 (1994).
- [86] J. Stöhr and H. C. Siegmann, *Magnetism: from fundamentals to nanoscale dynamics*, vol. 152 (Springer Science & Business Media, 2007).

-
- [87] P. Grychtol, *Element-selective and time-resolved magnetic investigations in the extreme ultraviolet range* (Forschungszentrum, Zentralbibliothek, 2011).
- [88] J. Erskine and E. Stern, Phys. Rev. B **12**, 5016 (1975).
- [89] Y.-R. Shen, *Fundamentals of sum-frequency spectroscopy* (Cambridge University Press, 2016).
- [90] Y. Shen, J. Phys. Chem. C **116**, 15505 (2012).
- [91] M. Fiebig, V. V. Pavlov, and R. V. Pisarev, JOSA B **22**, 96 (2005).
- [92] R. R. Birss et al., *Symmetry and magnetism*, vol. 863 (North-Holland Amsterdam, 1964).
- [93] M. Fiebig, J. Phys. D: Appl. Phys. **38**, R123 (2005).
- [94] B. Thole, P. Carra, F. Sette, and G. van der Laan, Phys. Rev. Lett. **68**, 1943 (1992).
- [95] P. Carra, B. Thole, M. Altarelli, and X. Wang, Phys. Rev. Lett. **70**, 694 (1993).
- [96] C. Chen, Y. Idzerda, H.-J. Lin, N. Smith, G. Meigs, E. Chaban, G. Ho, E. Pellegrin, and F. Sette, Phys. Rev. Lett. **75**, 152 (1995).
- [97] D. Atwood, Principles and Applications (1999).
- [98] P. Emma, R. Akre, J. Arthur, R. Bionta, C. Bostedt, J. Bozek, A. Brachmann, P. Bucksbaum, R. Coffee, F.-J. Decker, et al., Nat. Photon. **4**, 641 (2010).
- [99] R. Bonifacio, C. Pellegrini, and L. Narducci, Opt. Commun. **50**, 373 (1984).
- [100] J. Amann, W. Berg, V. Blank, F.-J. Decker, Y. Ding, P. Emma, Y. Feng, J. Frisch, D. Fritz, J. Hastings, et al., Nat. Photon. **6**, 693 (2012).
- [101] L. H. Yu, Phys. Rev. A **44**, 5178 (1991).
- [102] E. Allaria, A. Battistoni, F. Bencivenga, R. Borghes, C. Callegari, F. Capotondi, D. Castronovo, P. Cinquegrana, D. Cocco, M. Coreno, et al., New J. Phys. **14**, 113009 (2012).
- [103] E. Allaria, R. Appio, L. Badano, W. Barletta, S. Bassanese, S. Biedron, A. Borga, E. Busetto, D. Castronovo, P. Cinquegrana, et al., Nat. Photon. **6**, 699 (2012).

- [104] E. Allaria, D. Castronovo, P. Cinquegrana, P. Craievich, M. Dal Forno, M. Danailov, G. D'Auria, A. Demidovich, G. De Ninno, S. Di Mitri, et al., *Nat. Photon.* **7**, 913 (2013).
- [105] T. Togashi, E. J. Takahashi, K. Midorikawa, M. Aoyama, K. Yamakawa, T. Sato, A. Iwasaki, S. Owada, T. Okino, K. Yamanouchi, et al., *Opt. Exp.* **19**, 317 (2011).
- [106] S. Ackermann, A. Azima, S. Bajt, J. Bödewadt, F. Curbis, H. Dachraoui, H. Delsim-Hashemi, M. Drescher, S. Düsterer, B. Faatz, et al., *Phys. Rev. Lett.* **111**, 114801 (2013).
- [107] J. L. Krause, K. J. Schafer, and K. C. Kulander, *Phys. Rev. Lett.* **68**, 3535 (1992).
- [108] J. . J. Macklin, J. Kmetec, and C. Gordon III, *Phys. Rev. Lett.* **70**, 766 (1993).
- [109] P. Franken, A. Hill, C. Peters, and G. Weinreich, *Phys. Rev. Lett.* **7**, 118 (1961).
- [110] G. New and J. Ward, *Phys. Rev. Lett.* **19**, 556 (1967).
- [111] A. McPherson, G. Gibson, H. Jara, U. Johann, T. S. Luk, I. McIntyre, K. Boyer, and C. K. Rhodes, *JOSA B* **4**, 595 (1987).
- [112] P. B. Corkum, *Phys. Rev. Lett.* **71**, 1994 (1993).
- [113] C. Winterfeldt, C. Spielmann, and G. Gerber, *Rev. Mod. Phys.* **80**, 117 (2008).
- [114] M. Ammosov, N. Delone, and V. Krainov, *Sov. Phys. JETP* **64**, 1191 (1986).
- [115] A. Zholents and M. Zolotarev, *Phys. Rev. Lett.* **76**, 912 (1996).
- [116] R. Schoenlein, S. Chattopadhyay, H. Chong, T. Glover, P. Heimann, C. Shank, A. Zholents, and M. Zolotarev, *Science* **287**, 2237 (2000).
- [117] P. Beaud, S. Johnson, A. Streun, R. Abela, D. Abramsohn, D. Grolimund, F. Krasniqi, T. Schmidt, V. Schlott, and G. Ingold, *Phys. Rev. Lett.* **99**, 174801 (2007).
- [118] P. Prigent, P. Hollander, M. Labat, M. Couprie, J. Marlats, C. Laulhé, J. Luning, T. Moreno, P. Morin, A. Nadji, et al., *J. Phys. Conf. Ser.* **425**, 072022 (2013).
- [119] S. Yamamoto, M. Taguchi, M. Fujisawa, R. Hobara, S. Yamamoto, K. Yaji, T. Nakamura, K. Fujikawa, R. Yukawa, T. Togashi, et al., *Phys. Rev. B* **89**, 064423 (2014).

-
- [120] K. Namikawa, M. Ando, T. Nakajima, and H. Kawata, *J. Phys. Soc. Jpn.* **54**, 4099 (1985).
- [121] F. De Bergevin and M. Brunel, *Acta Crystallogr. Sect. A* **37**, 314 (1981).
- [122] J. Igarashi and K. Hirai, *Phys. Rev. B* **50**, 17820 (1994).
- [123] G. Krinchik and V. Gushchin, *Sov. Phys. JETP* **29**, 984 (1969).
- [124] C. Kao, J. Hastings, E. Johnson, D. Siddons, G. Smith, and G. Prinz, *Phys. Rev. Lett.* **65**, 373 (1990).
- [125] J. Hannon, G. Trammell, M. Blume, and D. Gibbs, *Phys. Rev. Lett.* **61**, 1245 (1988).
- [126] F. Hillebrecht, T. Kinoshita, D. Spanke, J. Dresselhaus, C. Roth, H. Rose, and E. Kisker, *Phys. Rev. Lett.* **75**, 2224 (1995).
- [127] T. Kinoshita, H. B. Rose, C. Roth, D. Spanke, F. U. Hillebrecht, and E. Kisker, *J. Electron. Spectrosc. Relat. Phenom.* **78**, 237 (1996).
- [128] P. Grychtol, R. Adam, A. Kaiser, S. Cramm, D. Bürgler, and C. Schneider, *J. Electron. Spectrosc. Relat. Phenom.* **184**, 287 (2011).
- [129] M. Tesch, M. Gilbert, H.-C. Mertins, D. Bürgler, U. Berges, and C. Schneider, *Appl. Opt.* **52**, 4294 (2013).
- [130] A. Kleibert, V. Senz, J. Bansmann, and P. Oppeneer, *Phys. Rev. B* **72**, 144404 (2005).
- [131] M. Pretorius, J. Friedrich, A. Ranck, M. Schroeder, J. Voss, V. Wedemeier, D. Spanke, D. Knabben, I. Rozhko, H. Ohldag, et al., *Phys. Rev. B* **55**, 14133 (1997).
- [132] M. Hecker, P. M. Oppeneer, S. Valencia, H.-C. Mertins, and C. M. Schneider, *J. Electron. Spectrosc. Relat. Phenom.* **144**, 881 (2005).
- [133] O. Zaharko, P. Oppeneer, H. Grimmer, M. Horisberger, H.-C. Mertins, D. Abramssohn, F. Schäfers, A. Bill, and H.-B. Braun, *Phys. Rev. B* **66**, 134406 (2002).
- [134] D. Knabben, N. Weber, B. Raab, T. Koop, F. Hillebrecht, E. Kisker, and G. Guo, *J. Magn. Magn. Mater.* **190**, 349 (1998).
- [135] H.-C. Mertins, D. Abramssohn, A. Gaupp, F. Schäfers, W. Gudat, O. Zaharko, H. Grimmer, and P. Oppeneer, *Phys. Rev. B* **66**, 184404 (2002).

- [136] V. Senz, A. Kleibert, and J. Bansmann, *Surf. Rev. Lett.* **9**, 913 (2002).
- [137] J. Kortright, S.-K. Kim, E. Fullerton, J. Jiang, and S. Bader, *Nucl. Instr. Meth. Phys. Res. A* **467**, 1396 (2001).
- [138] M. Sacchi, G. Panaccione, J. Vogel, A. Mirone, and G. van der Laan, *Phys. Rev. B* **58**, 3750 (1998).
- [139] F. De Bergevin, M. Brunel, R. Gale, C. Vettier, E. Elkaim, M. Bessière, S. Lefebvre, et al., *Phys. Rev. B* **46**, 10772 (1992).
- [140] S. Valencia, A. Gaupp, W. Gudat, L. Abad, L. Balcells, and B. Martinez, *Appl. Phys. Lett.* **90**, 252509 (2007).
- [141] J. B. Kortright, *J. Electron. Spectrosc. Relat. Phenom.* **189**, 178 (2013).
- [142] D. Siddons, M. Hart, Y. Amemiya, and J. Hastings, *Phys. Rev. Lett.* **64**, 1967 (1990).
- [143] H. Gotsis and P. Strange, *J. Phys.: Condens. Matter* **6**, 1409 (1994).
- [144] J. Kortright, M. Rice, and R. Carr, *Phys. Rev. B* **51**, 10240 (1995).
- [145] M. Freiser, *IEEE Trans. Magn.* **4**, 152 (1968).
- [146] H.-C. Mertins, F. Schäfers, X. Le Cann, A. Gaupp, and W. Gudat, *Phys. Rev. B* **61**, R874 (2000).
- [147] H.-C. Mertins, F. Schäfers, A. Gaupp, W. Gudat, J. Kunes, and P. Oppeneer, *Nucl. Instr. Meth. Phys. Res. A* **467**, 1407 (2001).
- [148] J. Kuneš, P. Oppeneer, H.-C. Mertins, F. Schäfers, A. Gaupp, W. Gudat, and P. Novák, *Phys. Rev. B* **64**, 174417 (2001).
- [149] H.-C. Mertins, O. Zaharko, A. Gaupp, F. Schäfers, D. Abramsohn, and H. Grimmer, *J. Magn. Magn. Mater.* **240**, 451 (2002).
- [150] J. B. Kortright and S.-K. Kim, *Phys. Rev. B* **62**, 12216 (2000).
- [151] S. Collins, *J. Phys.: Condens. Matter* **11**, 1159 (1999).
- [152] K. Saito, M. Igeta, T. Ejima, T. Hatano, and M. Watanabe, *Surf. Rev. Lett.* **9**, 943 (2002).
- [153] T. Hatano, W. Hu, K. Saito, and M. Watanabe, *J. Electron. Spectrosc. Relat. Phenom.* **101**, 287 (1999).

-
- [154] K. Saito, M. Igeta, T. Ejima, T. Hatano, A. Arai, and M. Watanabe, *J. Electron. Spectrosc. Relat. Phenom.* **144**, 757 (2005).
- [155] S. Valencia, A. Gaupp, W. Gudat, H.-C. Mertins, P. Oppeneer, D. Abramssohn, and C. Schneider, *New J. Phys.* **8**, 254 (2006).
- [156] J. Kortright and M. Rice, *Rev. Sci. Instrum.* **67**, 3353 (1996).
- [157] J. Kortright, M. Rice, S.-K. Kim, C. Walton, and T. Warwick, *J. Magn. Magn. Mater.* **191**, 79 (1999).
- [158] H.-C. Mertins, S. Valencia, D. Abramssohn, A. Gaupp, W. Gudat, and P. M. Oppeneer, *Phys. Rev. B* **69**, 064407 (2004).
- [159] S. Valencia, H.-C. Mertins, D. Abramssohn, A. Gaupp, W. Gudat, and P. M. Oppeneer, *Physica B: Condens. Matter* **345**, 189 (2004).
- [160] O. Hellwig, J. Kortright, K. Takano, and E. E. Fullerton, *Phys. Rev. B* **62**, 11694 (2000).
- [161] K.-S. Lee, S.-K. Kim, and J. Kortright, *Appl. Phys. Lett.* **83**, 3764 (2003).
- [162] S.-K. Kim, K.-S. Lee, J. Kortright, and S.-C. Shin, *Appl. Phys. Lett.* **86**, 102502 (2005).
- [163] P. Strange, H. Ebert, J. Staunton, and B. L. Gyorffy, *J. Phys.: Condens. Matter* **1**, 2959 (1989).
- [164] G. Guo, *Phys. Rev. B* **55**, 11619 (1997).
- [165] N. Mainkar, D. A. Browne, and J. Callaway, *Phys. Rev. B* **53**, 3692 (1996).
- [166] H. Gotsis and P. Strange, *Phys. Rev. B* **55**, 12826 (1997).
- [167] H. Gotsis and P. Strange, *J. Magn. Magn. Mater.* **140**, 2171 (1995).
- [168] P. Williams, A. Rose, and C. Wang, *Appl. Opt.* **36**, 6466 (1997).
- [169] D. Aspnes and A. Studna, *Appl. Opt.* **14**, 220 (1975).
- [170] M. Suzuki and T. Hirono, *The Japanese Society for Synchrotron Radiation Research* **19**, 444 (2006).
- [171] CXRO X-Ray Interactions with Matter website, http://henke.lbl.gov/optical_constants/.

- [172] H. Fujiwara, *Spectroscopic ellipsometry: principles and applications* (John Wiley & Sons, 2007).
- [173] F. Schäfers, H.-C. Mertins, A. Gaupp, W. Gudat, M. Mertin, I. Packe, F. Schmolla, S. Di Fonzo, G. Soullié, W. Jark, et al., *Appl. Opt.* **38**, 4074 (1999).
- [174] H. Kimura, T. Hirono, Y. Tamenori, Y. Saitoh, N. Salashchenko, and T. Ishikawa, *J. Electron. Spectrosc. Relat. Phenom.* **144**, 1079 (2005).
- [175] T. Hirono, H. Kimura, T. Muro, Y. Saitoh, and T. Ishikawa, *J. Electron. Spectrosc. Relat. Phenom.* **144**, 1097 (2005).
- [176] T. Hara, K. Shirasawa, M. Takeuchi, T. Seike, Y. Saito, T. Muro, and H. Kitamura, *Nucl. Instr. Meth. Phys. Res. A* **498**, 496 (2003).
- [177] Y. Saitoh, H. Kimura, Y. Suzuki, T. Nakatani, T. Matsushita, T. Muro, T. Miyahara, M. Fujisawa, K. Soda, S. Ueda, et al., *Rev. Sci. Instrum.* **71**, 3254 (2000).
- [178] O. Eriksson, B. Johansson, R. Albers, A. Boring, and M. Brooks, *Phys. Rev. B* **42**, 2707 (1990).
- [179] J. Vogel, G. Panaccione, and M. Sacchi, *Phys. Rev. B* **50**, 7157 (1994).
- [180] H. Burkhard, *Phys. Status Solidi A* **3**, K135 (1970).
- [181] B. Koopmans, M. Van Kampen, J. Kohlhepp, and W. De Jonge, *Phys. Rev. Lett* **85**, 844 (2000).
- [182] P. M. Oppeneer and A. Liebsch, *J. Phys.: Condens. Matter* **16**, 5519 (2004).
- [183] Sh. Yamamoto, M. Taguchi, T. Someya, Y. Kubota, S. Ito, H. Wadati, M. Fujisawa, F. Capotondi, E. Pedersoli, M. Manfredda, et al., *Revi. Sci. Instrum.* **86**, 083901 (2015).
- [184] J. Hohlfeld, T. Gerrits, M. Bilderbeek, T. Rasing, H. Awano, and N. Ohta, *Phys. Rev. B* **65**, 012413 (2001).
- [185] C. Back, R. Allenspach, W. Weber, S. Parkin, D. Weller, E. L. Garwin, and H. Siegmann, *Science* **285**, 864 (1999).
- [186] K. Vahaplar, Ph.D. thesis, Radboud University (2011).
- [187] A. Kimel, A. Kirilyuk, P. Usachev, R. Pisarev, A. Balbashov, and T. Rasing, *Nature* **435**, 655 (2005).

-
- [188] C. Stanciu, F. Hansteen, A. Kimel, A. Kirilyuk, A. Tsukamoto, A. Itoh, and T. Rasing, *Phys. Rev. Lett.* **99**, 047601 (2007).
- [189] C. Stanciu, A. Tsukamoto, A. Kimel, F. Hansteen, A. Kirilyuk, A. Itoh, and T. Rasing, *Phys. Rev. Lett.* **99**, 217204 (2007).
- [190] K. Vahaplar, A. Kalashnikova, A. Kimel, S. Gerlach, D. Hinzke, U. Nowak, R. Chantrell, A. Tsukamoto, A. Itoh, A. Kirilyuk, et al., *Phys. Rev. B* **85**, 104402 (2012).
- [191] T. Ostler, J. Barker, R. Evans, R. Chantrell, U. Atxitia, O. Chubykalo-Fesenko, S. El Moussaoui, L. Le Guyader, E. Mengotti, L. Heyderman, et al., *Nat. Commun.* **3**, 666 (2012).
- [192] C.-H. Lambert, S. Mangin, B. C. S. Varaprasad, Y. Takahashi, M. Hehn, M. Cinchetti, G. Malinowski, K. Hono, Y. Fainman, M. Aeschlimann, et al., *Science* **345**, 1337 (2014).
- [193] F. Hansteen, A. Kimel, A. Kirilyuk, and T. Rasing, *Phys. Rev. Lett.* **95**, 047402 (2005).
- [194] K. Vahaplar, A. Kalashnikova, A. Kimel, D. Hinzke, U. Nowak, R. Chantrell, A. Tsukamoto, A. Itoh, A. Kirilyuk, and T. Rasing, *Phys. Rev. Lett.* **103**, 117201 (2009).
- [195] M. Battiato, K. Carva, and P. M. Oppeneer, *Phys. Rev. Lett.* **105**, 027203 (2010).
- [196] J. Mentink, J. Hellsvik, D. Afanasiev, B. Ivanov, A. Kirilyuk, A. Kimel, O. Eriksson, M. Katsnelson, and T. Rasing, *Phys. Rev. Lett.* **108**, 057202 (2012).
- [197] A. Baral and H. C. Schneider, *Phys. Rev. B* **91**, 100402 (2015).
- [198] S. Wienholdt, D. Hinzke, K. Carva, P. M. Oppeneer, and U. Nowak, *Phys. Rev. B* **88**, 020406 (2013).
- [199] F. Capotondi, E. Pedersoli, N. Mahne, R. Menk, G. Passos, L. Raimondi, C. Svetina, G. Sandrin, M. Zangrando, M. Kiskinova, et al., *Rev. Sci. Instrum.* **84**, 051301 (2013).
- [200] M. B. Danailov, F. Bencivenga, F. Capotondi, F. Casolari, P. Cinquegrana, A. Demidovich, E. Giangrisostomi, M. P. Kiskinova, G. Kurdi, M. Manfredda, et al., *Opt. Express* **22**, 12869 (2014).

- [201] F. Casolari, F. Bencivenga, F. Capotondi, E. Giangrisostomi, M. Manfredda, R. Mincigrucci, E. Pedersoli, E. Principi, C. Masciovecchio, and M. Kiskinova, *Appl. Phys. Lett.* **104**, 191104 (2014).
- [202] J. Stöhr and H. C. Siegmann, *Magnetism*, vol. 5 (Springer, 2006).
- [203] K. Carva, M. Battiato, and P. M. Oppeneer, *Nat. Phys.* **7**, 665 (2011).
- [204] S. Yamamoto, D. Oumbarek, M. Fujisawa, T. Someya, Y. Takahashi, T. Yamamoto, N. Ishii, K. Yaji, S. Yamamoto, T. Kanai, et al., *J. Electron. Spectrosc. Relat. Phenom.* **222**, 68 (2018).
- [205] S. Mathias, C. La-o vorakiat, J. M. Shaw, E. Turgut, P. Grychtol, R. Adam, D. Rudolf, H. T. Nembach, T. J. Silva, M. Aeschlimann, et al., *J. Electron. Spectrosc. Relat. Phenom.* (2013).
- [206] R. Sandberg, D. Raymondson, C. La-O-Vorakiat, A. Paul, K. Raines, J. Miao, M. Murnane, H. Kapteyn, W. Schlotter, et al., *Opt. Lett.* **34**, 1618 (2009).
- [207] R. Adam, P. Grychtol, S. Cramm, and C. Schneider, *J. Electron. Spectrosc. Relat. Phenom.* **184**, 291 (2011).
- [208] E. D. Palik, ed., *Handbook of Optical Constants of Solids* (Elsevier, 1998).
- [209] E. Falcão-Filho, V. Gkortsas, A. Gordon, and F. X. Kärtner, *Opt. Express* **17**, 11217 (2009).
- [210] V.-M. Gkortsas, S. Bhardwaj, E. L. Falcão-Filho, K.-H. Hong, A. Gordon, and F. X. Kärtner, *J. Phys. B* **44**, 045601 (2011).
- [211] K. Yaji, A. Harasawa, K. Kuroda, S. Toyohisa, M. Nakayama, Y. Ishida, A. Fukushima, S. Watanabe, C. Chen, F. Komori, et al., *Rev. Sci. Instrum.* **87**, 053111 (2016).
- [212] M. Buchmeier, R. Schreiber, D. Bürgler, and C. Schneider, *Phys. Rev. B* **79**, 064402 (2009).
- [213] L.-Y. Chen and J. A. Woollam, in *33rd Annual Technical Symposium* (International Society for Optics and Photonics, 1990), pp. 267–277.
- [214] J. Suits, *Rev. Sci. Instrum.* **42**, 19 (1971).
- [215] J.-W. Lee, J. Kim, S.-K. Kim, J.-R. Jeong, and S.-C. Shin, *Phys. Rev. B* **65**, 144437 (2002).

-
- [216] F. Krausz and M. Ivanov, *Rev. Mod. Phys.* **81**, 163 (2009).
- [217] X. Zhou, P. Ranitovic, C. Hogle, J. Eland, H. Kapteyn, and M. Murnane, *Nat. Phys.* **8**, 232 (2012).
- [218] T. Rohwer, S. Hellmann, M. Wiesenmayer, C. Sohrt, A. Stange, B. Slomski, A. Carr, Y. Liu, L. M. Avila, M. Källäne, et al., *Nature* **471**, 490 (2011).
- [219] J. C. Johannsen, S. Ulstrup, F. Cilento, A. Crepaldi, M. Zacchigna, C. Cacho, I. E. Turcu, E. Springate, F. Fromm, C. Roidel, et al., *Phys. Rev. Lett.* **111**, 027403 (2013).
- [220] I. Razdolski, A. Alekhin, U. Martens, D. Bürstel, D. Diesing, M. Münzenberg, U. Bovensiepen, and A. Melnikov, *J. Phys.: Condens. Matter* **29**, 174002 (2017).
- [221] H. Liu, Y. Li, Y. S. You, S. Ghimire, T. F. Heinz, and D. A. Reis, *Nat. Phys.* (2016).
- [222] N. Ishii, K. Kaneshima, K. Kitano, T. Kanai, S. Watanabe, and J. Itatani, *Nat. Commun.* **5** (2014).
- [223] T. T. Luu, M. Garg, S. Y. Kruchinin, A. Moulet, M. T. Hassan, and E. Goulielmakis, *Nature* **521**, 498 (2015).
- [224] F. Bencivenga, R. Cucini, F. Capotondi, A. Battistoni, R. Mincigrucci, E. Giangristostomi, A. Gessini, M. Manfredda, I. Nikolov, E. Pedersoli, et al., *Nature* **520**, 205 (2015).
- [225] T. Glover, D. Fritz, M. Cammarata, T. Allison, S. Coh, J. Feldkamp, H. Lemke, D. Zhu, Y. Feng, R. Coffee, et al., *Nature* **488**, 603 (2012).
- [226] S. Shwartz, M. Fuchs, J. Hastings, Y. Inubushi, T. Ishikawa, T. Katayama, D. Reis, T. Sato, K. Tono, M. Yabashi, et al., *Phys. Rev. Lett.* **112**, 163901 (2014).
- [227] G. New, *Introduction to nonlinear optics* (Cambridge University Press, 2011).
- [228] Y.-R. Shen, New York, Wiley-Interscience, 1984, 575 p. **1** (1984).
- [229] R. W. Boyd, in *Handbook of Laser Technology and Applications (Three-Volume Set)* (Taylor & Francis, 2003), pp. 161–183.
- [230] B. Adams, *Nonlinear optics, quantum optics, and ultrafast phenomena with X-rays: physics with X-ray free-electron lasers* (Springer Science & Business Media, 2012).

- [231] T. Arima, *J. Phys.: Condens. Matter* **20**, 434211 (2008).
- [232] Y. Ogawa, Y. Kaneko, J. He, X. Yu, T. Arima, and Y. Tokura, *Phys. Rev. Lett.* **92**, 047401 (2004).
- [233] M. Sakurai, S. Morita, J. Fujita, H. Yonezu, K. Fukui, K. Sakai, E. Nakamura, M. Watanabe, E. Ishiguro, and K. Yamashita, *Rev. Sci. Instrum.* **60**, 2089 (1989).
- [234] M. Yabashi and H. Tanaka, *Nat. Photon.* **11**, 12 (2017).
- [235] T. Ishikawa, H. Aoyagi, T. Asaka, Y. Asano, N. Azumi, T. Bizen, H. Ego, K. Fukami, T. Fukui, Y. Furukawa, et al., *Nat. Photon.* **6**, 540 (2012).
- [236] M. Rumi and J. W. Perry, *Adv. Opt. Photonics* **2**, 451 (2010).
- [237] K. Tamasaku, E. Shigemasa, Y. Inubushi, T. Katayama, K. Sawada, H. Yumoto, H. Ohashi, H. Mimura, M. Yabashi, K. Yamauchi, et al., *Nat. Photon.* **8**, 313 (2014).
- [238] A. I. Serykh and M. D. Amiridis, *Surf. Sci.* **604**, 1002 (2010).
- [239] R. Carli and C. Bianchi, *Appl. Surf. Sci.* **74**, 99 (1994).
- [240] B. Ivanov, *Low Temp. Phys.* **40**, 91 (2014).
- [241] P. Němec, M. Fiebig, T. Kampfrath, and A. V. Kimel, *Nat. Phys.* p. 1 (2018).
- [242] S. Dong, J.-M. Liu, S.-W. Cheong, and Z. Ren, *Adv. Phys.* **64**, 519 (2015).
- [243] M. Fiebig, T. Lottermoser, D. Meier, and M. Trassin, *Nature Reviews Materials* **1**, 16046 (2016).
- [244] Y. Tokura, S. Seki, and N. Nagaosa, *Rep. Prog. Phys.* **77**, 076501 (2014).
- [245] V. Laukhin, V. Skumryev, X. Martí, D. Hrabovský, F. Sánchez, M. García-Cuenca, C. Ferrater, M. Varela, U. Lüders, J.-F. Bobo, et al., *Phys. Rev. Lett.* **97**, 227201 (2006).
- [246] J. Heron, J. Bosse, Q. He, Y. Gao, M. Trassin, L. Ye, J. Clarkson, C. Wang, J. Liu, S. Salahuddin, et al., *Nature* **516**, 370 (2014).
- [247] C. Becher, M. Trassin, M. Lilienblum, C. T. Nelson, S. J. Suresha, D. Yi, P. Yu, R. Ramesh, M. Fiebig, and D. Meier, *Nat. Commun.* **5**, 4295 (2014).
- [248] A. Baker, A. Figueroa, L. Collins-McIntyre, G. Van Der Laan, and T. Hesjedal, *Sci. Rep.* **5** (2015).

-
- [249] F. Katmis, V. Lauter, F. S. Nogueira, B. A. Assaf, M. E. Jamer, P. Wei, B. Satpati, J. W. Freeland, I. Eremin, D. Heiman, et al., *Nature* **533**, 513 (2016).
- [250] M. Li, C.-Z. Chang, L. Wu, J. Tao, W. Zhao, M. H. Chan, J. S. Moodera, J. Li, and Y. Zhu, *Phys. Rev. Lett.* **114**, 146802 (2015).
- [251] M. Ye, W. Li, S. Zhu, Y. Takeda, Y. Saitoh, J. Wang, H. Pan, M. Nurmamat, K. Sumida, F. Ji, et al., *Nat. Commun.* **6** (2015).
- [252] G. A. Somorjai and Y. Li, *Introduction to surface chemistry and catalysis* (John Wiley & Sons, 2010).
- [253] K. Takeuchi, S. Yamamoto, Y. Hamamoto, Y. Shiozawa, K. Tashima, H. Fukidome, T. Koitaya, K. Mukai, S. Yoshimoto, M. Suemitsu, et al., *J Phys. Chem. C* **121**, 2807 (2017).
- [254] C. Hess, S. Funk, M. Bonn, D. Denzler, M. Wolf, and G. Ertl, *Appl. Phys. A* **71**, 477 (2000).
- [255] P. Srivastava, F. Wilhelm, A. Ney, M. Farle, H. Wende, N. Haack, G. Ceballos, and K. Baberschke, *Phys. Rev. B* **58**, 5701 (1998).
- [256] P. Srivastava, N. Haack, H. Wende, R. Chauvistré, and K. Baberschke, *Phys. Rev. B* **56**, R4398 (1997).
- [257] G. Waddill, J. Tobin, and D. Pappas, *Phys. Rev. B* **46**, 552 (1992).
- [258] E. Tamura, G. Waddill, J. Tobin, and P. Sterne, *Phys. Rev. Lett.* **73**, 1533 (1994).
- [259] J. G. Tobin, K. W. Goodman, F. O. Schumann, R. F. Willis, J. B. Kortright, J. D. Denlinger, E. Rotenberg, A. Warwick, and N. V. Smith, *Surf. Sci.* **395**, L227 (1998).
- [260] J. Tobin and F. Schumann, *Surf. Sci.* **478**, 211 (2001).
- [261] F. Hillebrecht, C. Roth, H. Rose, M. Finazzi, and L. Braicovich, *Phys. Rev. B* **51**, 9333 (1995).
- [262] M. Taguchi, J. Parlebas, T. Uozumi, A. Kotani, and C.-C. Kao, *Phys. Rev. B* **61**, 2553 (2000).
- [263] M. Taguchi, L. Braicovich, F. Borgatti, G. Ghiringhelli, A. Tagliaferri, N. Brookes, T. Uozumi, and A. Kotani, *Phys. Rev. B* **63**, 245114 (2001).
- [264] M. Taguchi and G. van der Laan, *Phys. Rev. B* **66**, 140401 (2002).